Mimicking Marine-based Natural systems: A Study of Sediment-hydrate Interactions Under *in situ* Conditions

A Dissertation Presented

by

Michael Waldram Eaton

to

The Graduate School

in Partial fulfillment of the

Requirements

for the Degree of

Doctor of Philosophy

in

Materials Science and Engineering

Stony Brook University

December 2007

Stony Brook University

The Graduate School

Michael Waldram Eaton

We, the dissertation committee for the above candidate for the

Doctor of Philosophy degree,

hereby recommend acceptance of this dissertation.

Devinder Mahajan, Dissertation Advisor
Professor, Department of Materials Science and Engineering

Miriam Rafailovich, Chairperson of Defense
Professor, Department of Materials Science and Engineering

Pelagia-Irene Gouma, Associate Professor,
Department of Materials Science and Engineering

Marco Castaldi, Assistant Professor,
Earth & Environmental Engineering, Columbia University

This dissertation is accepted by the Graduate School

Lawrence Martin
Dean of the Graduate School

Abstract of the Dissertation

Mimicking Marine-based Natural systems: A Study of Sediment-hydrate Interactions Under *in situ* Conditions

by

Michael Waldram Eaton

Doctor of Philosophy

in

Materials Science and Engineering

Stony Brook University

2007

Clathrate hydrates are inclusion compounds that owe their existence to the ability of water molecules to assemble via hydrogen bonding and form polyhedral host cavities around guest molecules. Such weak interactions impose thermodynamic and kinetic instability to these compounds, typically called gas hydrates. Found in marine sediments and permafrost regions, gas hydrates are of scientific interest to both climate change and energy recovery. However, it is the recent estimation of enormous hydrate deposits that has put the spotlight on recovery methods for energy production. As such, the focus of this thesis was to collect data that can aid in developing a thorough understanding of natural hydrate systems, and perhaps improve the economical extraction of such an abundant resource.

For this work, previously-hydrate-bearing sediments from known hydrate sites were selected as the porous media. The aqueous mediums used were pure water as well as simulated seawater in an effort to mimic "real life" hydrate conditions. A seafloor mimicking unit, namely the flexible integrated study of hydrates (FISH), was designed and constructed to control and record all aspects of the hydrate environment (temperature, pressure, and gas flow), all while enabling visual observation of dynamic behavior of hydrates on a macroscopic scale. Finally, simple computer models were constructed to simulate, in the case of hydrate formation, coupled mass transfer and chemical kinetics, and in the case of hydrate dissociation, coupled heat transfer and chemical kinetics. It was found that in porous, large-grained systems, large hydrate accumulations occurred, whereas in fine-grained systems, nodular and vein-like hydrate formations occurred. These data represent means for identifying the environments for more economically feasible hydrate production. Additionally, it was found that while hydrate formation closely followed a simultaneous diffusion/reaction curve in porous media, hydrate dissociation rates in all types of sediments and pressure/temperature environments occurred at more than 13 times that seen in pure water, even with heat transfer effects from the media controlled.

This work has implications for the improvement of current reservoir models for hydrate formations, and also provides the impetus for further study in realistic sediments, both from a microscopic and macroscopic point of view.

Table of Contents

List of Figures

List of Tables

Acknowledgements

This work could not have been completed (or perhaps started) without the encouragement and support of a huge number of people. Inevitably, I will leave people out, but it is my hope I've already told you how much you've meant to this work and to me along the way.

First, I wish to thank my advisor, Devinder Mahajan, whose breadth of knowledge in all things science is matched only by the tenacity with which he pursues them. Above all else, he has taught me the value in being a well-rounded researcher, and has given me insight into the business of science that no class could ever teach. He was also incredibly flexible with letting me have a life outside of the lab, and always understood if I had to come in a little bit late or leave a little bit early when the ferry schedules changed. For his understanding and patience, I am indebted.

I would also like to thank my committee, Marco Castaldi, Pelagia-Irene Gouma, and Miriam Rafailovich, who forced me to think both as a chemical engineer and a materials scientist, despite the fact that hand-waving would have been much more convenient, but ultimately less fulfilling. Special thanks goes to Marco, whose expertise and suggestions in modeling will ultimately go to furthering the designs and experiments presented in this work. General thanks also goes to the many people at Stony Brook University and Brookhaven National Laboratory whose assistance in all things non-hydrate-related kept me on track to actually graduate.

Of course, many thanks go to my colleagues for the last several years, Mozhgan Anjom and Prasad Kerkar, for always having a smile and a laugh available on demand. They are the most patient and dedicated researchers I have ever had the pleasure of working with, and they served as a standard by which I conducted my work.

Thanks to Justin Britsch, Andrew Caggiano, Matthew Douglass, Brent Lutz, and Shawn Slockers for keeping me distracted with humorous emails, but for also not letting me take my achievements (and, most importantly, my failures) too seriously.

Enormous thanks to my mom, Daryl, my dad, William, and my sister, Diana, for their emotional support. The finish line was so far away when I began, and their words of encouragement throughout MS/Ph.D. trek have been invaluable in keeping me going. Thanks also to "Family II," Charlie, Debbie, and Nick Williams, who have been as supportive as I could have possibly wanted. I love you all.

Finally, thanks to my wife, my muse, and my love, Erin Williams. Despite the long distance, late nights, and much-too-early mornings, her encouragement, dedication, and patience never waned. I cannot begin to express my gratitude for her partnership.

Chapter 1: Introduction

1.1 The Clathrate Hydrate

Clathrate hydrates were discovered in 1811 when, experimenting with chlorine-water mixtures, Humphrey Davy stumbled upon a peculiar phenomenon: the mixtures “froze” at temperatures above the freezing point of water. For the rest of the 1800’s, scientists studied the curious solids, determining that frameworks of water were stabilized by the inclusion of gases, and determining which molecules would co-exist with water to form such solids. Unfortunately, as the compounds did not appear to have analogs in nature, study stagnated from lack of widespread interest.

A rebirth in hydrate research came about in 1934, however, when E.G. Hammerschmidt discovered that hydrates were responsible for plugs formed in natural gas pipelines. At higher-than-ambient pressures, hydrates may form from water in the presence of hydrocarbons and other natural gas components (e.g. methane, ethane, propane, carbon dioxide, etc.) at temperatures above the freezing point of water. Such a large-scale problem thrust hydrates into the spotlight of industrial research in a quest to find additives to inhibit hydrate formation both kinetically and thermodynamically. Given the importance of natural gas as an energy source to our economy, the hydrate plugging problem remains an issue and more economical solutions are constantly being sought to minimize gas-flow disruptions during production. An exhaustive review of the subject is covered in a book by Sloan (1998).

Aside from artificial natural gas hydrate formation under appropriate temperature and pressure conditions in gas pipelines during production, recent estimates show that hydrates naturally exist as huge deposits ($1x10^{16}$ tons) at greater than 500 meters below the ocean floor and also trapped in the permafrost in very cold regions of the earth. The trapped gas is of either thermogenic or biogenic origin, depending on the location. Though the precise origin of hydrate deposits is still being debated, the sheer volume of available gas stored as hydrates worldwide is of interest to develop it as a clean energy source. Several options to economically transport the produced gas are being considered (Mahajan et al., 2000).

1.2 Hydrate Crystallographic Structure

Depending on the type of gas in contact with water, different hydrate structures will form. The three main structure types currently observed are: structure one (sI), structure two (sII), and structure H (sH). Until very recently, only sI and sII were thought to be found in nature – sH was mainly found in the laboratory domain. However, recent findings suggest that sH may also occur in oceanic hydrates (Sasson and MacDonald, 1994, Yousuf et al., 2003).

All three hydrate types are composed of at least two distinct polyhedral structures, or "cages." Typically, there is a small and a large cage, with sH being the exception (it has a third 'medium' cage). Additionally, all three hydrates have the same small cage – the so-called "building block" of each hydrate structure, a dodecahedron. The small cage has 12 pentagonal sides (defined as 5^{12}), and is shown in Figure 1.1. It should be noted for

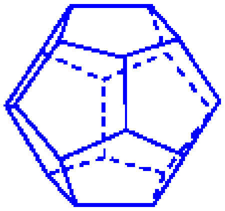

Figure 1.1 The 5^{12} "building block" of hydrate structures

the purpose of visualization that the vertices of each object represent the oxygen atom positions of the water molecules.

Structure I is also composed of a large cage, which is slightly bigger and less spherical than the 5^{12} cage. It is called a tetrakaidecahedron ($5^{12}6^{2}$) and is a 14-sided object with 12 pentagonal faces and two hexagonal faces. It is shown below in Figure 1.2

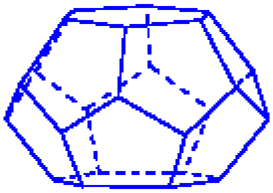

Figure 1.2 The $5^{12}\ 6^{2}$ large cage of hydrate structure sI

A sI hydrate unit cell (the repeating unit that forms a crystal) is formed when two small cages and six large cages link together at the pentagonal vertices.

The sII large cage is slightly bigger and more complex than sI's, having four hexagonal faces instead of two. It is called a hexakaidecahedron ($5^{12}6^{4}$), and appears as shown in Figure 1.3.

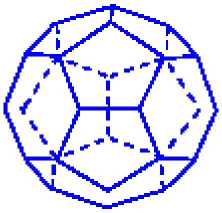

Figure 1.3 The $5^{12}\ 6^{4}$ large cage of hydrate structure sII

A sII unit cell is formed by the union of 16 small cages and eight large cages, and is held together by the sharing of common faces on adjacent 5^{12} cages.

Finally, the largest and most complex structure known, sH, has two cages other than a 5^{12}. They are called an irregular dodecahedron ($4^3 5^6 6^3$) and an icosahedron ($5^{12} 6^8$), respectively. Both cages are shown below in Figure 1.4.

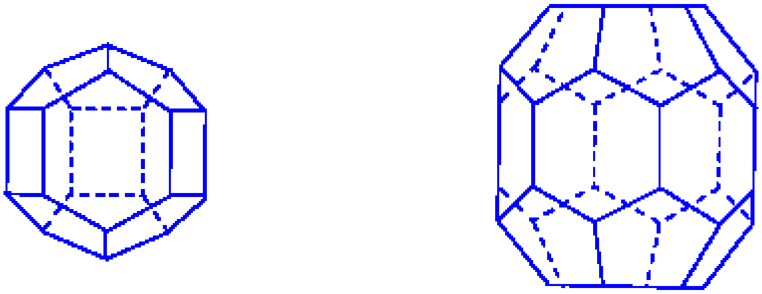

Figure 1.4 The $4^3 5^6 6^3$ and $5^{12} 6^8$ cages of structure sH

A unit cell of sH is composed of 3 small cages, 2 irregular dodecahedrons, and 1 icosahedron. Although it has been found in nature, sH is still very much a laboratory curiosity and further analysis and discussion of this structure will be withheld.

It was discovered by early researchers that irrespective of the structure, gas molecules stabilized the water framework in these inclusion compounds. Without a gas "guest" present, the water cages are unstable and would collapse. The gas, trapped inside the cages, acts to repel the cages slightly, keeping them open. The geometry of each cage dictates the size of molecule that can support their stability. A general rule is as follows: if the ratio of the molecular diameter of the guest to the diameter of the cage is a little less than one, the hydrate is stabilized. It is easier to think of this situation as an analogy with a ball inside a cage – if the ball is too large, the cage will crack, but if the ball is too small, the cage will collapse on itself. Table 1.1 lists structural characteristics of both sI and sII unit cells.

Table 1.1 Hydrate unit cell characteristics

Hydrate Structure	*Structure I*		*Structure II*	
Crystal System	Cubic		Cubic	
Space Group	Pm3n		Fd3m	
Avg. Lattice Parameter (Å)	12		17.2	
Cavity Type	Small (5^{12})	Large ($5^{12}6^{2}$)	Small (5^{12})	Large ($5^{12}6^{4}$)
Cavities/Unit Cell	2	6	16	8
Cavity Radius (Å)	3.95	4.33	3.91	4.73
Water Molecules / Unit Cell	46		136	

It should be noted that recent work by Huo (2003) has shown that the lattice parameter of each type of hydrate is affected not only by temperature (thermal expansivity), but also by composition, and therefore the lattice parameter given in Table 1.1 is simply an average.

In addition to basic structural knowledge, single-crystal X-ray diffraction (XRD) work by McMullan and Jeffrey (1965), and Mak and McMullan (1965) has revealed the atomic positions of each of the atoms within sI and sII unit cells, respectively. These results can be found in Tables 1.2 and 1.3. Recent neutron powder diffraction work by Rawn et al. (2002) and Chakoumakos et al. (2002) have revealed slightly different atomic positions, but differences could be caused by a number of reasons:

- the use of deuterated water when forming hydrates
- different experimental conditions
- greater sensitivity of neutron diffraction to light atoms, and
- different cage distortions due to different gas guests.

Table 1.2 sI atomic parameters (McMullan and Jeffrey, 1965)

Atom	Multiplicity	Site Occupancy	Fractional Atomic Coordinates			Temperature Factor (Å ^{2})
			X	*y*	*Z*	
1 O	16	1	0.18362	0.18362	0.18362	3.53
2 O	24	1	0.0	0.3071	0.11819	3.49
3 O	6	1	0.0	0.5	0.25	3.42
1 H	16	0.5	0.2350	0.235	0.235	6.0
2 H	24	0.5	0.0	0.4233	0.1967	6.0
3 H	24	0.5	0.0	0.3767	0.1667	6.0
4 H	24	0.5	0.0	0.335	0.035	6.0
5 H	48	0.5	0.075	0.2483	0.135	6.0
6 H	48	0.5	0.1033	0.2217	0.1633	6.0
Cage centers		Small cage:	0	0	0	
		Large cage:	0.25	0.5	0	

Table 1.3 sII atomic parameters (Mak and McMullan, 1965)

Atom	Multiplicity	Site Occupancy	Fractional Atomic Coordinates			Temperature Factor (A^2)
			X	y	Z	
1 O	8	1	0.0	0.0	0.0	3.46
2 O	32	1	-0.09228	-0.09228	-0.09228	3.52
3 O	96	1	-0.05744	0.05744	-0.024487	3.58
1 H	32	0.5	-0.06	-0.06	-0.06	8
2 H	32	0.5	-0.033	-0.033	-0.033	8
3 H	96	0.5	-0.08	-0.08	-0.146	8
4 H	96	0.5	-0.07	-0.07	-0.191	8
5 H	96	0.5	-0.024	-0.024	-0.0245	8
6 H	192	0.5	-0.024	0.091	0.278	8
Cage centers		Small cage:	0.5	0.5	0.5	
		Large cage:	0.125	0.125	0.125	

1.3 Basic Hydrate Thermodynamics and Prediction

In 1959, van der Waals and Platteeuw used statistical thermodynamics to create a gas hydrate equation of state; that is, a model which describes hydrate equilibrium at a given temperature and pressure (van der Waals and Platteeuw, 1959). The model is shown below in equation 1.1.

$$\frac{\Delta\mu_w^H}{RT} = \frac{\mu_w^\beta - \mu_w^H}{RT} = -\sum_i \nu_i \cdot \ln\left(1-\sum_k \theta_{ki}\right) \tag{1.1}$$

$\Delta\mu_w^H$ is the difference in chemical potentials of the theoretical empty hydrate cage, μ_w^β, and the occupied hydrate, μ_w^H. ν_i is the ratio of i-type cavities to water molecules in a unit cell, θ_{ki} is the fractional occupancy of species k, the guest gas molecule(s), in a type i cavity (either the small cage or large cage for sI and sII hydrates) per water molecule in the cage. To satisfy three-phase equilibrium conditions, pressures (P), temperatures (T), and chemical potentials ($\Delta\mu_w^H, \Delta\mu_w^L$) of each phase (hydrate, vapor, and liquid water) must be equal. The chemical potential for liquid water at a given state can also be written in terms of the difference between the chemical potential for water in the pure liquid phase and the chemical potential for water in the empty hydrate phase, $\Delta\mu_w^0$ at the reference state, as seen below

$$\frac{\Delta\mu_w^L}{RT} = \frac{\Delta\mu_w^0}{RT_0} - \int_{T_0}^{T} \frac{\Delta H_w^{\beta-L}}{RT^2} dT + \int_{P_0}^{P} \frac{\Delta V_w^{\beta-L}}{RT} dT - \ln(\gamma_w x_w) \tag{1.2}$$

Here, T_0 and P_0 represent reference temperatures and pressures, respectively, R is the universal gas constant, γ_w is the activity coefficient of aqueous water, x_w is the mole fraction of aqueous water, $\Delta H_w^{\beta-L}$ is the difference in enthalpy between the empty hydrate cage and liquid water, and $\Delta V_w^{\beta-L}$ is the difference in molar volume between the empty hydrate cage and liquid water.

The van der Waals and Platteeuw model assumes a Langmuir-type adsorption model of gas into the hydrate cage, as shown by

$$\theta_{ki} = \frac{C_{ki} P_k}{1 + \sum_k C_{ki} P_k} \tag{1.3}$$

Where C_{ki} is the Langmuir constant of the kth guest in the ith cavity. Equations 1.1 – 1.3, in addition to regressed models for the Langmuir constants, have been used extensively to model hydrate phase equilibria accurately (often within 2% of experiment), although some minor modifications have been employed to account for molar volume expansion due to guest occupation (Huo, 2003).

1.4 State Of The Art in Hydrate Research and Hydrates in Porous Media

As previously mentioned, hydrate research was sparked by the observation that hydrate plugs formed in natural gas pipelines during commercial production. The gas flow assurance aspect continues today. The thermodynamics and kinetics of hydrate plug formation dominate the field but recently research on hydrates as an energy resource is slowly coming into focus. Most thermodynamic prediction methods are sufficiently accurate to address industrial problems involving hydrates (Ballard, 2002). However, hydrate predictions for complex mixed guest systems (e.g. those in black oils, those confined within a sediment matrix) have not been as thoroughly investigated, and such systems are the current state of the art for thermodynamic predictions in clathrate systems.

Many real-world scenarios involving hydrate formation, like pipe flow, are inherently transient and require a kinetic analysis to be useful. Discreet element modeling of hydrate particles in a flow field, particle size analysis, and interparticle force measurements all feed into the current state of the art flow simulators, thus addressing another facet of cutting-edge hydrate research. Concomitant with kinetic measurements, the quest for newer and better anti-agglomerants (AA) and kinetic hydrate inhibitors (KHI) is a continuing task for the oil and gas industry. With the advent of increasingly accurate kinetic models, and the already established thermodynamic predictions, AA and low-dosage hydrate inhibitor (LDHI) research is at the forefront of current studies.

Energy recovery from hydrates, while not currently a major focus in industrial hydrate research, is gaining momentum in the hydrate community. As the worldwide energy crisis deepens, hydrates will be further relied upon for their vast stores of gaseous hydrocarbons. Estimates of total hydrated carbon (in the form of methane/natural gas hydrates) vary, but most common estimates appear to contain about $1\text{x}10^{16}$ tons of hydrated methane (Kvenvolden and Lorenson, 2001). Table 1.4, adapted from Milkov (2004) gives estimates by a number of different authors as to the large reserves of oceanic hydrated methane.

Table 1.4 Inventory of global estimates of methane in submarine gas hydrate ($\times 10^{15}$ m^3)

High - Low Estimate	Best or Average Value	Reference
3021-3085	3053	Trofimuk et al (1973)
	1135	Trofimuk et al (1975)
	1573	Cherskiy and Tsarev (1977)
	1550	Nesterov and Salmanov (1981)
110-130	120	Trofimuk et al (1979)
	3.1	McIver (1981)
5-25	15	Makogon (1981)
	15	Trofimuk et al (1983)
	40	Kvenvolden and Claypool (1988)
	20	Kvenvolden (1988)
	20	MacDonald (1990)
26.4-139.1	26.4	Gornitz and Fung (1994)
22.7-90.7	45.4	Harvey and Huang (1995)
	1	Ginsburg and Soloviev (1995)
	6.8	Holbrook et al (1996)
	15	Makogon (1997)
3-5	4	Milkov et al. (2003)
1-5	2.5	Milkov (2004)

Even conservative estimates of the amount of energy in hydrates on the ocean floor yield approximately twice the amount in all other fossil fuels combined (Kvenvolden, 1988, Kvenvolden and Lorenson, 2001). This is most easily seen in Figure 1.5, which shows the estimated global distribution of carbon in various sources.

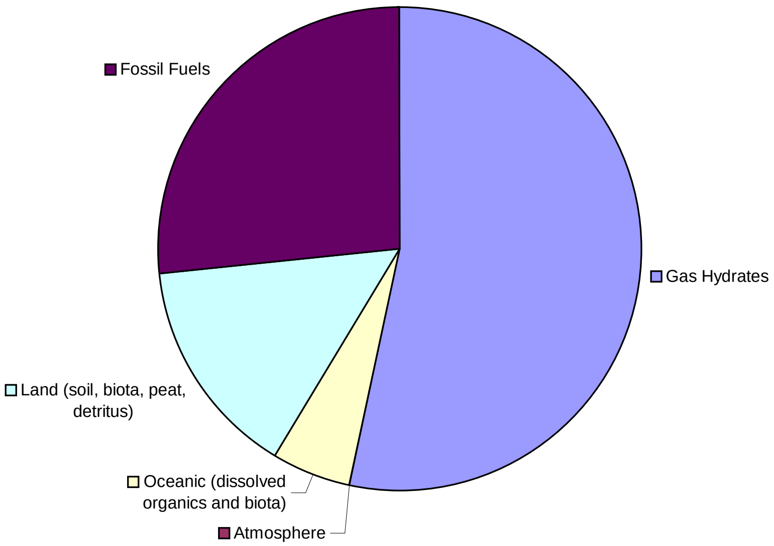

Figure 1.5 Worldwide distribution of carbon (USGS 2002)

Also of note about Table 1.4 is that it does not list hydrates found in permafrost regions, where hydrate thermodynamic equilibrium may also be achieved. Unfortunately, due to the overwhelming majority of hydrates found in oceanic regions, the error on such a calculation encompasses even the most liberal estimates of permafrost hydrate availability, and therefore oceanic energy recovery, while perhaps more difficult, will only be discussed. The Department of Energy (DOE) now estimates about 1% recovery of methane from the known methane hydrate reserves within the U.S. will be enough (over 2,000 trillion cubic feet) to satisfy the U.S. consumption for the next several decades (Boswell, 2007).

Reservoir simulations, spectroscopic analyses of natural hydrate formations, and active energy recovery from hydrates by countries like Japan will continue to contribute to the state of the art in this aspect of hydrate research (Dooley, 1999). Current reservoir models such as those by Hong et al. 2003, Moridis et al. 2002, and Gerami and Pooladi-Darvish, 2007 represent “cutting edge” work in such modeling fields, and pave the way for new work such as this in natural hydrate systems.

Given the current “push” towards utilization of hydrates as an energy resource, some of the major issues facing such work are locating economically feasible regions of hydrate accumulations and also extracting said energy in a way that has a net positive energy balance (i.e. the energy out is greater than the energy used to extract the hydrated gas). Many of the global deposits of hydrates are of low saturation; that is, the volume fraction of hydrates in the sediment is low (3-4%). The first goal, and partial focus of this work, is to determine the types/areas of sediment that give rise to large (i.e. “massive”) hydrate accumulations. Second, once the hydrates are found, the key becomes “how fast” or, simply, “how,” do we extract them in an economical way? While finding a suitable recovery method is not a focus of this dissertation, understanding the way in which hydrate formation in sediments alters hydrate dissociation behavior *is*, and thus may be used in the future to aid such recovery studies.

1.5 Incentives and Goals of This Work

The forgoing discussion emphasizes that much needs to be done to develop hydrates as a potential energy source of the future. While the proposed work herein is not intended to determine a new model for energy recovery from hydrates, it does seek to improve on such models through the use of data obtained from “real life” systems. Many of the current reservoir models use thermodynamic and kinetic data from laboratory hydrates – that is, those formed from distilled water and pure, research-grade gases. As mentioned, much work has been done to accurately predict such systems. However, very little data in the models takes into account the presence of sediment/impurities and all their confounding factors, such as: altered thermal and mass transport properties, possible autocatalytic effects of different minerals in the sediment, and the presence of biosurfactants which have been shown to greatly alter hydrate equilibrium (Rodgers et al. 2004). Performing experiments to determine hydrate kinetics and thermodynamics in sediments that were previously hydrate-bearing will perhaps allow refinement of the state-of-the-art models, and will greatly enhance our ability to exploit hydrates as an energy source. The potential of developing this indigenous resource has recently led resource characterization (Sloan. 1998), mining, and transport by economical conversion to liquid fuels aspects of hydrate R&D to attract increasing attention (Wegrzyn et al., 1999) with the ultimate goal of developing an environmentally benign method.

In addition to their potential as fuel, hydrates in nature are a concern because of their role in the structural stability of the seafloor around petroleum reservoirs. As a reservoir is tapped (that is, its gas and oil extracted), the pressure in and around the reservoir decreases. This lowers the stabilizing pressure on the hydrate and causes it to dissociate. Because hydrates are currently thought to 'cement' the sea floor around them (Feeser 1997), hydrate dissociation causes a loss of integrity, and huge shifts in sea floor stratigraphy can occur causing structures anchored to the sea floor to undergo unforeseen stresses. Figure 1.6 and 1.7 illustrate this phenomenon. Figure 1.6 is a cartoon showing the change in relief of the sea floor when a hot pipeline was run over a hydrate field (Hovland and Gudmestad 2001), while figure 1.7 shows a collapse feature present in a seismic image taken from a known hydrate site (Blake Ridge) off the coast of South Carolina, USA (Dillon et al. 2002).

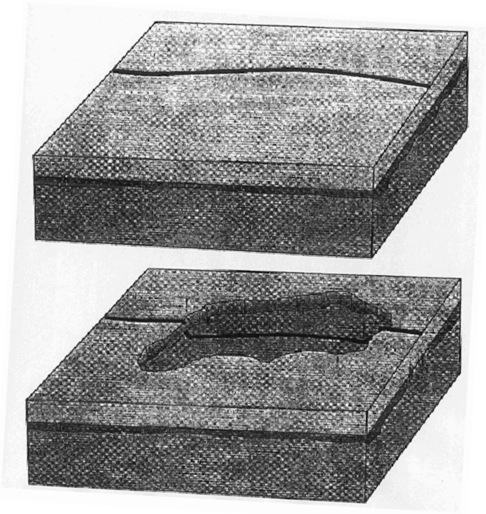

Figure 1.6 Theoretical damage from hydrate dissociation due to hot pipeline in a hydrate field

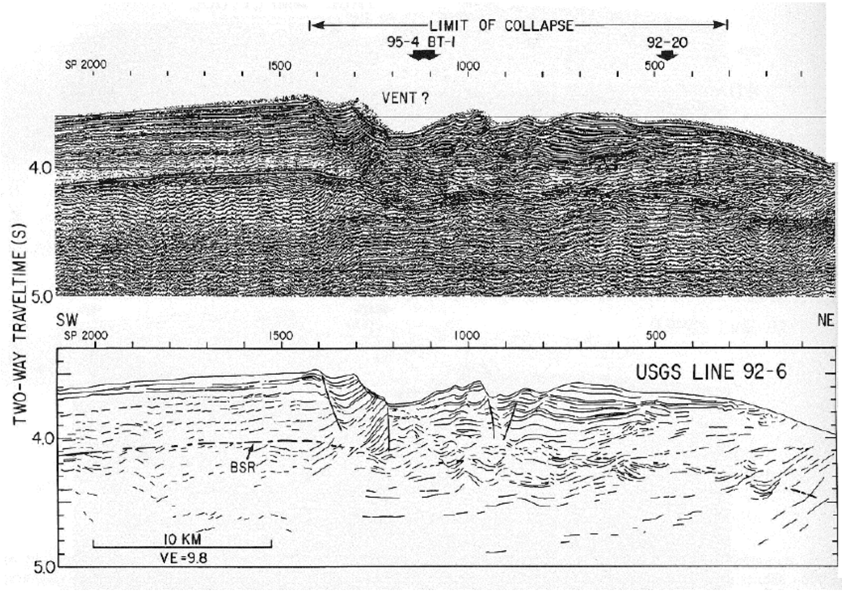

Figure 1.7 Seismic image of seafloor collapse from a hydrate venting occurrence (Dillon et al. 2002).

Finally, and perhaps most importantly, the need to understand *how* hydrates form in the sediment is required in order to determine the best or most economical locations around the world to begin extraction of hydrates for fuel, and also how to proceed in identifying such deposits. In many cases, it has been reported that hydrate saturations in sediments rarely go above 3-4 volume percent (Sloan, pp 483). Such low concentrations of available hydrate present not only economic problems due to the tremendous amount energy necessary to heat or depressurize a large volume of non-hydrate mass, but also safety concerns due to the large expanse of necessarily altered sea floor. However, it has been theorized and verified that there are "sweet spots" of hydrate formations – areas of hydrates in which large (perhaps hundreds of meters long and tens of meters deep) deposits occur, such as those of Leg 204 at Hydrate Ridge (Trehu et al., 2004). In fact, it has been observed that there are at least four types of hydrate deposits: disseminated, nodular, layered, and massive, with the goal of finding and utilizing the massive-type hydrate deposits simply due to their high concentration of energy. Figure 1.8 depicts each of the four types of hydrate-in-sediment configurations.

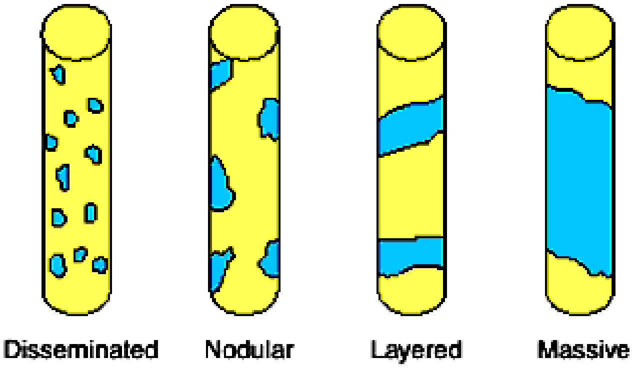

Figure 1.8 Potential Gas Hydrate Configurations (Sloan, 1998 and Collett, 2000)

It appears that for many hydrate formations, there is no single factor that definitively determines whether the sediment will contain dispersed hydrate or one of the other types of hydrate growth configurations. Mineral content, particle size and biological factors all appear to play a role, and the absence of a given factor does not necessarily imply the absence of dispersed hydrate. In general, however, the following qualities have been shown (in the Gulf of Mexico, Blake Ridge, Cascadia Margin, etc) to form significant quantities of disseminated hydrate:

1. "Large volumes of sandy and silty turbidites" (Ocean Drilling Program Leg 204). This obviously plays a role in the gas flux through the sediment (see also 2). Areas of high gas flux, such as those seen in the salt diapirs in the Gulf of Mexico or the mud volcanoes of the Caspian sea (Ginsburg and Soloviev, 1994), tend to occur via faulting of fine-grained sediments. Such high fluxes of gas, notably thermogenic, tend to produce massive hydrate accumulations.
2. Long, slow formation, associated with low gas fluxes. Such fluxes are of the 2-phase variety (methane saturated water, hydrate), where gas of biogenic origin is dissolved into water and consequently the lower-density water migrates up to the hydrate stability zone. Massive hydrate mounds are almost exclusively in areas of 3-phase hydrate formation (water, free gas, and hydrate).
3. From Lorenson, 2000:

   > "Observations of gas-hydrate-bearing sediment at microscopic resolution reveal a wide variety primary and secondary porosity, including the interiors of foraminifera tests, diatom tests, paleoburrows filled with sand-like microfossil debris, framboidal pyrite accumulations, and vesicular volcanic ash..." and "…it is suggested that disseminated gas hydrate is more likely to occur in sediment with higher primary and secondary porosity that contain more microfossils, paleoburrows, framboidal pyrite

accumulations, and vesicular volcanic ash rather than sediment lacking these large aperture pore spaces.“

Two terms above of some importance when describing guest gas origins in hydrates are biogenic and thermogenic. Biogenic gas is that gas which has been produced via bacterial metabolism. In general, a given sample of biogenic gas has between 1000 and 100000 times more methane (C_1) than ethane and propane (C_2 + C_3), and does not typically display the enrichment in the carbon-13 isotope than does its deeper-produced sibling, thermogenic gas (Bernard et al., 1976). Thermogenic gas is produced via deep thermal decomposition of matter, and contains, as a general rule, less than 100 times as much methane as ethane and propane for a given sample, and is also enriched in ^{13}C. Figure 1.9 below shows over 25 known sources of gas (from hydrates) and their origins, along with isotopic and C_1 to (C_2+C_3) ratios.

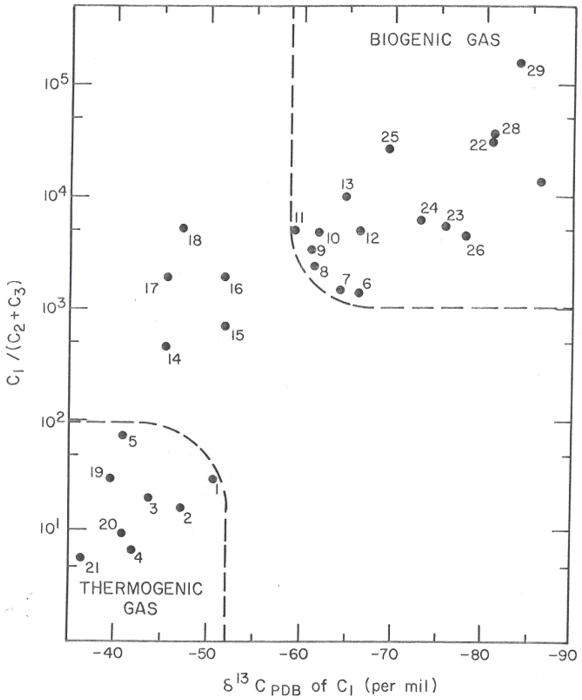

Figure 1.9 Heuristic for determination of the origin of gas from hydrates (Claypool and Kvenvolden, 1983)

Gas origin and hydrate configuration in sediment is important due to hydrate structural considerations. As has been shown (Subramanian, 2000), as little as 0.02 mol% ethane can cause a structural transition from an sI hydrate to an sII hydrate – resulting in lowered formation pressures by many hundreds of psi (and thus a more rapid formation for a given depth). In such a case where gas of thermogenic origin is in high flux, massive hydrate mounds may be observed (from point 1, above). However, the hydrate mounds are most likely of type sII due to their high ethane/propane content, and are of significantly less economic interest than those massive hydrates of type sI.

While analyzing the conditions necessary will allow us to *predict* where economically-retrievable hydrate formations will occur, it is also necessary to know how their presence in the sediments affects the actual *measurements* therein. Even without a dissociation event, it is known that hydrate intercalation between and throughout sediment layers affects sediment properties – namely, acoustic velocity and sediment strength. In order to identify the presence of hydrates, researchers exploit such changes using seismic techniques to identify large accumulations of hydrates. Although an in depth discussion of such acoustic techniques is beyond the scope of this thesis, it is important to note one important factor with such measurements: the bottom simulating reflector (BSR). The bottom simulating reflector is a region in the sediment/hydrate mixture where sound waves (sent from a vessel on the ocean's surface) travel first quickly as they pass through the dense hydrate layer, then very slowly as they propagate through the gas trapped below the hydrate accumulation, as can be seen in figure 1.10, with corresponding hydrate locations and saturations in figure 1.11.

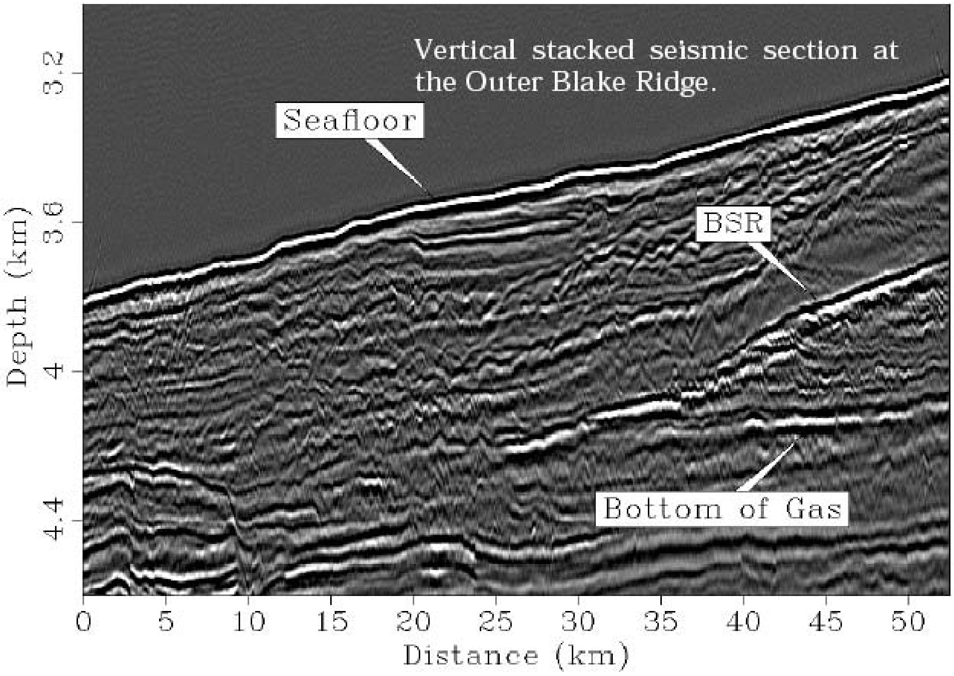

Figure 1.10 A seismic image of hydrate-bearing sediment showing the characteristically strong BSR line (Ecker et al., 2000)

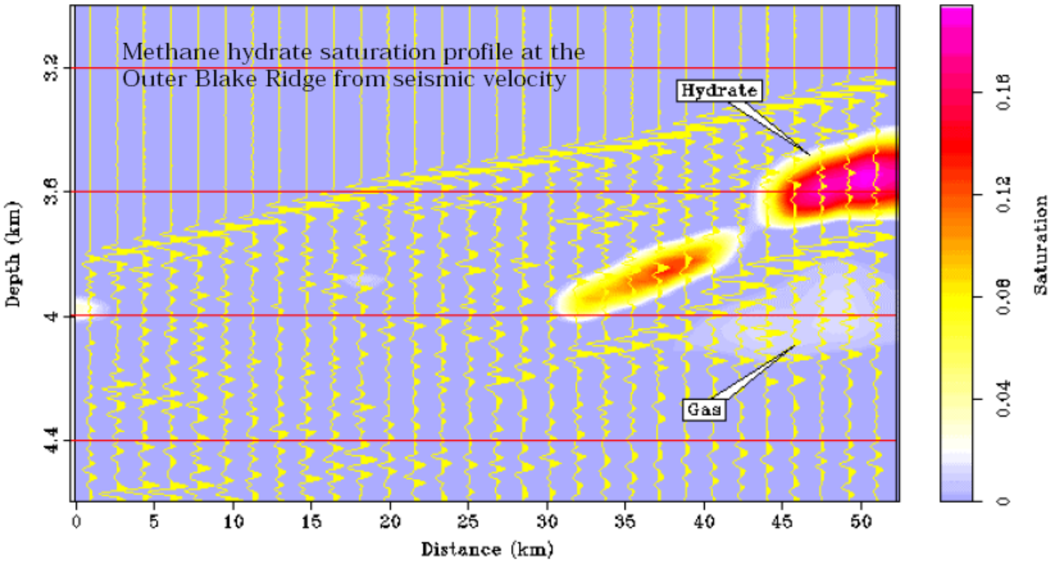

Figure 1.11 A seismic image of hydrate-bearing sediment with corresponding hydrate saturation overlay (Ecker et al., 2000)

Often, the BSR is said to indicate the base of the gas hydrate stability zone (GHSZ). This is the region in the sediment where the ambient conditions such as temperature (due to geothermal heating), pressure, and salinity transition from suitable to unsuitable for hydrate formation (Maekawa et al., 1995). Unfortunately, the BSR technique, though widely used, is not definitive for the presence or absence of hydrates. A more promising method, which may be borne out by further laboratory testing of sediments and hydrates, is "elastic property inversion…using high quality seismic data…followed by rock physics inversion" to determine gas hydrate saturations, with the idea that higher hydrate saturations lead to increases in elastic properties (Dai et al., 2004). However, the rock physics and elastic properties of the hydrate/sediment mix depend on *how* the hydrate forms, as seen below in figure 1.12.

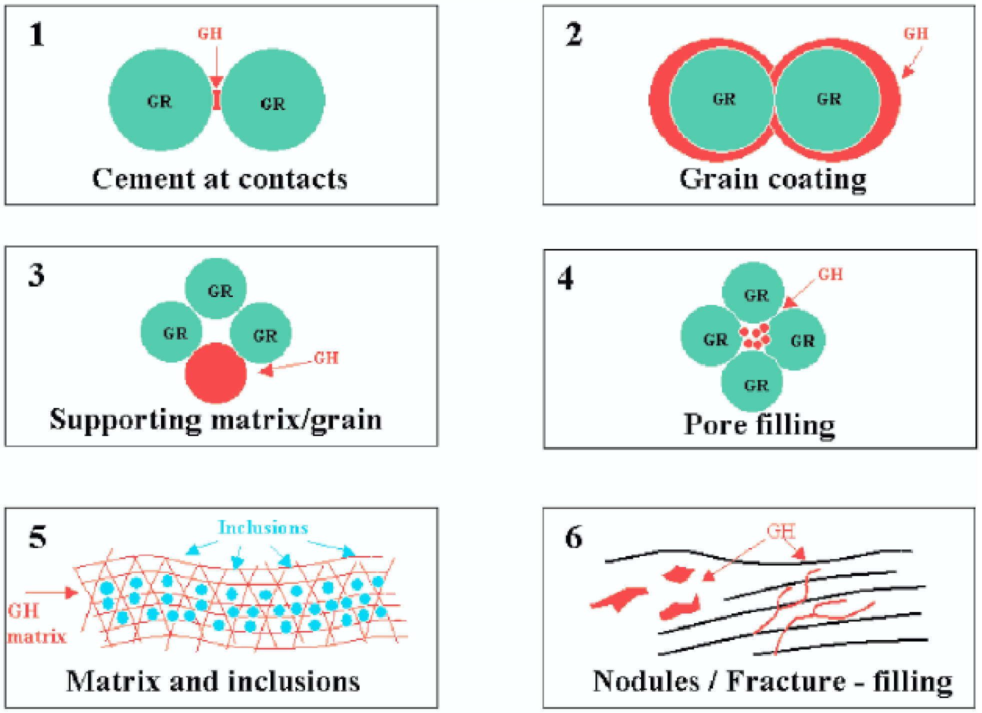

Figure 1.12 Existing microstructural models of gas hydrate bearing sediments (Dai et al., 2004).

Each of the models are described below:

1. This is a cementation model in which hydrates occur and the contact point between hydrate grains
2. Again, from the work of Dvorkin and Nur (1996), this model is a cementation model, however the hydrates grow around the sediment grains. Both models 1 and 2 yield erroneously large increases in elastic properties with small initial increases in hydrate saturation

3 & 4 Both of these models improve on the cementation models by considering hydrates as either load bearing or pore-filling structures (Dvorkin et al., 1999; Helgerud et al., 1999). The models are adjusted for sediment porosity, and are much closer to empirically determined elastic behavior at low hydrate saturations.

5. This model treats gas hydrate as the matrix and sediment grains as the inclusions (somewhat of the reverse of 1-4). It is important to note that models 1-5 consider hydrates as being homogeneously distributed in the sediment – most closely related to disseminated hydrate formation.
6. This model is proposed due to evidence found in hydrate cores suggesting that hydrates may also form large nodules and fill fractures (much like the massive/layered/nodule macroscopic formations listed above) in “shallow shaly sediments” (Dai et al., 2004).

Understanding the pressure and temperature conditions by which all of these types of hydrates occur, as well as the nature of their dissociation will allow for safer and more economical operations not only during resource extraction, but subsea operations in general.

Hydrates have been shown to occur in a variety of morphology and growth schemes, both on a microscopic and macroscopic scale, and in order to understand the means by which economic extraction of such a resource can proceed, the foregoing discussion presents an argument for a need to establish sediment-hydrate interaction under conditions that are relevant to naturally occurring hydrate systems. There is paucity of such data, though recent studies by Winters et al. (2004) and Kneafsey et al. (2007) are noteworthy. The purpose of this work, then, is to mimic seafloor conditions in the formation and dissociation of pure methane hydrates formed in once hydrate bearing, now depleted sediments. The thermodynamics of pure, laboratory hydrates are well established, and much work has been done to determine what effect, if any, the presence of porous media has on such values (Handa and Stupin 1992, Sheshadri et al. 2001). However, no work to date has been done using actual seafloor sediments (most have been tightly-size-regulated silica spheres or sand) despite the apparent need and importance of such data. In contrast to such thoroughly washed, low secondary porosity (internal pores) media, previously-hydrate-bearing sediment has not been stripped of any material (other than a slight loss of water), and therefore represents a true “reservoir” environment. Although complex, it contains all biosurfactants, secondary porosity, and other ions which may contribute to such sediment’s effect on hydrate thermodynamics and kinetics.

Chapter 2: Materials and Analytical Methods

A brief overview of the chemicals used in this work, including gases and sediments, is necessary. Additionally, analytical techniques for analyzing such chemicals should be mentioned, however detailed operation and theory behind the techniques is somewhat beyond the scope of this work. For a more thorough explanation of the computerized microtomographic technique, especially dealing with hydrates and porous media, the reader is first directed to work by Jones et al, 2006**.** For an introduction to the use and practice of gas chromatography, the reader is directed to the work by McNair and Miller, 1997. Finally, discussion of the main hydrate forming apparatus is carried out in the proceeding chapter, as it represents a significant step in the study and visualization of hydrates, and thus is presented alone, rather than with currently established techniques.

2.1 Sediment Samples and Analysis

Sediments from two different regions of the ocean floor around North America were used in this work. Three sediment samples, originally mined from Blake Ridge (Cruise: ODP leg 164; Latitude: 31° 48.210' N; Longitude: 75° 31.343' W; Hole/core: 995A-80X-1; Water Depth: 2278.5 m) were obtained through the Unites States Geological Survey (USGS), Woods Hole, Massachusetts. Previous measurements of stress history and geotechnical properties have been reported by Winters et al. (2004) (water content: 39.3 % dry weight; porosity: 51.0 %; maximum past stress: 2730 kPa). Three selected samples were taken from sub-seafloor depths of 1, 50, and 667m. Figure 2.1 shows the location of the Blake Ridge, along with bathymetric contours (Holbrook et al., 1996)

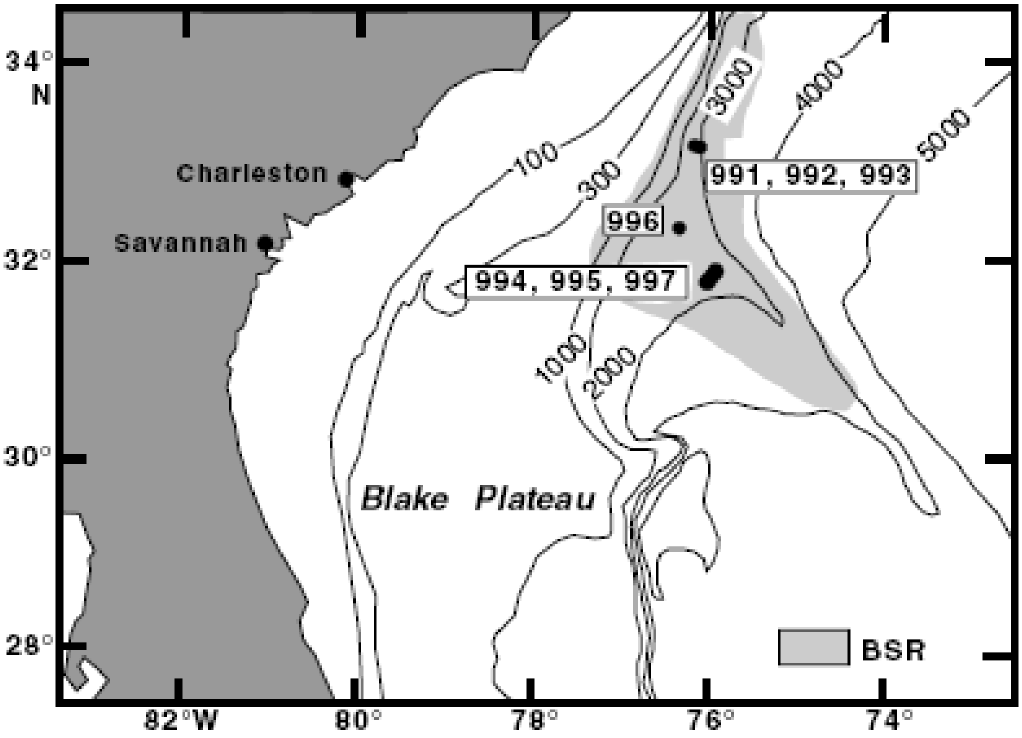

Figure 2.1 Geographic location of the Blake Ridge samples

The Blake Ridge site is important to hydrate research for several reasons. First, both hydrate and free gas have been discovered even in the absence of a clear BSR (see figure 2.2). As shown, site 994 lacks the acoustic character of a BSR (a strong 'line' on the seismic image), but reports from ship logs indicate "gas hydrate was sampled from two cores. Section 164-994C-31X-7 (258 mbsf) contained several white nodules of hydrate that ranged in volume from ~ 4 to 25 cm^3" (Taylor et al., 2000). Additionally, it should be noted that all three drill sites exhibited much the same water/chloride/sediment character laterally, although the three displayed three distinct seismic characters.

Secondly, and equally as important, is the depth at which the observed BSR occurs at the Blake Ridge site. Normally, as stated in chapter one, the BSR for hydrates typically ends at the base of the gas hydrate stability zone. That is, given a temperature in the sediment due to geothermal gradients, one expects to stop finding hydrates at a depth corresponding to the equilibrium pressure for the given temperature. Figure 2.2 more clearly demonstrates this phenomenon.

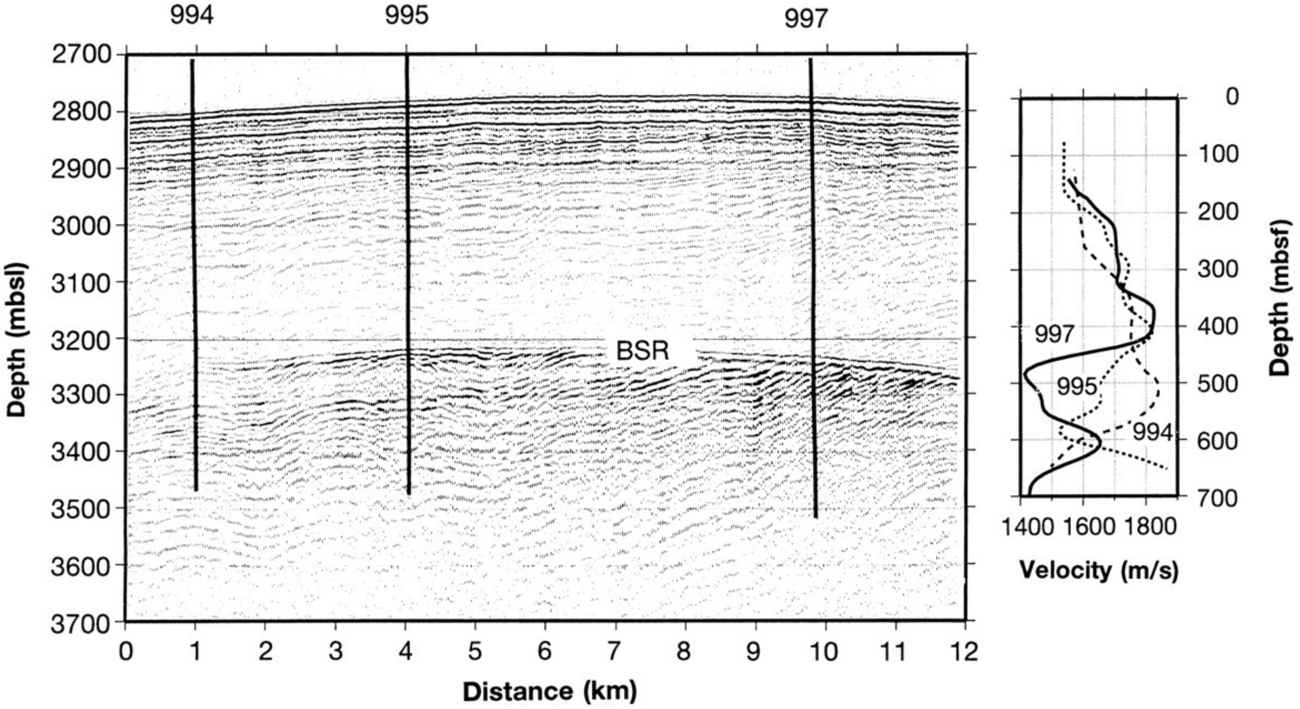

Figure 2.2 Acoustic measurements of ODP Leg 164 (Taylor et al., 2000)

Figure 2.3 shows the temperature required, for a given seawater depth (or, seawater and sediment, if below the mudline), to ensure hydrate stability. Two curves are shown: one for pure water and one for seawater, which is taken to be 3.35% NaCl, among other elements at smaller concentrations. Both curves were generated via Gibbs energy minimization of the hydrate equation of state using CSMGem, the de facto standard for hydrate prediction

(Ballard, 2002). It is readily seen that the salt acts as a hydrate inhibitor, much as salt acts to decrease the melting point of normal ice. In the curves above, all points to the left of the curve (that is, temperatures lower for a given depth) are thermodynamically capable of forming hydrates. All points to the right of each curve, then, are thermodynamically unsuitable for hydrate formation. It should be noted that because hydrates are less dense than water (and also seawater), even though temperature and pressure conditions are right for hydrate formation, hydrates will not be found in the open ocean due to their buoyancy and eventual dissociation at lower depths. Therefore, hydrates will only be found *below* the mudline, where they are immobilized, and to the left of the formation curves, as indicated. As mentioned previously, the BSRs' for hydrate formations are located

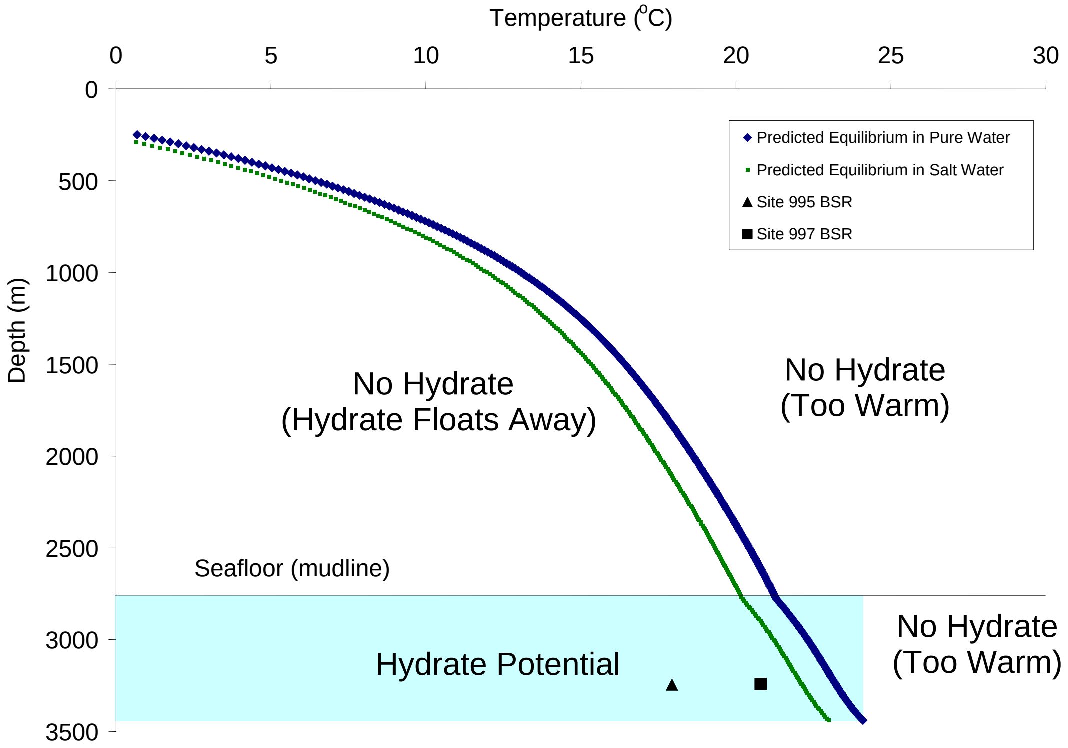

Figure 2.3 Hydrate equilibrium curves as a function of depth and observed Blake Ridge BSR sites

at the point where the acoustic velocity in a hydrate/sediment formation rapidly decreases as the seismic waves travel from an area of high density (hydrate) through a free gas layer (low density). Traditionally, this free gas is thought to exist because the sediment below the hydrate mass is simply too hot to support hydrate formation, and thus the hydrates dissociate, trapping the gas. This, as mentioned, corresponds to the base of the gas hydrate stability zone (GHSZ).

It can be seen in figure 2.3 that the BSR's for both site 995 and 997 of the Blake Ridge occur well within the hydrate stability zone. This is unusual, as it appears as though the hydrate equilibrium conditions for this particular area/sediment have shifted by between 1.3° and 4.2°C lower than predicted in salt water, suggesting an inhibition. Ruppel (1997) offers several hypotheses for the inhibition:

- The gas below the BSR may simply be anomalous, and that the P-T conditions the BSR is currently at are not sufficient to dissociate hydrate
- Although disputed, hydrates may not have completely adjusted to sea level and climate changes during the Pleistocene-Holocene era, and are thus at a non-equlibrium P-T condition
- Most likely, inhibition due to small pore sizes (resulting in increased pore pressure, as noted earlier) is causing the equilibrium shift

The second sets of sediments used were from the northern portion of the Gulf of Mexico in an area known as the Keathley Canyon (figure 2.4). Samples were obtained through the Department of Energy's Join Industry Project (JIP) with ChevronTexaco. The location of site 151, hole #3, where all sediment samples were acquired from is latitude 26° 49' 22.6" N, longitude 92° 59' 11.3" W. Water depth was approximately 1311 m at the drill location. Two selected 1 m samples in 10cm intervals were taken from sub-seafloor depths of 1m and 260 m. Water contents of these samples were interpolated using available measured data and were approximately 94.5 and 30%, respectively. Additionally, the samples had porosities of 73.2 and 48.5% sediments (JIP Cruise Report, 2005).

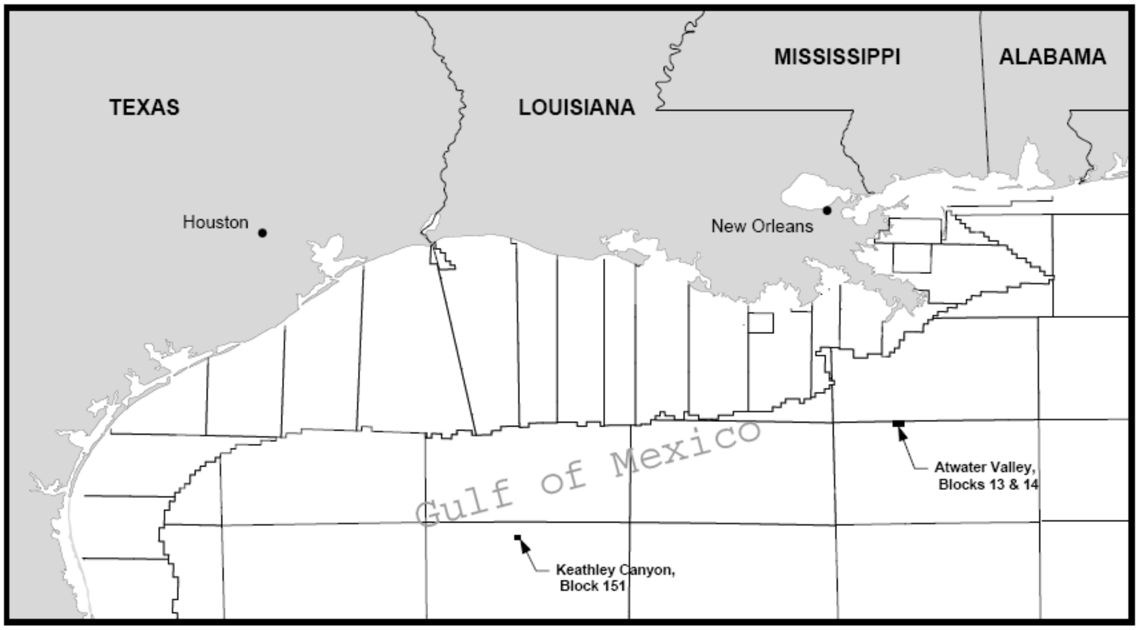

Figure 2.4 Geographic location of Keathley Canyon Well KC151

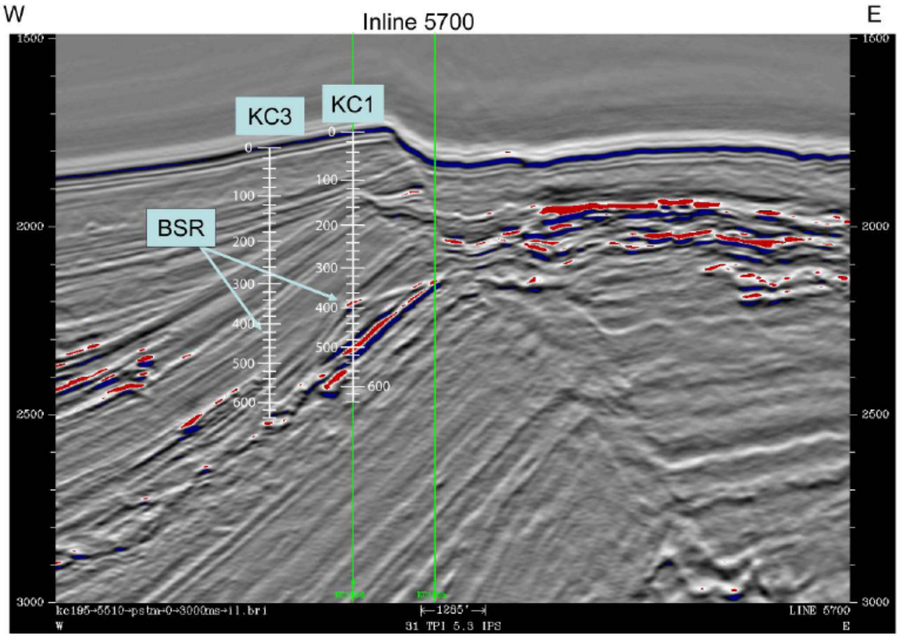

Figure 2.5 Seismic Image of Keathley Canyon Well KC151 Sites 1 and 3

Figure 2.5 shows an image of the seismic record for both sites KC151-3 (the location of the samples used) and KC151-1, a hole drilled in close proximity to #3 and upslope on the apparent BSR

The Gulf of Mexico (GOM) site is interesting to study because it contains sediments on the opposite end of the particle-size spectrum from the Blake Ridge. Whereas the Blake Ridge site has massive or nodular type hydrates contained within coarse-grained sediments, Keathley Canyon, with its mainly fine-grained particles, was found to have very little in the way of massive-type hydrates. In fact, most results from KC151 #3 suggest a content of mostly disseminated hydrates, with larger, vein-like hydrates only found at fracture sites (not within the sediment matrix). It should also be pointed out that off-gasses from each of the GOM cores contained, at minimum, 99.6% methane, with the remainder being largely CO_2 with relatively low (< 90 ppm) concentrations of higher hydrocarbons. Likewise, shipboard Blake Ridge hydrate dissociation revealed the presence of ~99% methane gas (indicative of sI). This purity, indicative of microbial/biogenic methane, supports the use of pure methane gas in our experiments.

In terms of classifying each site's sediment, it is helpful to understand the classification scheme. Table 2.1 below demonstrates the Udden-Wentworth grain-size classification scheme for siliciclastic sediment (Wentworth, 1922).

Table 2.1 Udden-Wentworth grain classification scale

Millimeters (mm)	Micrometers (mm)	Phi (f)	Wentworth Size Class	
256		-8	Boulder	Gravel
64		-6	Cobble	
4		-2	Pebble	
2		-1	Granule	
1		0	Very coarse sand	Sand
0.5	500.00	1	Coarse sand	
0.25	250.00	2	Medium sand	
0.125	125.00	3	Fine sand	
0.0625	62.50	4	Very fine sand	
0.03125	31.25	5	Coarse silt	Silt
0.015625	15.63	6	Medium silt	
0.0078125	7.81	7	Fine silt	
0.00390625	3.91	8	Very fine silt	
0.00006	0.06	14	Clay	Mud

Figure 2.6 shows the particle size distribution, as determined by a commercial analysis laboratory, Microtrac, Inc., of both the shallowest and the deepest sediments in the Blake Ridge and Gulf of Mexico sites. There are several items of note in the figure. First is that the deepest sediments from both sites have their highest fraction of sediments from 3-5 microns in diameter. However, while the GOM sample is unimodally distributed, the Blake Ridge sediment is bimodal, and has a relatively large fraction (>10%) of sediment which is considered sand. This is interesting, because as pointed out by Turner (2002): "volume contributions of large pores are typically much larger than small pores. Therefore, if large pores are present, the large pores are likely to dominate, and an equilibrium shift may not be

observed even in the presence of small pores." The average pore size of the Blake Ridge sediments approaches 1000Å (Clennell et al., 2000), and thus, according to Turner (and in contrast to Ruppel, 1997), an equilibrium shift should not be observed in hydrates formed at the Blake Ridge, simply because such large pore spaces would not alter hydrate thermodynamic equilibrium by a measurable amount (i.e. the error on the temperature measurement would envelope the shift in equilibrium in such large pores). The second interesting point is that most hydrates found in the sediment of the Gulf of Mexico are disseminated.

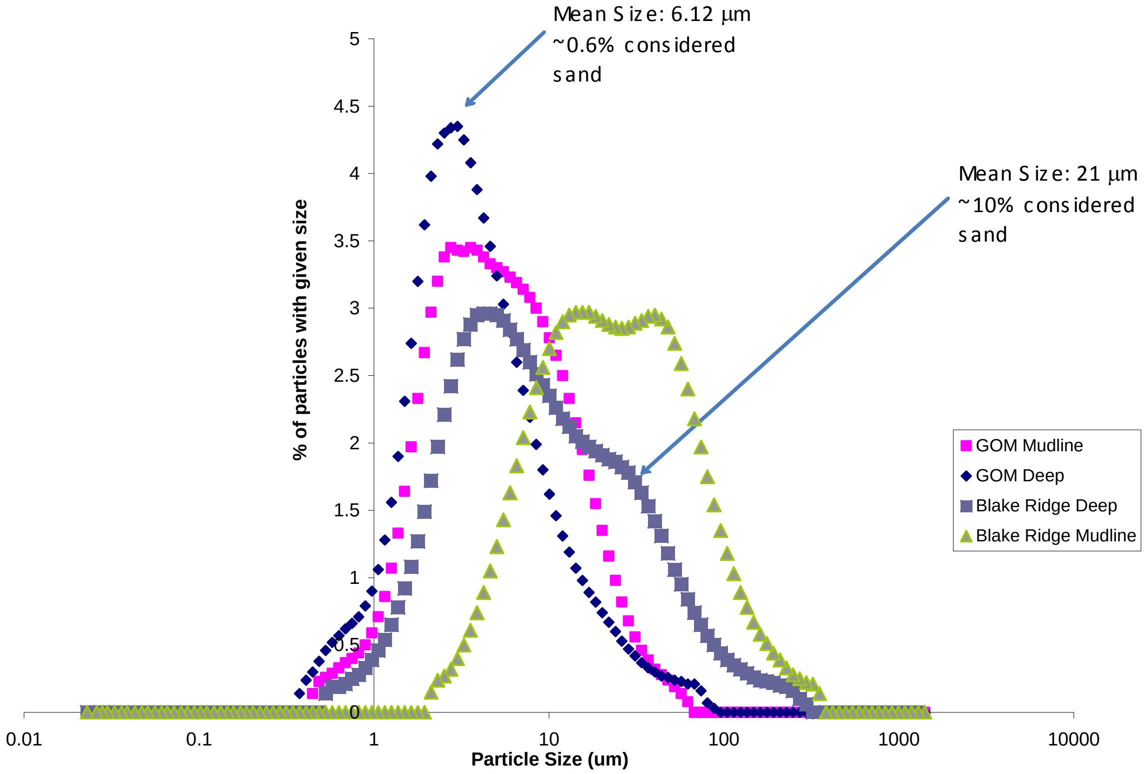
Mean Size: 6.12 µm
~0.6% considered
sand

Mean Size: 21 µm
~10% considered
sand

Figure 2.6 Particle size distribution of Blake Ridge and Gulf of Mexico sediment samples from various depths

Only at faults and fissures in the sediment has it been suggested that massive/nodular/vein hydrates form. In the Blake Ridge, however, massive hydrates were found in areas not limited to active vents, and thus the unanswered question is whether particle size of these two end-membered sediments has an influence on hydrate morphology/growth/cementation in the sediment matrix.

Both sets of sediments were analyzed using computerized microtomography (CMT) at the National Synchrotron Lightsource (NSLS) at Brookhaven National Laboratory (BNL), beamline X-27a (shown in figure 2.7 below). Synchrotron radiation is useful for studying such samples because it has exceptional brightness, tunability, and polarization, allowing penetration and focusing into very small and dense samples. Using such a device, the 3-D morphology, pore-space pathways, porosity, and permeability values of the sediment were extracted. This provides not only a "visual" inspection of the microscopic nature of the sediment which complements the macroscopic view in the hydrate formation unit, but also verification of pore-size, grain-size, and surface area data obtained from bulk measurements.

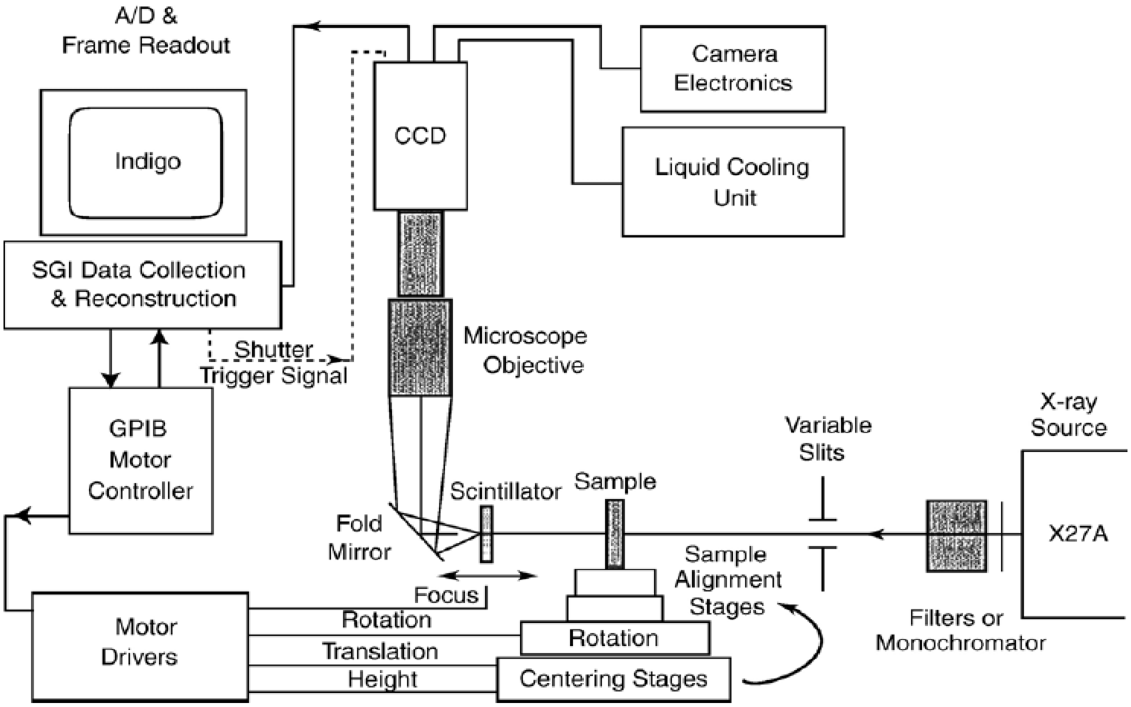

Figure 2.7 Major component schematic of the X-27a beamline at the NSLS (Jones et al., 2006)

For all imaging, a small amount of wet, intact sediment (~0.5 g) was placed in a polyethylene tube with an inside diameter of 4.71 mm and a wall thickness of 0.81 mm. Care was taken when loading the tube so as not to agitate the natural packing of the sediment. A brief overview of the imaging and 3-D reconstruction technique, summarized from Jones et al., 2006, is as follows:

1. An area beam is used to illuminate the sample and surrounding air.
2. The X-rays are detected with an yttrium aluminum garnet (YAG) scintillator that is viewed by a CCD camera.
3. The sediment tube is rotated through 180° in 0.09° increments, with image acquisition at each stop

4. The three-dimensional image is then reconstructed from the ~2000 two-dimensional images using a Fast-Fourier Transformation (FFT) method (Dowd et al., 1999).

Figure 2.8 shows a 3-d reconstruction of a deep (667mbsf) sample of Blake Ridge sediment. Color intensity is indicative of X-ray attenuation (arbitrary units), and a lack of color represents the pore-space. It is important to note the heterogeneity of the sample, both in terms of particle size and pore-space distributions, which can also be inferred from figure 2.6.

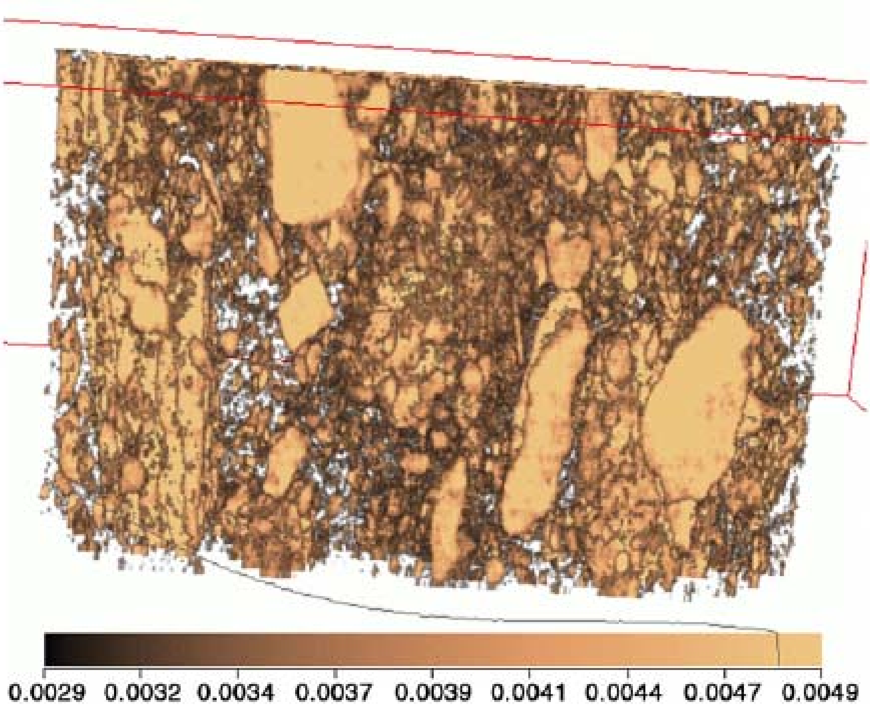

Figure 2.8 CMT Reconstruction of Blake Ridge sediment (units are of arbitrary X-ray absorption)

2.2 Gases and Analysis

Gas used in all experiments was obtained from Matheson. ‘Matheson’ grade methane and was used, with a certified purity of 99.99%. Higher hydrocarbon content ($C_{2-3}H_{4-8}$) in the methane was less than 3 parts per million (ppm), with nitrogen impurities present at 60 ppm or less. Predictions using CSMGem indicate probable sI hydrate formation for all pressures less than approximately 6000psi for such a mixture (Ballard, 2002). Gases were analyzed prior to injection for all runs in a GOW-MAC Series 580 Gas Chromatograph. Additionally, during any given run, a sample of gas was collected from the headspace in the hydrate formation unit using a gas-tight syringe to determine if any residual gas from the sediment samples was present. This was necessary because analyses of recovered hydrate cores from which the sediments samples were extracted showed 90 ppm levels of heavy hydrocarbons (as well as CO_2). While it is not expected that these gases would linger (due to their storage at atmospheric conditions) in the host sediments, analysis was nevertheless performed to ensure no residual gas interfered with our results. Figure 2.9 shows the chromatograph analysis of both a gas sample from the commercial gas cylinder (as-delivered) as well as a sample from the headspace of the hydrate formation unit after loading the sediments/water slurry under N_2. It should be noted that the depicted data in figure 2.9 are from the very first sediment charge when any natural contaminants would be at their highest level (subsequent runs would be diluted by constant charging with methane).

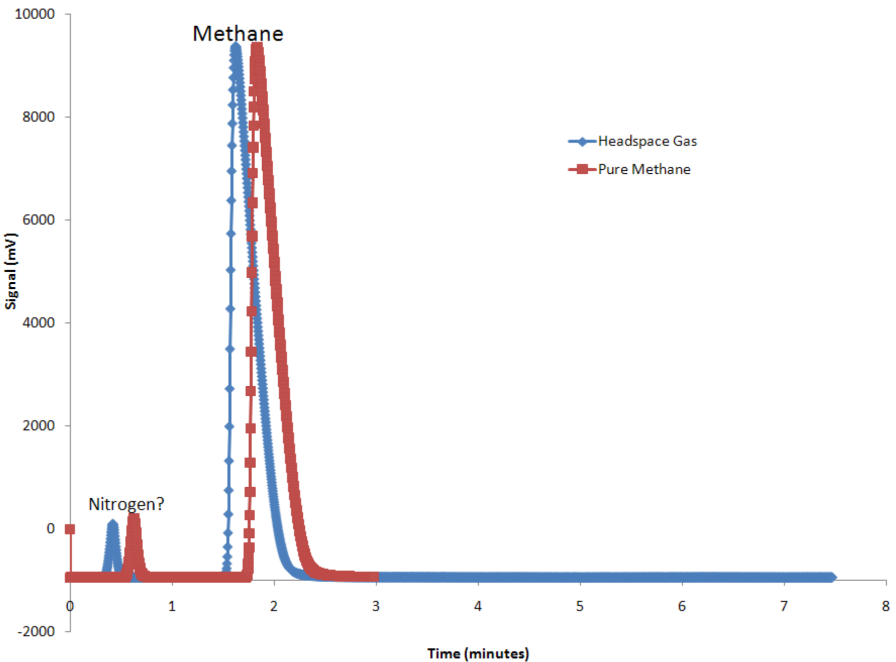

Figure 2.9 Gas chromatograph results of delivered vs. headspace gas of 1st run on Gulf of Mexico sediment

As can be seen in Figure 2.9, areas under the peaks attributed to methane differ by only 0.27%, which suggests a good agreement within experimental error. The time shift between runs was due to a delay between injection and acquisition, and is considered to be trivial to the analysis. While not shown, Blake Ridge sediments displayed similar behavior– no residual gas was observed. The first peak is attributed to nitrogen, the largest contaminant in the Matheson grade gas which is non-polar and faster-traveling, and thus should appear first in the chromatograph output.

2.3 Kinetic Runs

Hydrate formation and decomposition kinetic data collection was one of the main objectives of this dissertation. Though the kinetic aspect is discussed in detail in a later chapter, it should be noted that a typical kinetic run involves: 1) FISH unit shakedown, 2) sediment loading, 3) bringing the entire system under equilibrium conditions, 4) data collection, 5) material balance, 6) data analysis. Hence, each run presented takes approximately a month to complete. For this project, a series of runs were completed, several done in duplicate and triplicate, and the data analyzed.

The ensuing chapters are dedicated to data collection and analysis that resulted from this work. Hence, the chapters are arranged to address specific focus areas. These are:

1. The FISH Unit construction and its instrumentation.
2. Formation kinetics and growth morphology
3. Decomposition kinetics and thermal modeling of the system
4. Future work and enhancements

Chapter 3: The FISH Unit

Although the materials and analytical methods used for studying gas hydrates have been mentioned previously in chapter two, the heart of the hydrate studies, the Flexible Integrated Study of Hydrates (FISH) Unit, has been given its own chapter. This is because it not only represents a significant amount of work (two and a half years of iterative refinements have gone into its construction), but also because it represents somewhat of a departure from the typical vessels used to study gas hydrates. As such, it is informative to gain perspective as to what is currently available, why they are used, and why the FISH unit represents an improvement to the current technology.

3.1 Existing Technology

Often, hydrates in the laboratory are formed in a sealed vessel by contacting the hydrate former (either in the gas or liquid phase) and liquid water, and then increasing the pressure until crystalline hydrates form, as often indicated by a drop in pressure. This vessel is usually an autoclave cell – a thick stainless steel vessel typically on the order of 100ml with little in the way of observation methods either visually or spectroscopically. Alternatively, a technique developed by Stern et al (2000) is used in which hydrates are formed from powdered water ice and a pressurized hydrate guest, and the temperature is allowed to increase in the autoclave cell until hydrate conversion begins, again, as noted by a pressure drop. In the latter case, hydrate formation occurs extremely rapidly as the water changes phase from solid to liquid. A large surface area, combined with the rate of diffusion into the water is the key; gas into liquid diffusion is orders of magnitude faster than gas into solid diffusion, and thus at the melting point, hydration is rapid. While both methods have advantages, they are not without their disadvantages. The second method, beginning from ice, allows for rapid water-to-hydrate conversion, but begins with a substrate (ice) not known to exist in oceanic hydrate conditions. Additionally, this technique is somewhat incompatible with hydrate formation in sediment – grinding ice and sediment together in order to achieve a homogeneous mixture as well as a large ice surface area may cause alteration of the physical properties of the sediment (particle size, pore geometry), and may also cause unnatural fusing of the sediment grains as the ice melts and refreezes during agitation. The first method (gas and liquid water), while accurately mimicking gas-rich hydrate formation conditions (Suess et al., 2001), offers no reproduction of the gas-lean case where hydrate formation occurs from a single-phase solution of a dissolved hydrate guest. That is, dissolved methane, or any other water-soluble hydrate former, has been shown by Huo (2003) and others to form hydrates (perhaps like those in some sediment conditions) given sufficient time, despite the lack of a free gas phase; a huge excess of gas in an unagitated, non-pre saturated autoclave cell is only capable of forming two-phase hydrates. However, this method is more appropriate to modeling *in situ* conditions than is the ice-method of Stern et al. (2000).

Although there are many iterations of the aforementioned setup, there are two hydrate formation units that are what might be considered “second generation.” The first is at Oak Ridge National Laboratory (ORNL) and is the Seafloor Process Simulator (SPS). Shown in front and side views below in figure 3.1, it is a 72 liter temperature-controlled high-pressure vessel with a working range from 0-2900 psi and 0°C to 10°C.

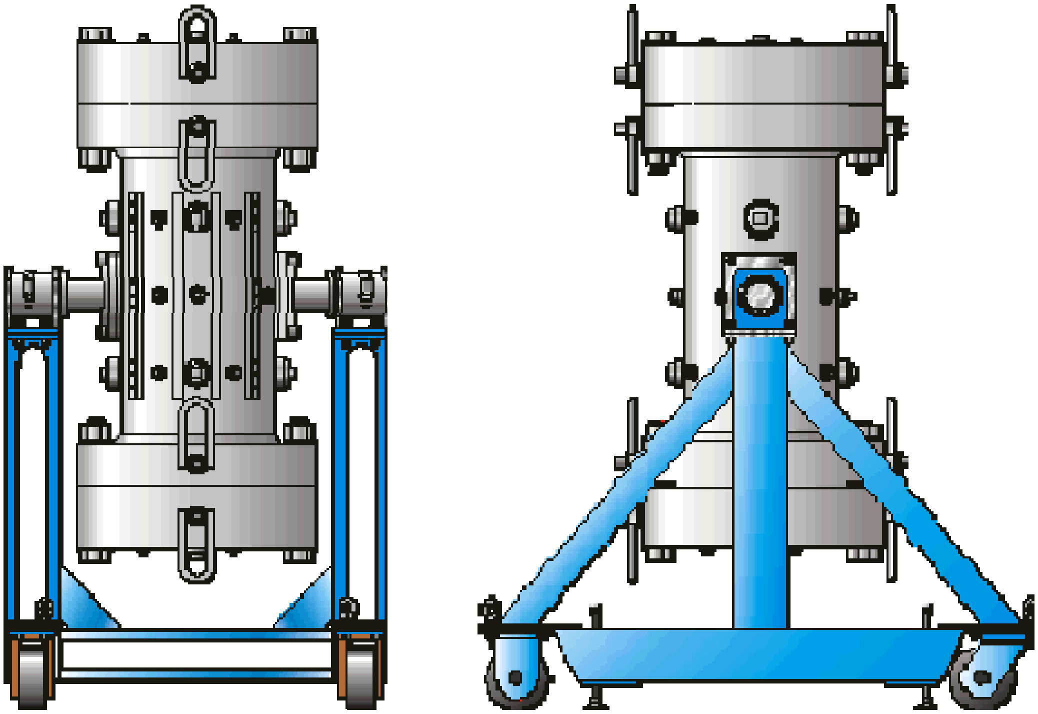

Figure 3.1 Front and side views of ORNL's Seafloor Process Simulator (obtained from http://sps.esd.ornl.gov/facilitiestools.html)

The SPS is an ideal reactor in which to run scale-up experiments. Such a large volume of contained sediment and water can, perhaps, most closely mimic the more macroscopic hydrate and sediment features (veins, fractures), all while maintaining a very stable temperature due to its large thermal mass. In addition to its size, its two main advantages over the first-generation autoclave-type cell are its flow-through capability (it is not simply a batch reactor, allowing for simulation of single-phase hydrates), and its monitoring capabilities. While most autoclave cells have pressure monitoring, and many have multiple temperature monitoring throughout their geometries, none have ports for visual inspection – they are essentially closed to any type of inspection. As mentioned previously, understanding how hydrates form in both the cementation/intercalation and disseminated/nodular/massive type schemes is just as important as understanding the temperature and pressure conditions in which they form. Autoclave cells, while offering accurate answers to the latter question, cannot address the morphological characteristics of hydrate/sediment interaction.

Unfortunately, the SPS also has its disadvantages. First and foremost is its bulk and usability. At 72L, the mostly-metal vessel weighs around 3000 pounds (1361 kg). The lid alone weighs 700 pounds (317 kg) and requires 16, 1.5 inch diameter (3.81 cm) bolts tightened to 2000 foot-pounds (2711 N-m) of tension to maintain pressure. The machine requires a crane to operate, and has an open/close time of approximately 2 hours; this is in addition to time required to cool the unit. Also, despite its large size, the SPS has only two, 2 inch (5cm) diameter sapphire windows with which to view hydrate formation. So, despite its ability to simulate large, scaled-up systems, its visualization capabilities of macroscopic phenomena are equal to a much smaller device, perhaps causing researchers to miss important behavior above or below each viewport.

The second generation two device currently in use is the Gas Hydrate and Sediment Test Laboratory Instrument (GHASTLI), a unit at the United States Geological Survey (USGS), Woods Hole, MA. GHASTLI is capable of pressure, temperature, flow, shear, and acoustic measurements.

Figure 3.2 A picture of the GHASTLI setup

(http://geology.usgs.gov/connections/mms/joint_projects/methane.htm)

Despite its significant capabilities, the GHASTLI setup suffers from two disadvantages. Again, much like the SPS, it lacks viewports. Additionally, the unit has thus far been used only in the two-phase hydrate growth regime. Because the systems studied are typically consolidated (to be more correct, they are compacted, with no headspace), water and gas must be forced through the system at run time. This causes large bubbles to form in the sediment matrix, thus precluding any single-phase dissolved gas hydrates from forming.

To address many of these issues, a device was designed and constructed which allows for visual, spectroscopic, acoustic, thermal, and pressure measurements of gas hydrates in sediment, and has the capability to do so using a single-phase (methane saturated water) condition or a flow-through, two-phase formation condition. It should be noted that spectroscopic work thus far has not been carried out, although the borosilicate glass used in the hydrate formation unit does not show Raman activity in the typical hydrate wavenumber range (2800 – 3100 cm^{-1}). Also, work is underway to add a biaxial stress hydrate formation vessel to the device, allowing for the study of hydrates using independently controlled confining and pore pressures.

3.2 The Flexible Integrated Study of Hydrates (FISH) Unit

The schematic of the FISH unit is shown in Figure 3.3. From right to left (inlet to outlet), it can be broken down into 3 sections: gas delivery and metering, hydrate formation and monitoring, and gas outlet and metering.

3.2.1 The Gas Delivery System

Gas at tank pressure (2200 psi, 15.15 MPa) is first stepped down to experimental pressure through an emergency on/off valve (GV1 in figure 3.3), and then to a pressure regulator. Both the inlet (tank) and outlet (post-pressure regulator) pressures are monitored via Omega digital gauges (source: Omega.com), marked PT1 and PT2, and values are fed into a custom-built LabView data acquisition system. Gas inlet into the actual hydrate formation system was allowed via valves GV3, GV5, and GV6 and metered via a Brooks Instrument mass flow controller, model 5850i. The NIST-traceable unit (see Appendix A for certificate) is capable of controlling gas inlet from 75 to 2000 ml/min at up to 4500 psi (31 MPa) with a 0.7% precision on the measured rate. For lower flowrates, a calibrated precision needle valve (GV6, normally left in full open position) was employed. For inlet flow greater than 2000 ml/min, GV3 and GV5 were closed and bypassed via GV4. While flow rates greater than 2000 ml/min were used in many of the experiments, metering of the gas was simply calculated by the rate of pressure change with time, and extracting the volumetric flowrate using the Redlich-Kwong-Soave (1972) equation of state, shown below in equation 3.1.

$$P = \frac{RT}{\hat{V} - b} - \frac{\alpha a}{\hat{V}(\hat{V} + b)}, \tag{3.1}$$

$$where\, a = 0.42747\frac{R^2 T_c^2}{P_c},$$

$$a = 0.08664\frac{RT_c}{P_c},$$

$$\alpha = \left(1 + m\left(1 - \sqrt{\frac{T}{T_c}}\right)\right)^2$$

$$and\; m = 0.048508 + 1.55171\omega - 0.15613\omega^2$$

Tc, Pc, and ω are the critical temperature, critical pressure, and accentric factor, respectively, of the entering gas (methane). T is the temperature, P is the pressure, and $\hat{V}$ is the specific volume at the given T and P.

3.2.2 Hydrate Formation, Dissociation, and Monitoring Unit

The main component of the hydrate unit is a high-pressure vessel fabricated from carbon steel. The unit, seen in figure 3.4, is based on a Jerguson liquid-level gage that has been retrofitted with several precision sensors for measurement of temperatures and pressures at various points along the unit, along with an inlet gas sparger. A top-down view of the cell can be seen in figure 3.5. The availability of different volume liquid-level gauges from Jerguson allows us to construct pressure vessels of different volumes and geometries: this gives an unprecedented flexibility to the unit. The physical wetted (internal) dimensions of the pictured pressure vessel (410mm length x 17mm width x 28mm depth) yields an internal volume of 198 ml (includes correction for all associated fittings).

The as-purchased materials for the pressure vessel were not been altered from original manufacturer's specifications: two steel faceplates, each 32 mm thick, made of cold-rolled steel AISI C1040 securing the tempered borosilicate glass windows, nuts and bolts are A194/A193 B7 alloy steel, respectively. The liquid chamber itself is made from machined bar stock, type ASTM A696. Manufacturer-cut gaskets, placed between the window and the surrounding steel body to prevent chipping and to ensure a complete seal, are made from Teflon. These were replaced occasionally between runs due to sediment abrasion and general wear.

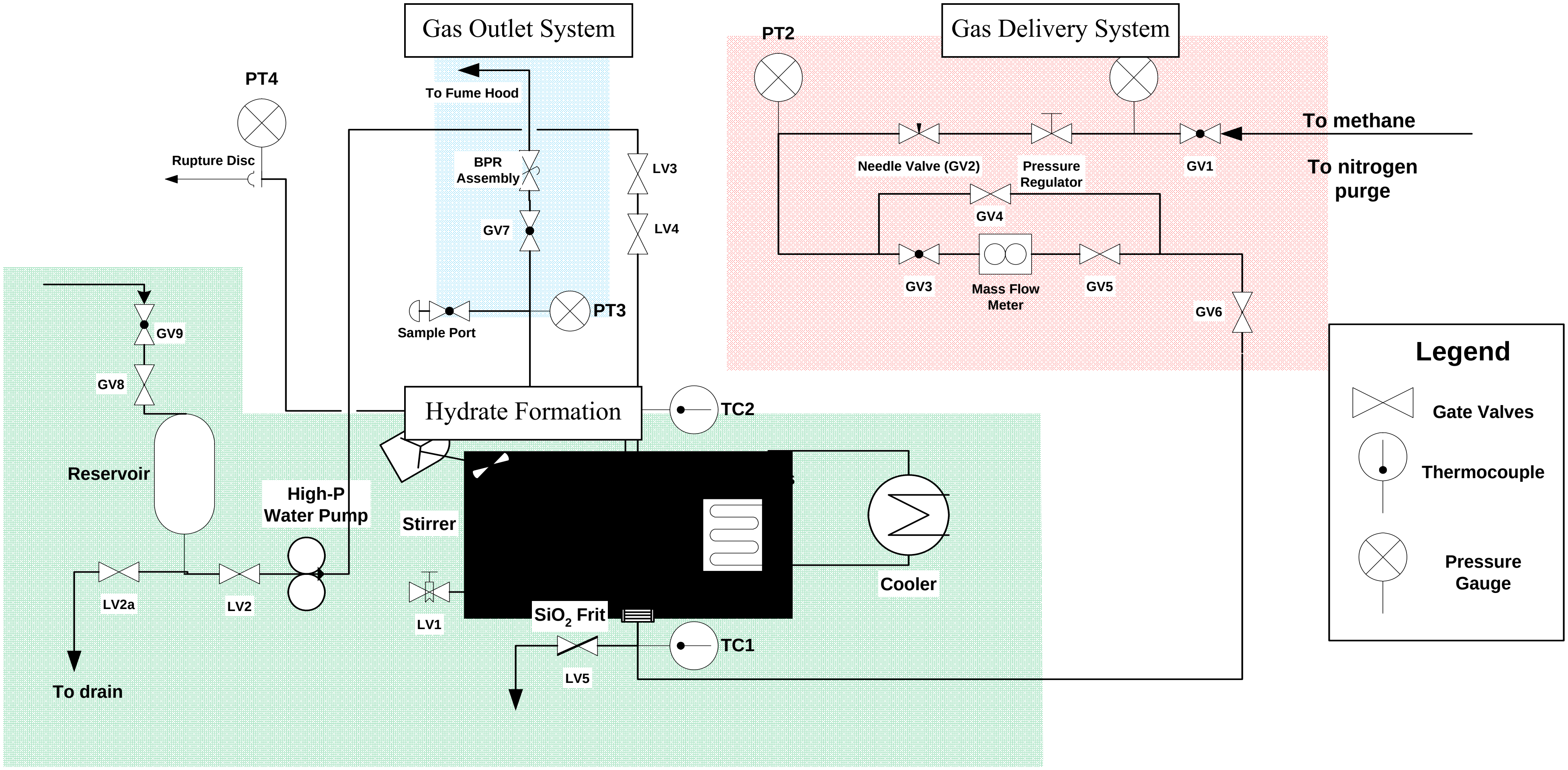

Figure 3.3 Process flow diagram for the FISH unit

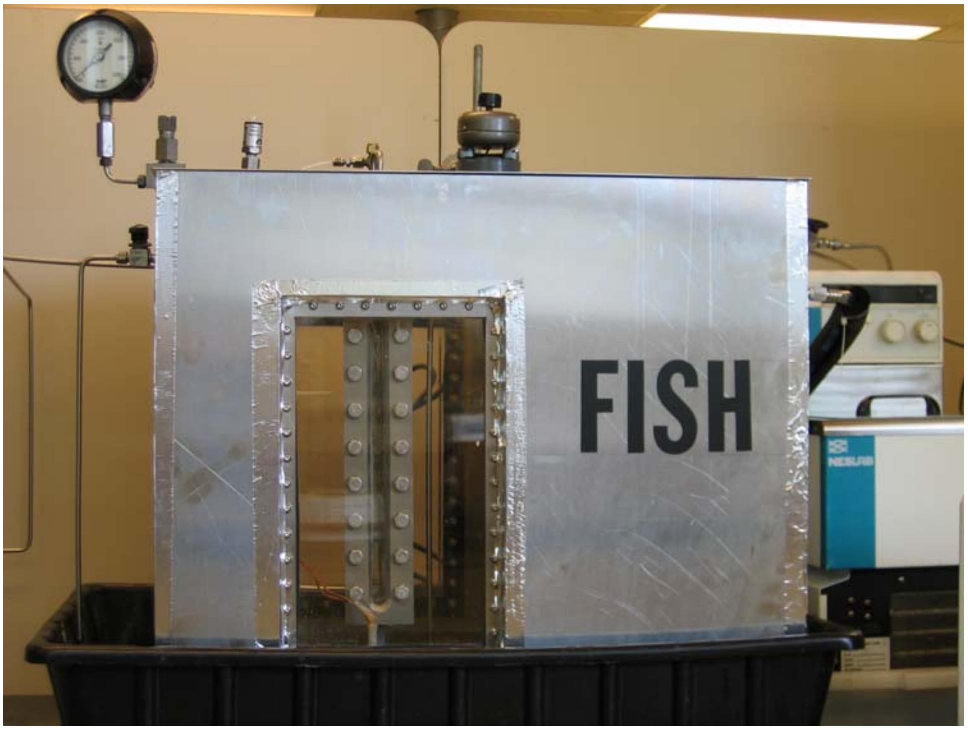

Figure 3.4 FISH unit with pressure vessel submerged in water bath

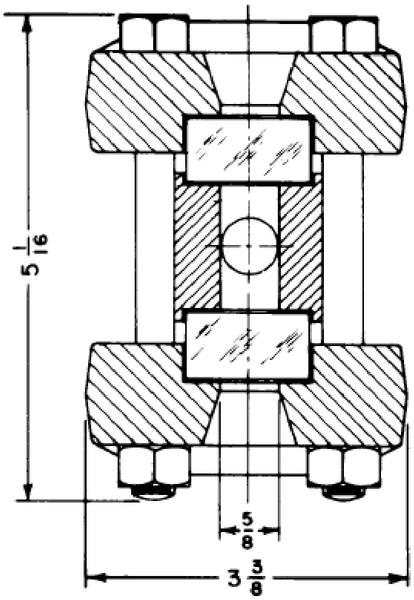

Figure 3.5 Top-down view of modified Jergeson liquid level gauge. Dimensions in inches

While typically held constant in all runs described herein, the gas-to-liquid volumetric ratio inside the cell can be varied by simply increasing the amount of sediment/water contained within the unit or by switching to the aforementioned different pressure vessels.

The vessel has rectangular viewing windows on two opposite sides constructed from borosilicate (rated to 20 MPa) and is immersed in a temperature-controlled water bath. These windows provided an ideal means for verifying, at least for the sediments and hydrates against the viewglass, hydrate morphology and growth character – having multiple views (front and back) of the cell increases this advantage further.

The gas inlet of the vessel (at the bottom) originally contained a custom sparger of fine glass wool sandwiched between two 70 μm stainless-steel sieves. The sparger was epoxied into a ½" Swagelok fitting, and checked between runs to ensure its integrity. A diagram of the sparger design can be seen in figure 3.6.

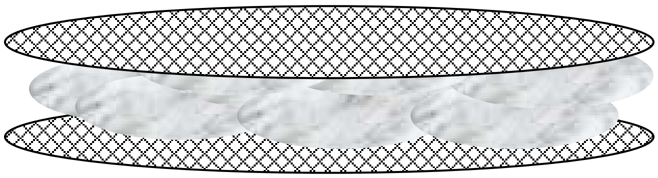

Figure 3.6 A cartoon of the custom gas sparger on the FISH unit

The sparger serves several purposes. First, it reduces or eliminates channeling in the sediment. Without proper attention to inlet conditions, large gas bubbles travel along the "path of least resistance" through the vessel, which is usually between the wall or glass viewport and the outside of the sediment sample. While some hydrates will form under these conditions, this type of hydrate formation is undesirable as only a fraction of the sediment contributes to hydrate formation. As the goal of the project is to simulate *in situ* conditions, a finer, more homogeneous packed-bed type flow was desired. Second, the sparger acts as a one-way valve, eliminating back flow of the water and sediment into the gas lines and averting a potential unwanted plugging condition. Upon recommendation from Dr. Robert Kleinberg, Schlumberger Doll Research **(**Kleinberg, 2006**)**, the custom sparger was replaced with a polyester supported Gore-Tex membrane, which allowed for finer gas distribution (pore size = 0.1 μm) and true hydrophobicity.

The main tank is cooled by means of a 500W Neslab digital RTE-111 chiller/circulator ('Cooler' in figure 3.3), which is filled with a 50/50 volume percent mixture of ethylene glycol and water. The rated temperature stability of the circulator was $0.01^{o}C$, though the temperature stability of the bath itself was, on average, less than $0.05^{o}C$, based upon measurements from thermocouples located in the bath, as well as in the cell. The water bath is approximately $0.45\ m^3$, and provides several advantages. First, the mass of the tank is very large. While it takes on the order of 20 hours to cool from room temperature to $2.5^{o}C$, it maintains a very (+/- $0.05^{o}C$) stable thermal mass to draw from or add energy to. This is advantageous not only experimentally, as forming and dissociating hydrates is an energetically dynamic process, but also in modeling – a constant temperature boundary condition often greatly simplifies calculations. Second, the water added a layer of safety in case of pressure vessel rupture (although several fail-safes are in place, as will be discussed later).

It should also be noted that Styrofoam "peanuts" (the type used as packing materials) were added to the exposed top of the water (not shown in figure 2.1) to add an extra layer of insulation. Although four out of the six sides of the FISH unit are insulated with 0.02m of Styrofoam, the "top" section of the tank remained open to the environment. Not only did this result in large water losses due to evaporation, but also thermal instability (+/- 0.3^{o}C). Adding the insulation at the top resulted in an order of magnitude greater precision on temperature control.

Finally, the tank has a stirrer (see figure 3.4, top) mounted to ensure homogenous mixing of the tank and prevent hot or cold spots inside the cell.

Two thermocouples are located inside the pressure vessel: one near the top and other near the bottom to measure and establish any temperature gradient along the length of the vessel during the hydrate formation/decomposition event. For all runs described herein, the top thermocouple measured only the gas phase temperature, while the bottom thermocouple measured the temperature of the water/sediment/hydrate mixture. The measurement location is approximately 10 cm from the bottom of the cell and is centered horizontally (both in width and depth) of the column. The temperatures of both the gas and liquid phases are measured with the aid of grounded ¼" (0.00635m) type K thermocouples from Omega (Omega.com, 2007). The thermocouples have a stated absolute accuracy of 1.1^{o}C from 0-20 °C based upon NIST monograph 175 (National Institute of Standards and Technology, 1993). Each was calibrated regularly using an ice-bath immersion to ensure high-precision measurements. It is important to note the difference between the absolute accuracy of the measurement and its relative accuracy (or, more importantly, the precision). While the thermocouples are guaranteed to within 1.5 °C, this simply indicates that a measured temperature, over time, will be within 1.5 °C of the "actual" temperature (in the case of the ice bath, 0 °C). However, a repeated measurement of a constant temperature or the measurement of a *change* in temperature will be influenced mainly by the precision or relative accuracy of a thermocouple and its attached hardware. In the case of our setup, the precision on the temperature measurement was taken to be 0.01 °C, based upon the fluctuation in a constant temperature environment, the ice bath. Finally, the response time of each thermocouple, as reported by Omega (http://www.omega.com/prodinfo/TC_Graphic2.HTML), is approximately one second. That is, for a step change in temperature, after one time constant the thermocouple will register 63.2% of the actual value. This is important because the measurement of formation and dissociation kinetics relies on changes in temperature and pressure with time (on the order of $10^2 - 10^4$ seconds), and such a rapid response indicates that calculations will not be limited by the thermocouple, as expected.

The pressure inside the vessel was measured by a differential pressure transducer, model PX4100-1.5KGV, also from Omega (Omega.com, 2007). The range on the device is 0-1500 psig (0 – 10.3 MPa), with a repeatability of 0.1% (1.5 psi or 10.3 kPa). In this setup, the pressure transducers measure bulk pressure, not pore pressure. This is important to note because pore pressure and bulk pressure can differ in consolidated constrained sediments, leading to a shift in hydrate equilibrium conditions inside the pores, and thus a shifted hydrate equilibrium overall in the sediment (Anderson et al. 2001, Clarke et al. 1999, Clennell et al. 1999). However, because the system uses unconstrained unconsolidated sediments (free to move and expand during hydrate formation), it is assumed that the bulk and pore pressure are equal. A bi-axial core holding device to measure constrained hydrate equilibrium is currently in the process of being built. In this case, pore pressure and bulk pressure may vary significantly.

The pressure transducers were zeroed based upon barometric readings at Brookhaven National Laboratory (http://wx1.bnl.gov/) before each run, although the error on the measurement (1.5psi) was an order of magnitude more than the typical daily variation in barometric pressure. No further calibration was performed.

As previously discussed, all pressure, temperature, and flowrate data were recorded using a LabView (www.ni.com) setup. A 24-bit, 32-channel data acquisition (DAQ) acquisition board (SCXI-1100) with cold junction compensation (CJC) and signal conditioning was used to acquire all data. This setup alleviated many problems in thermocouple acquisition with ambient electrical noise, as well extraneous voltage at the junction between the thermocouple and the DAQ board.

In order to support hydrate formation in the absence of a free gas phase, the FISH unit also has a high-pressure liquid pump (shown as a combination of reservoir and pump in figure 3.3) manufactured by Milton Roy. The pump is capable of delivering water against pressures of up to 5000 psi (34.5 MPa). Therefore, in the instance that the cell was entirely filled with sediment and gas-saturated water, it could be pressurized using only water from the pump, maintaining a single-phase formation condition.

3.2.3 Gas Outlet and Metering

Gas can be contained within the hydrate formation unit via valve GV7, or by operation of the back pressure regulator (BPR), seen in figure 3.3. A back pressure regulator works as follows: a diaphragm is held down by a force, either mechanical (an adjustable spring) or pneumatic (in the case of the FISH tank) in order to resist flow. When the force of the flow matches the spring/pneumatic force opposite the flow, the diaphragm ‘bleeds’ off excess gas until the forces are balanced. These are particularly useful devices where rapid expansion of gas may occur, as they serve as a safety valve to drain off potentially dangerous pressures. In hydrate formation and decomposition experiments, they serve as a means for a constant driving force. That is, if the back pressure regulator is set to 1200psi (8.27 MPa) and the cell is filled with gas, hydrates will never be allowed to form at pressures higher than 1200psi. Conversely, if the temperature was to rise and the hydrates were to dissociate, they would always dissociate at 1200psi. The BPR's important role in kinetic studies will become more apparent in later experimental chapters.

Gas exiting the BPR (i.e. the total volumetric gas output of the cell) was measured via a dry test meter (precision=0.005 ft^3, $1.42x10^{-4}$ m^3) from the American Meter Company. Digital video recordings were made of the dry test meter gauge, and via frame-by-frame inspection of the video, gas outlet rates (dissociation rates) could be extracted

In summary, a detailed design allowed us to build a hydrate unit at BNL with several capabilities unavailable in the two units that are in use elsewhere. In the following chapters, we now describe a series of runs that were performed to further the science associated with methane hydrates in sediments

Chapter 4: Effect of Sediment on Hydrate Growth and Formation Kinetics

As previously mentioned, the goal of this work is to understand the effect of sediments on hydrates. Although broad in scope, this statement may be broken down into three experimentally and industrially relevant questions, each pertaining to a different aspect of the hydrate "life cycle":

1) How does the sediment shift the formation conditions of the hydrate?

This question addresses the initial formation period of a hydrate deposit found in natural settings. The question is perhaps the most fundamental in understanding and recovering oceanic hydrates. As is well established, an addition of salt to ice lowers the temperature at which the water freezes, sediments have been predicted (and will be shown) to alter the pressure and temperature conditions at which hydrates form – forcing them to form at pressures higher than normal (for pure deionized water) for a given temperature. This consequence is of tremendous importance to hydrate prediction, as it establishes boundary conditions of temperature and pressure on the ocean floor for hydrate recovery.

2) How does the presence of sediments affect the morphology during hydrate growth?

This question is, perhaps, the most influential factor in determining economical energy recovery from hydrates. As shown in figure 1.8, natural hydrates have been found in a number of different growth configurations within the sediment, each with various degrees of economic potential for recovery (massive-type hydrates are the most favorable).

3) How does the sediment alter the rate, route, and amount of gas in a forming hydrate?

The question of hydrate formation kinetics has been troublesome to researchers for many years. System geometry, the inherent stochastic nature of hydrate nucleation, and sediment/particle quality all appear to alter results – a broad spectrum of hydrate formation models has been proposed (Proceedings of the Fourth International Conference on Gas Hydrates, 2002). While the question of *formation* kinetics is most important to those studying the geology and geochemistry of the oceans, the scale of such an occurrence, both temporally and spatially, preclude their emphasis. Instead, most of this work (chapter 5) will concentrate on the *decomposition* of hydrates within the sediment, and how factors such as sediment temperature, pressure, and driving force influence the rate of gas evolution. Not only does this play a role in direct energy recovery (i.e. understanding the optimum conditions to maximize gas outlet), but also in transporting hydrates (i.e. minimizing solid hydrate decomposition with minimal effort during shipment). However, in the interest of completeness, the formation kinetic data was collected and will be presented later in this chapter.

4.1 Experimental Methods

Due to the varying conditions of gas flux throughout the sea floor, several types of hydrate formation "methods" were used in the following studies. To simulate a high gas flux which, as mentioned by Ginsburg and Soloviev (1994), was indicative of massive hydrate accumulations, a "dynamic mode" of filling the cell (hereafter known as method 1) was employed. In this method, CH_4 gas (delivered at the desired formation pressure: 900, 1200, or 1500psi) continuously flows from the bottom in the pressure vessel during the hydrate formation event. The sparger creates tiny bubbles and as these bubbles travel upwards they continuously mix sediment, gas, and water. Although the bubbles do disrupt the sediment matrix, experimental limitations prevent the addition of gas by an alternate route. Care was taken upon charging to ensure no loss of sediment through explosive compression of the cell. The bubble size is controlled by the gas flow rate that itself can be precisely controlled by the mass flow meter. The system is held in an isothermal condition, and hydrates theoretically form as the pressure inside the system exceeds the equilibrium pressure.

The first step in refining method 1 was to investigate the effect that inlet gas flow rate had on hydrate formation. In nature, hydrates have much time to form, and often do so with limited resources -- gas formation by microbes/percolation through the seafloor occurs slowly. This achieves almost 100% conversion of the water/gas to hydrates, but does so over a period of thousands of years. However, due to the time scale of laboratory experiments, a compromise between accurate reproduction of *in situ* conditions and production of any quantity of data was necessary. Thus, a sensitivity study was initiated to achieve maximum hydrate production with maximum inlet gas flowrate (obtaining accurate results with the least amount of time). A mixture of 20ml of water and 60g of sediment (in this case, Blake Ridge) was loaded into the pressure vessel, and the apparatus was cooled down to $4^{o}C$. At this loading, the effective gas to liquid volume (V_g/V_l) ratio was kept constant at 1.86. The flexibility of the unit allows variability of the V_g/V_l parameter. Methane, at flow rates between 70ml/min and 2000ml/min was added to the cell until the desired pressure was achieved. No channeling was observed in the system at any flowrate; at high flow rates the sediment column was agitated to the point of fluidity, and at low flow rates the effect of the sparger was apparent – methane appeared to permeate the column uniformly.

Results of the sensitivity study are shown below in figure 4.1. It is important to note that thermodynamics are the "final" determining factor in hydrate formation. Given enough time, a certain quantity of water/sediment will hydrate a constant volume of gas.

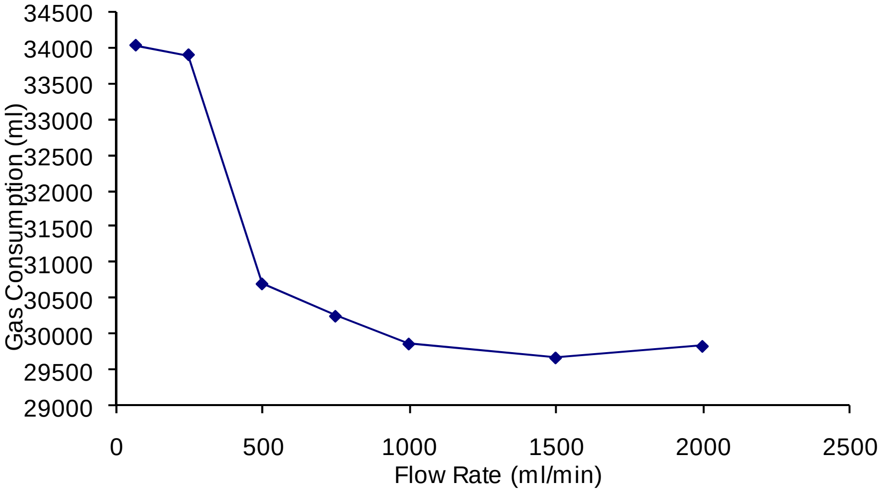

Figure 4.1 Hydrate gas consumption versus inlet gas flowrate

However, on the laboratory time frame, kinetics is the deciding factor. There are several notable features of figure 4.1. First, at high inlet flow rates (>1000 ml/min), the asymptotic decay suggests very little, if any, hydrate formation– most gas 'consumption' was probably due to simply filling the cell with gas. This is an expected behavior, as at high flow rates (superficial gas velocities greater than 0.035 m/s), there is very little gas-sediment-water interaction, and therefore the only hydrate-forming surface becomes the few square centimeters of the water-gas interface at the top of the cell (i.e. the bed has become fluidized, and gas holdup in between sediment particles is minimal). This interaction is more clearly demonstrated in figure 4.2, which is the theoretical gas hold-up in porous media, based upon work by Jamialahmadi (Jamialahmadi et al., 2005).

Second, the occurrence of another apparent asymptote at low flow rates (< 150 ml/min, or superficial gas velocities less than 0.005 m/s). This too is expected, because there is a physical limit to the amount of hydrate that can form (based upon gas holdup in the sediment) and therefore a limit to the amount of gas consumed (ultimately limited by the total available volume of water in the system). This result is encouraging, as it suggests that laboratory-scale experiments can approach the conditions and hydrate saturation level found in nature, but in a much shorter time.

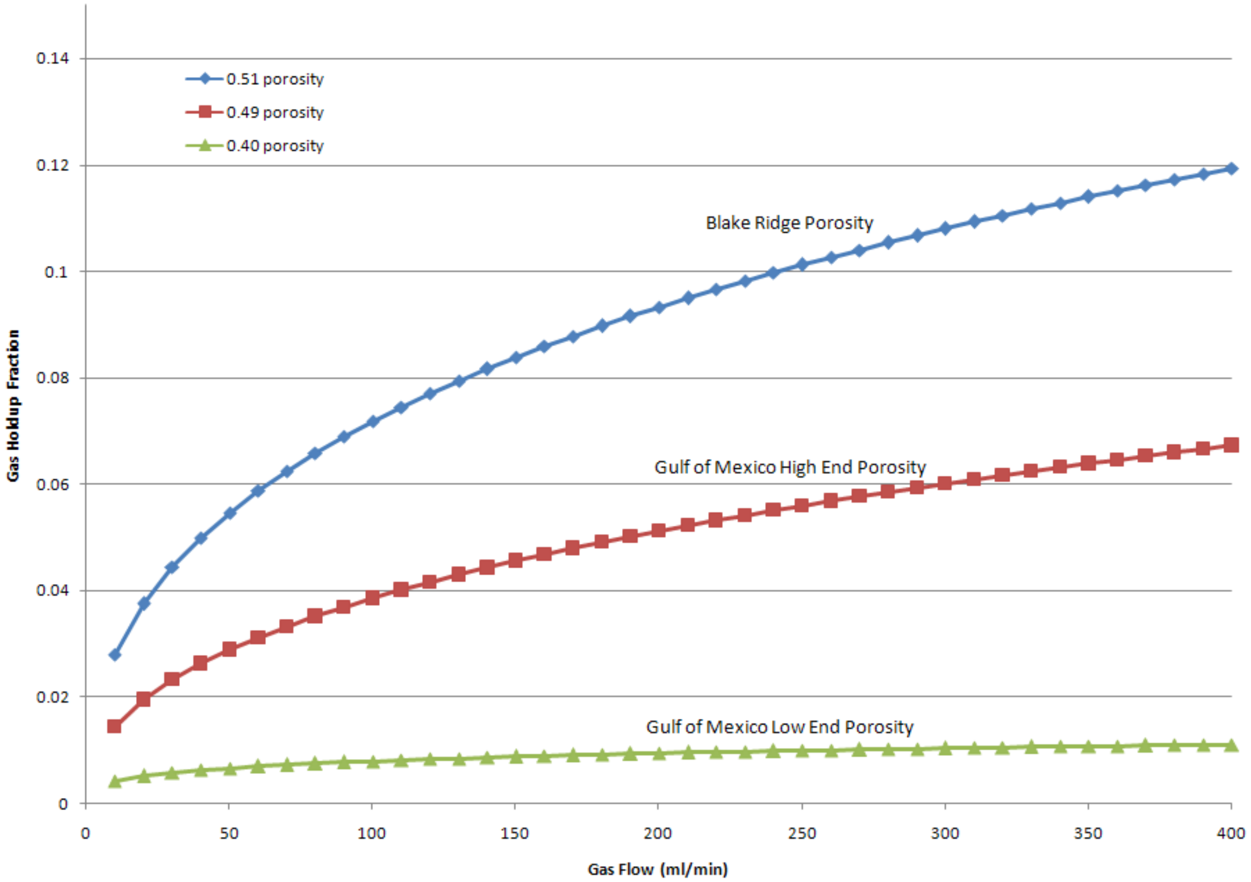

Figure 4.2 Predicted fractional gas hold-up in a porous system based upon superficial gas velocity and calculated liquid velocity.

Of note about figure 4.2 is the calculated liquid velocity. While superficial gas velocity can be simply calculated by volumetric flow of gas through the reactor/sediment, liquid velocity, when not experimentally measured, requires the use of a correlation for centerline velocity.

In this case, work by Zehner (1982) in bubble columns was used to estimate liquid velocities – see equation 4.1.

$$V_L(0) = 0.737 g^{1/3} D_T^{1/3} U_g^{1/3} \tag{4.1}$$

Where V_L is the centerline velocity of liquid, g is gravitational acceleration, D_T is the diameter of the column, and U_G is the superficial gas velocity. While the presence of sediment may alter the magnitude of the curve (by decreasing total liquid velocity), the shape is nevertheless the same, and may actually approach zero gas holdup at elevated flow rates due to churning/fluidization of the bed.

It is very interesting to see the order-of-magnitude difference in the gas holdup in figure 4.2 for the relatively (average 0.45) non-porous sediment of the Gulf of Mexico (JIP Cruise Report, 2005) compared to the larger, more porous Blake Ridge sample. Additionally, only a two percent change in porosity can almost double the gas holdup at the high end of gas flow rates. Note that calculations for flow rates higher than 500 ml/min were suppressed – at these flow rates, in a non-consolidated/compacted system, the bed becomes fluid and gas holdup is minimal.

Figure 4.3 shows a representative image of hydrate formation in Blake Ridge sediments using formation method 1 at low flow rates (<200ml/min).

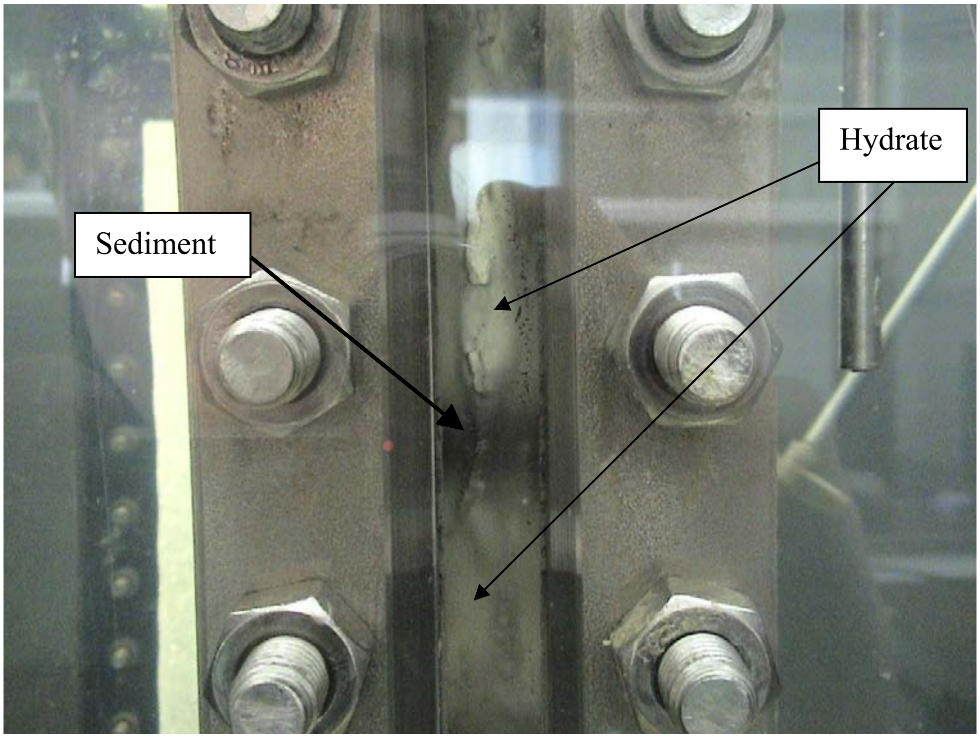

Figure 4.3 Hydrate formation under dynamic, low-flow charging conditions in Blake Ridge sediment

For clarification, the light colored (white/grey) substance inside the chamber is methane hydrate. The dark substance both trapped inside the hydrate and pressed against the borosilicate glass is Blake Ridge sediment. It should be noted that this outcropping of hydrate was approximately 10 cm long, about the size of the entire sediment/water column. Given its size, this type of formation would be considered “massive.” Indeed, as pointed out by Ginsburg, such formations typically occur in areas of high gas flux, which, in comparison to the relatively diminutive production of gas by bacteria, 200 ml/min of gas in 50 cm^3 of sediment and water certainly is. Although it will be shown later, such studies performed in the fine-grained Gulf of Mexico sediment yielded less dramatic results. Gas uptake and hydrate growth in all but the slowest (<75 ml/min) gas fluxes yielded very little hydrate outcropping (1-2 mm above the sediment column), indicative of very low gas holdup internally – most gas absorption was most likely due to hydrate formation at the sediment/gas interface at the top of the column. Such growth was seen in method 2 – static mode.

The static method is similar to the dynamic method except CH_4 gas is added very rapidly initially (>2000ml/min by bypassing the mass flow controller) to the desired system pressure. As gas in the gas phase diffuses into the sediment/water column and is hydrated, the overall pressure in the system decreases. To maintain a constant system pressure, metered gas is added to the system over the course of several weeks to maintain a constant driving force for formation. This method is more representative of the seafloor conditions where methane gas/water does not agitate the sediment and the methane hydrate formation phenomenon probably occurs mostly by diffusion. To our knowledge, this method has never been used before to make hydrates in the laboratory. Unfortunately, it is a relatively time-consuming process, and the vast majority of data reported herein rely on such a method for formation; the result of which is a group of experiments that took over a year of solid data collection to obtain.

Of special importance to the low-flow dynamic method described above is that hydrates were formed from liquid water in a gas-rich (two-phase) condition. In the case of the no-flow static condition, hydrates were formed from a single phase, with the guest molecule (methane) coming from dissolved methane in solution. Huo (2003), and more recently Winters et al. (2004) have cited this formation condition difference for discrepancies between laboratory and natural hydrates. An explanation of such a discrepancy could possibly be the changes in small cage occupancy seen with varying levels of the methane/water ratio at the time of hydrate formation. Of course, hydrate cage occupancy will alter lattice size, and hence the properties of the macroscopic hydrate formations in sediment. However, in most laboratory experiments, hydrates are formed from finely powdered ice, and the temperature is increased to stimulate formation. Because this does not accurately reflect oceanic conditions, we have chosen to use liquid water rather than ice as the starting water phase that interacts with methane in the FISH unit. Cage occupancy analysis has not yet been performed to determine if such a change will affect the laboratory/oceanic hydrate discrepancy, but lattice size is being investigated at NSLS/BNL.

While the formation method for hydrates in the cell is relatively straightforward (altering either temperature or pressure), the decomposition method is more complex, due to the number of variables to be tested for influence on dissociation kinetics. Kinetic models by Kamath et al. (1987), Selim and Sloan (1989), Clarke et al (2001), Moridis et al. (2005), and most recently Pooladi-Darvish and Gerami (2007) all incorporate the difference between the fugacity of methane in the bulk phase and the equilibrium fugacity of methane at the given decomposition temperature. In simple terms, not only do they account for the typical kinetic effects of temperature and pressure, but the aforementioned models also take into account the "driving force" for hydrate decomposition; a hydrate held just below its equilibrium pressure is predicted to dissociate at a different rate than one substantially *lower* than its equilibrium pressure. As such, we have devised a step-down pressure method to quantitatively measure CH_4 gas evolution during hydrate decomposition. In the step-down pressure method, the original pressure (typically between 6 and 10 MPa) is decreased in ~ 1.37 MPa (200 psi) increments and the evolved gas is recorded. The process is continued until the vessel is at an ambient pressure. Both, the quantitative gas release at a given pressure as well as the total gas evolution are recorded. The 200psi step was chosen to ensure the instantaneous pressure shock to the system would not overwhelm the capability of the back pressure regulator. Additionally, gas was released from the system to ensure that the 200psi steps would fall at regular intervals (0psi, ~75psi, ~150psi) below the predicted hydrate dissociation pressure. That is to say, if at a given temperature the hydrate was predicted to dissociate at 500psi, three separate experiments were done so that the system was maintained at 500, 425, and 350psi during hydrate dissociation. This allowed for verification of the effect of fugacity difference on hydrate dissociation rate. This method will become more apparent in chapter 5, which deals exclusively with dissociation kinetics, although it is introduced here for completeness in experimental description.

4.2 Growth Morphology

The most apparent factor, at least from a qualitative aspect of sediment's effect, is on hydrate macroscopic morphology. As mentioned in section 2.1, two different end members of the sediment scale were used in these studies. One, from Blake Ridge off the coast of South Carolina/Georgia, is a coarse grained, bimodally-distributed sediment, with over 10% of the particles classified as 'sand' (125 microns and above), even for deep samples of 667m below the mudline. The average particle size diameter for the Blake Ridge "deep" sample was 21 microns. The second sediment was a very fine-grained sample from the Gulf of Mexico, with an average particle size of 6 microns, and only 0.6% of the sample classified as sand.

Figures 4.4 through 4.7 show the difference in behavior for both types of sediments under method 2 (static) formation conditions. While the formation morphology for every single experiment (all temperatures and pressures) is not shown in the interest of space, the outcome for each was consistent for the individual type of sediment (coarse or fine grained), independent of the salinity of the water used.

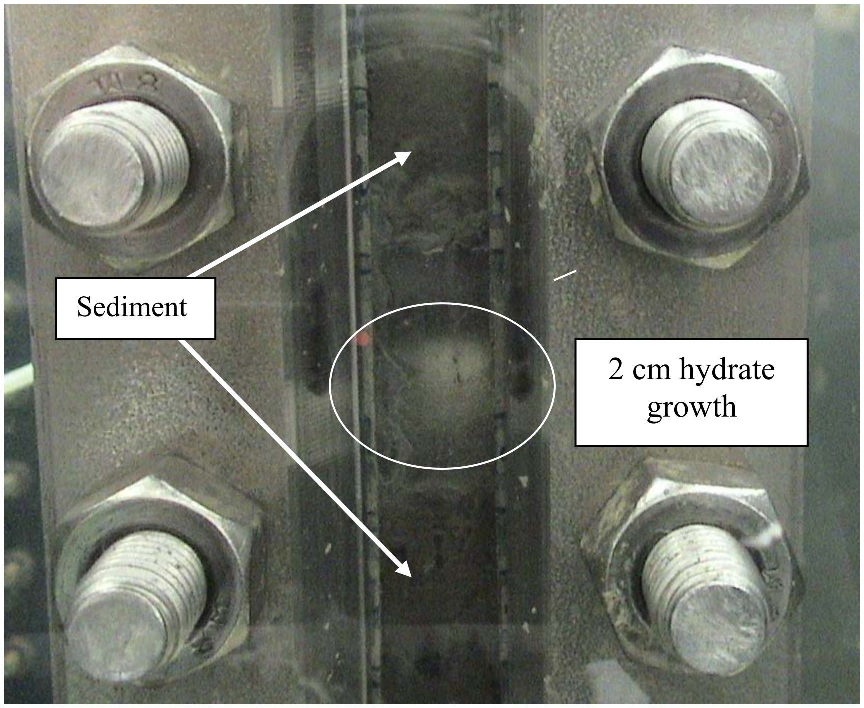

Figure 4.4 Methane hydrate formation in the 667m Blake Ridge host sediment under 2^{o}C and 1500psi static conditions. These hydrates are classified as “massive”.

Figure 4.5 Geometry of the host sediment subsequent to complete dissociation of methane hydrate formed in Figure 4.4.

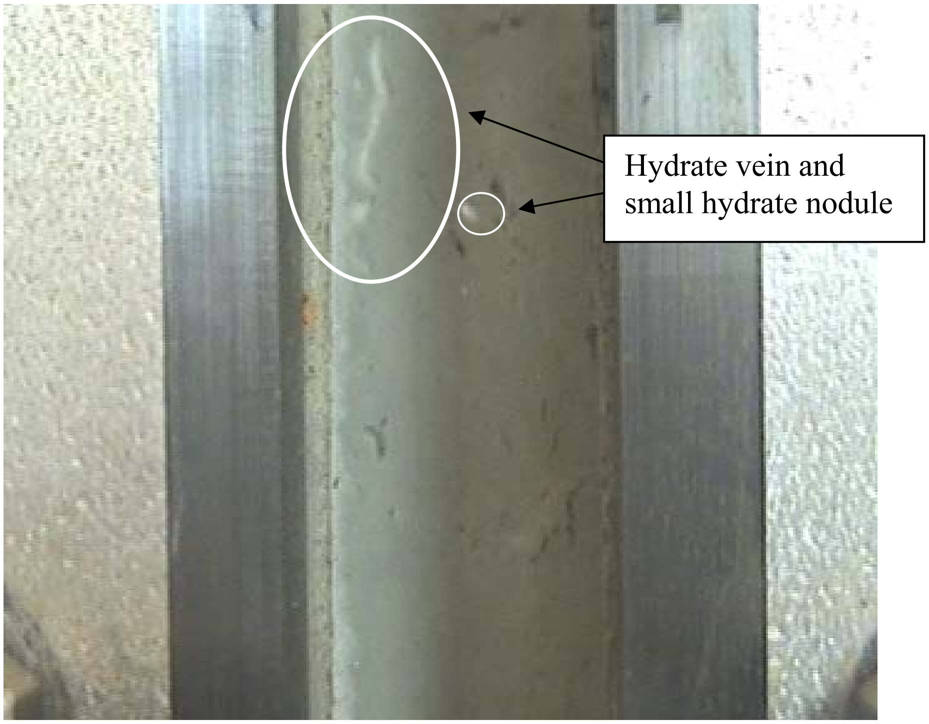

Figure 4.6 Methane hydrate formation in the Gulf of Mexico host Sediment at 2^{o}C and 1500psi conditions. This type of hydrate is classified as “nodular” or “vein-like.”

The difference between the modes of hydrate growth is evident. The more coarse-grained sediment appears to form much larger exclusionary hydrates; note the large void left behind in figure 4.5 from the dissociated hydrate. The finer-grained Gulf of Mexico hydrates are much less distinct and dispersed, and in most cases not nearly as evident. While lack of visual observation of hydrates in the fine-grained sediments might lead to the assumption that no hydrate was formed within the sediment, gas evolution and temperature measurements point to the contrary.

There are two points of caution which must be addressed with respect to figures 4.4 – 4.6. First and foremost, the assertion that one type of hydrate is “massive” and one is “disseminated” is essentially purely subjective. Currently, no *quantitative* size or particular shape classification exists for the different types of hydrates in sediments. Therefore, it is mainly the size difference between the two hydrate formations and the presence (or lack thereof) of visible voids upon dissociation that is cause for different identifications. However, given the scale of the “massive” formation compared to both the size of the unit, and the size of the “nodular/vein-like” hydrates, an argument can be made for such a classification. The second note of caution and one which will be addressed in future work with the FISH unit is in regards to sediment confinement. In all studies presented herein, confining stresses on the hydrate were minimal. That is, the sediment column was allowed to expand freely in the vertical direction upon hydrate growth. In deep oceanic sediments, hydrate growth occurs in a static sediment system, with hundreds of meters of sediment confining it. As such, pore space growth in the current system is expected to be minimized (figure 1.12, model 4), while hydrate outcropping/nodular/massive hydrate accumulations would be most likely – as is the case with mudline-type hydrates, as seen in figure 4.7

Figure 4.7 Massive mudline hydrates, Barkley Canyon, British Columbia, Canada **(**Monterey Bar Aquarium Research Institute, 2006**)**

4.3 Formation Kinetics

In the proceeding sections, all hydrate formation occurred in the Blake Ridge and GOM sediments via the static-charge mode. Similar amounts of sediments (57.8g) and water (57.1g) were used in each case. Experiments were performed at approximately 2, 6, and 10^{o}C, with initial charging pressures to 900, 1200, and 1500psi. Combinations of the conditions (sediment type, temperature, and pressure) were performed to ascertain the effect of each.

Experimentally, there are a number of well-documented factors which alter the formation of hydrate growth – the reader is directed to Chapter 3 of Sloan, 1998, for an excellent review of temperature, pressure, and inhibitor influence. However, most studies reported there have been performed under 'pure' conditions – that is, with deionized (DI) water and pure guests. More recently, the trend in hydrate kinetic research has shifted towards growth in porous/complex media, although much of such work has been performed using DI water and glass beads or other synthetic materials as the "host matrix." While this takes a step forward in calculating formation kinetics, the availability of natural, once hydrate-bearing sediment for use in experiments begs the use of even more complex systems. Early work with such systems is reported here.

There are two ways to follow the formation of hydrates. The first, which exploits the exothermic nature of hydrate formation, is the thermal "spike." At the moment of growth, the temperature of the medium surrounding the hydrates increases (assuming that experiments is performed under isothermal conditions) as the hydrate formation phenomenon is accompanied by a release of the predicted $2.9\text{x}10^9$ J/m^3 of energy **(**Ballard, 2002**)**. Of course, the temperature rise in the system will depend on a number of variables, most of which are rate dependent (e.g. rate of hydrate formation, rate of conduction/convection of heat away from the hydrate, etc). Additionally, depending on the thermal dynamics of the experimental system, such a "spike" may be sustained over an extended time, or may be unobservable due to slow hydrate growth or rapid transmission of heat from the newly formed hydrate. The second method of following the "pressure drop" relies on the formation of hydrates in a closed system. In a closed, isochoric system, as hydrates form, gas is extracted from the gas phase and trapped the more highly concentrated crystalline phase of hydrates. As such, the pressure of the experimental system drops. However, the way in which it drops is, as in the thermal spike indicator, characteristic to the experimental system. In this case, however, there must ***always*** be a decrease in pressure for a closed system concomitant with hydrate formation.

In distilled water, quiescent, unagitated hydrate systems show a slow, exponentially decaying pressure drop as hydrates first nucleate and slowly grow – the so-called “induction period” (Lekvam and Ruoff, 1993**)**. This can be seen in figure 4.8. In a closed system with a lack of nucleation sites, this type of slow pressure drop will continue as molecules in the gas phase diffuse through the newly formed solid hydrate “crust” – essentially being governed by mass transfer limitations. However, in an agitated system, constant liquid water to gas exposure results in rapid pressure drop, as the hydrate is no longer limited by slow gas diffusion through solid. This can be seen in figures 4.9a and 4.9b, which represent experiment and simulation of a quiescent-to-stirred system, respectively

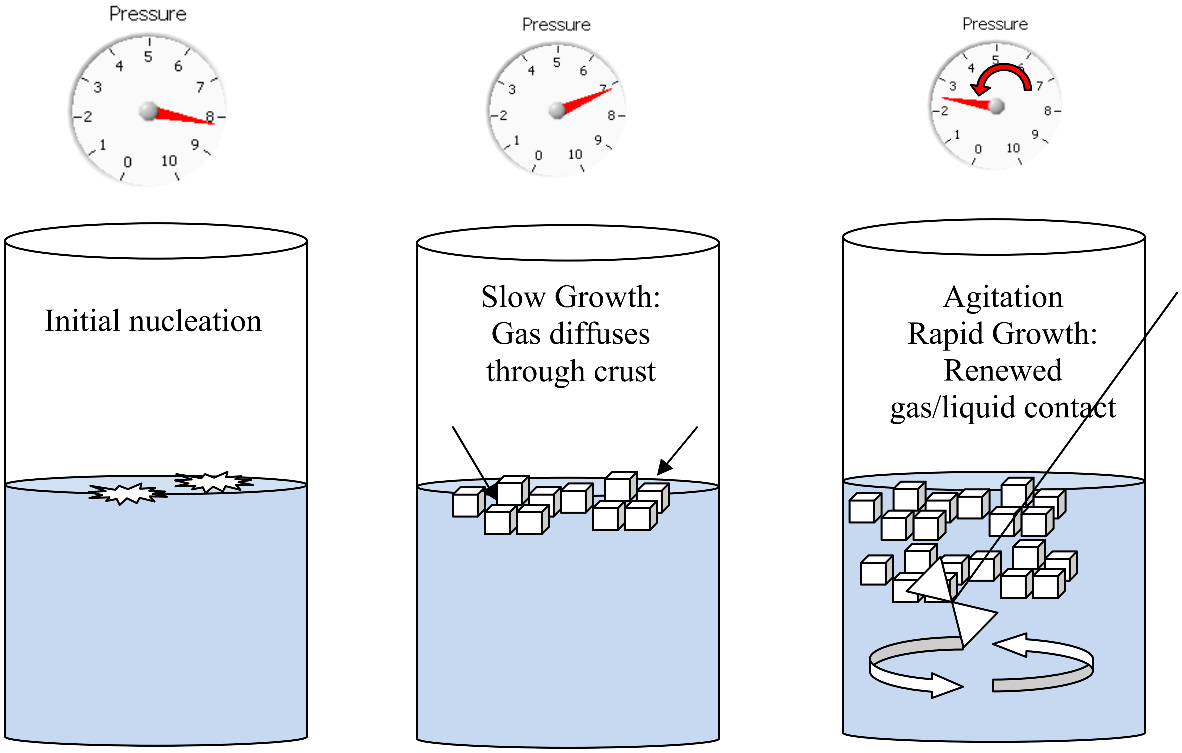

Figure 4.8 An animation of hydrate growth in a closed system with and without agitation

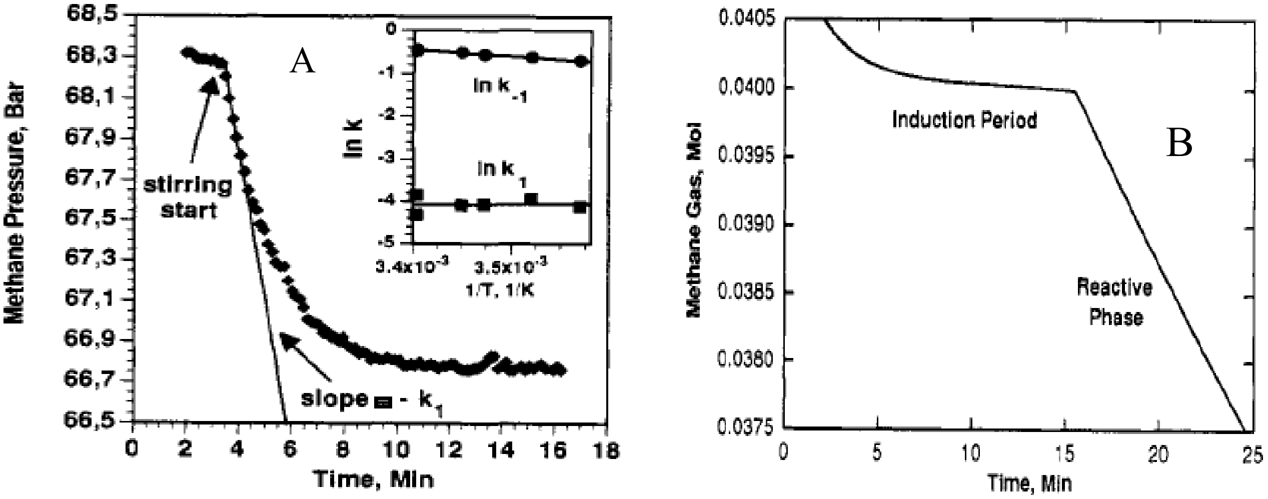

Figures 4.9a & 4.9b Gas pressure drop and theoretical consumption in a closed, agitated system (Lekvam and Ruoff, 1993**)**.

Additionally, hydrate formation may be visually verified, at least at the macroscopic level, in the FISH unit, and while it is not as quantitative, it compliments the above indicators and provides strong evidence for the presence of hydrates.

4.3.1 Dynamic Method

The formation of hydrates in the laboratory is subject to procedural constraints and no one method truly represents the natural systems. In this work, we devised two hydrate formation modes, static and dynamic, and both are discussed in detail in this chapter. Early work relied on the dynamic method: slow percolation of gas through the sediment column to the desired pressure. In this method, because gas was added long after hydrates began forming, the precipitous drop in pressure observed in closed systems was not, as expected, observed in this system. Formation was initiated by the introduction of gas into the system until the desired pressure was achieved (900psi -- 6.21 MPa, 1200psi -- 8.27 MPa, or 1500psi

-- 10.34 MPa). Formation pressures were arbitrarily chosen, but varied to ascertain the effect of formation pressure on formation and decomposition kinetics/thermodynamics. Once formation ended, as indicated by the cessation of gas consumption (inlet lines were left open), hydrates were held at a constant temperature and pressure for 48 hours, in order to allow for equilibration and possible further conversion. Figure 4.10 a, b, and c show typical temperature/pressure vs. time trace for the initial formation event. Note that during the 48 hour equilibration period, data collection continued, although no significant events were noted for any of the runs. For comparison, figure 4.11 shows the event in a pure water system at 1500psi; the loss of sediment mass was compensated for by the addition of extra DI water. It should also be noted that the dynamic studies were only performed in Blake Ridge sediments, as more quantitative data (the moment of hydrate formation/nucleation, total gas uptake, greater experimental control), at the suggestion of Professor Marco Castaldi, Columbia University (personal communication, 2006), could be obtained in a static system.

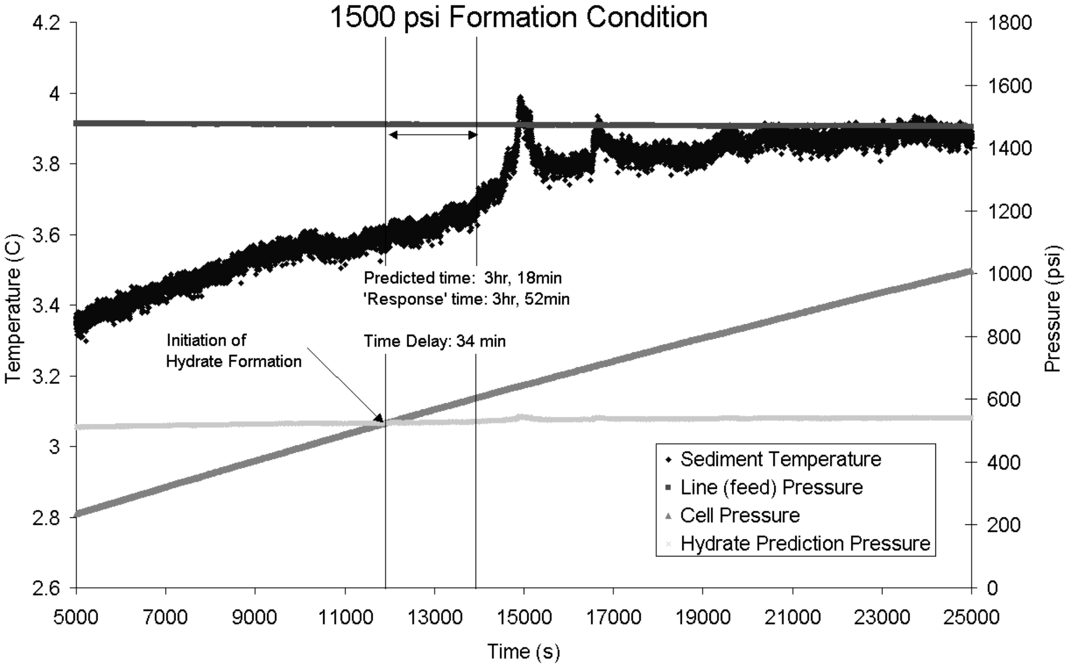

Figure 4.10a Temperature vs. run time trace for a 1500psi formation condition in the FISH unit.

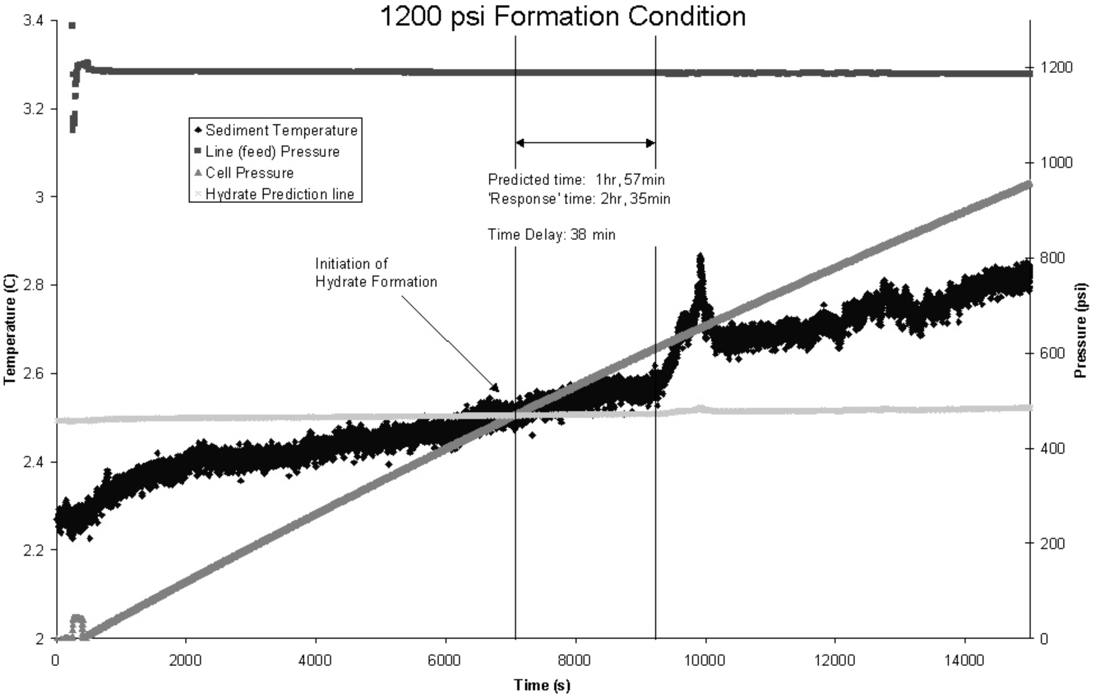

Figure 4.10b Temperature vs. run time trace for a 1200psi formation condition.

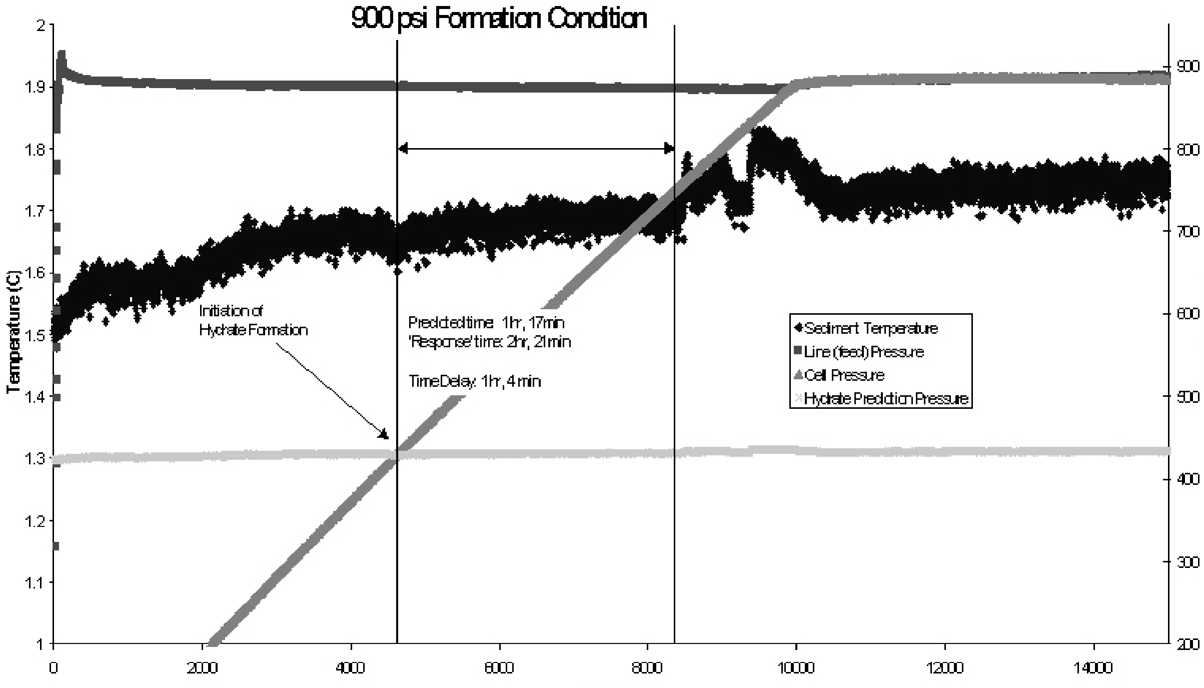

Figure 4.10c Temperature vs. run time trace for a 900psi formation condition.

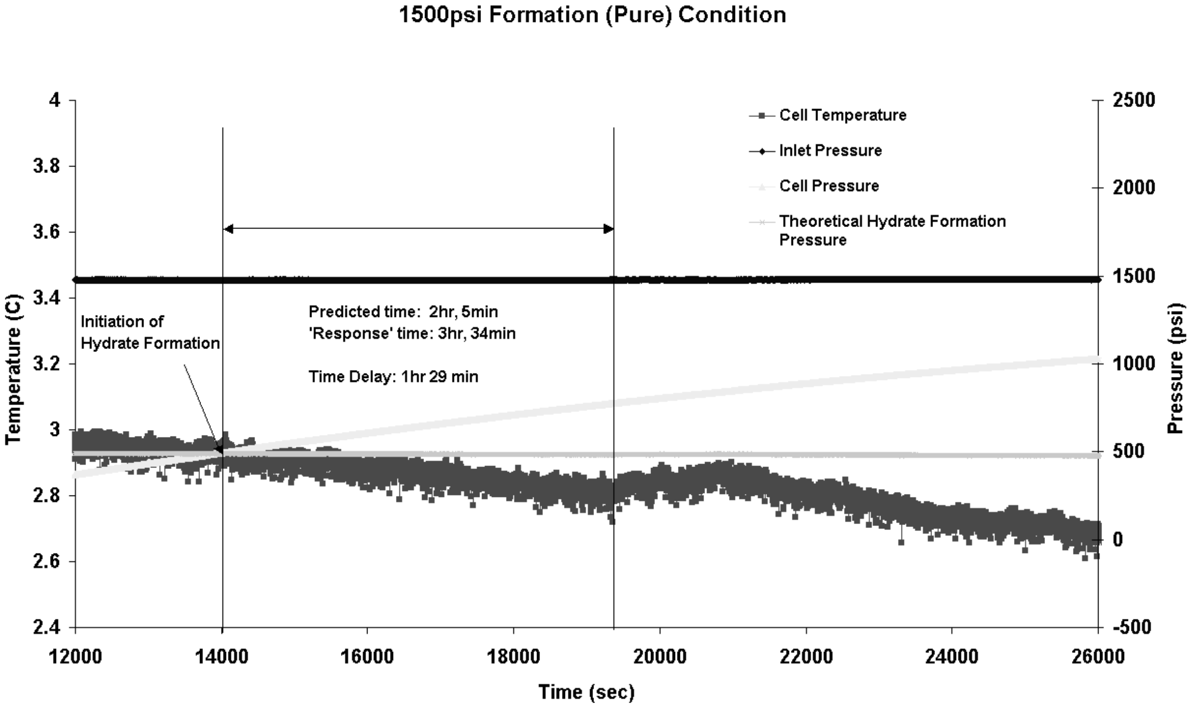

Figure 4.11 Temperature vs. run time trace for a 1500psi formation condition

During formation, it was observed that the temperature of the sediment in response to exothermic hydrate formation monotonically increased with formation temperature and pressure. From a fundamental chemical kinetics perspective, this is a logical outcome. If one were to treat the gas + water → hydrates as a chemical reaction (instead of a physical one), increasing the temperature (and, appropriately, the pressure) would result in a more rapid chemical reaction. As such, it is to be expected that the rate of formation of hydrate would increase with temperature (**and** pressure), and as the rate of heat removal by the sediment and bath are not as strongly dependent on temperature (linear or polynomial dependence, as opposed to the kinetic exponential dependence), the magnitude of the temperature spike would increase with increasing temperature. Outcomes for the Blake Ridge sediments are shown below in table 4.1. Additionally, the onset of the temperature spike was measured and found to be in agreement with the aforementioned theory on spike magnitude – that is, increasing the temperature increased the rate of hydrate formation, and therefore the temperature spike (the point at which the rate of hydrate growth and exothermic generation exceeded heat removal rate) occurred sooner.

Table 4.1 Analysis of temperature spike magnitude and time of appearance vs. formation pressure

Sediment	System P psi	Bath °C	Est. t, min	Actual Spike, t, min	Δt	T Spike °C
Y	900	1.8	70	141	1:11	0.18
Y	1200	2.6	117	155	0:38	0.32
Y	1500	3.5	198	232	0:34	0.40

Note the far lower temperature spike, however, in the 1500psi “pure” case, despite the similar temperature to the case with sediment (~3^{o}C). An explanation may rest in the nucleation capability of a pure DI system. That is, without a means of gas hold up, as seen in figure 4.2, and without the abundance of nucleation sites (the sediment), hydrates formed in DI water simply form more slowly and in areas not initially detected by the base-mounted thermocouple, resulting in a slower onset and lower magnitude temperature spike.

4.3.2 Static Mode Formation

In a static formation mode, gas is rapidly charged to the system: upwards of 30 liters of gas in approximately 1 minute are introduced. Such a fast fill results in much different behavior than dynamic filling:

1) The sediment bed was fluidized, resulting in low gas holdup.

2) The majority of gas/liquid contact was at the top of the sediment column, as opposed to throughout the entire volume, resulting in slower hydrate growth (less nucleation sites and mass transfer area)

3) The rate of hydrate formation in the system was slowed to the point that a temperature spike (see figure 4.10) could not be seen. The hydrate formation, however, was readily confirmed via the corresponding pressure drop

Such behavior very much resembles the left and center animations in figure 4.8. However, there is a major difference between current kinetic models in pure water (figure 4.9) and this system: the rough sediment particles serve as ideal nucleation points for hydrate growth. Additionally, a sediment/water matrix is porous. So, while hydrate growth in a quiescent system containing sediments may be slow, it will be shown that hydrate growth in such a system, especially in the case of more porous sediments such as those from Blake Ridge (with added gas hold up), occurs faster than simple "gas diffusion through water and sediment" predicts and should allow.

As the remainder of this section is focused on comparisons of true hydrate formation to that predicted by theory, it is helpful to first briefly review diffusion.

Adolf Fick first derived his laws of diffusion in 1855 (Fick, *1855*). His second law is used in transient diffusion problems (i.e. when the concentration of diffused material changes within the diffusion volume) and is written as in equation 4.2:

$$\frac{\partial c}{\partial t} = D\frac{\partial^2 c}{\partial x^2} \tag{4.2}$$

where c is the concentration of the diffusing species, t is time, x is the one dimensional distance into the diffusion volume, and D is the diffusion coefficient – essentially a measure of how easily the diffusing species passes into the diffusion volume.

However, several modifications must be made to such an equation to more appropriately model the situation of the static mode of hydrate formation in a reactive system. First and foremost is a generation/consumption term that must be added in to account for the consumption of dissolved methane into the hydrate phase. It can be modeled in a number of physically reasonable ways, but this work will concern itself with treating the consumption of dissolved methane (or guest gas) as a simple first-order elementary reaction, yielding:

$$\frac{\partial c}{\partial t} = D\frac{\partial^2 c}{\partial x^2} - kc \tag{4.3}$$

where k is the specific reaction rate of formation. A note of caution regarding the use of this variable, which echoes that made by Yuri Makogan (Makogon and Holditch, 2001): the kinetic rate constants for hydrate dissociation and the models used to determine them should only be used for finding hydrate decomposition, and not used to predict formation. As such, this work uses, as a first approximation, overall kinetic rate constants obtained by Kono et al., 2002, which were obtained from methane gas hydrates formed in porous, synthetic sediments. Its value, which will be refined later, is on the order of 2.07×10^{-4} min^{-1} for a mixture of glass and ceramic with an average particle size of 50 microns – on par with those particles in both the Gulf of Mexico and Blake Ridge sediments.

Finally, as an added degree of realism, D_s, the diffusion coefficient of methane through wet sediment, was modeled after work by Iversen and Jørgensen as:

$$D_S = \frac{D_o}{1 + n \cdot (1 - \phi)} \tag{4.4}$$

where D_o is the diffusion coefficient of methane in standard seawater, Φ is the sediment porosity, and n=3 for clay-silt sediments or n=2 for sandy sediments. For reference, D_o is assumed to be 8.7×10^{-5} cm^2s^{-1}.

After combining all modifications to Fick's second law, one is left with the partial differential equation:

$$\frac{\partial c}{\partial t} = \frac{D_o}{1 + n \cdot (1 - \phi)} \frac{\partial^2 c}{\partial x^2} - kc \tag{4.5}$$

In order to solve this system analytically, several assumptions must be made. First, at the sediment/water boundary, for all times greater than t=0, there is some concentration of methane, c^*. Additionally, the concentration of methane in the water initially is 0, and at the bottom of the sediment column the concentration is fixed at zero. Although these last two assumptions are most certainly not fully valid (the water throughout the column had *some* methane dissolved in it before filling, and the bottom of the sediment column definitely had methane, given that the inlet to the system was located at the bottom), the dissolved concentrations were small in comparison to the concentration of gas in the head space. Mathematically, the boundary conditions may be listed as:

$$\begin{gathered} c = c^*, x = 0, t > 0 \\ c = 0, x = 0, t = 0 \\ c = 0, x = \infty, t > 0 \end{gathered} \tag{4.6}$$

The solution to such a problem was first proposed by PV Danckwerts in 1950 (Danckwerts, 1950) and is presented here with intermediate steps suppressed. Also note that the solution to such a problem relies on a steady-state value for the kinetic rate constant. That is, k may not change with time. In a relatively isothermal system (<1°C change), this assumption is valid. For a more complete treatment using a Green's function method for transient solutions, the reader is directed to work by Vrentas and Vrentas, 1987.

The concentration profile with respect to time and distance in the sediment column may be written as:

$$\frac{c}{c^*} = \frac{1}{2} e^{-x\sqrt{\frac{k}{D}}} \cdot erfc\left(\frac{x}{2\sqrt{Dt}} - \sqrt{kt} \right) + \frac{1}{2} e^{x\sqrt{\frac{k}{D}}} \cdot erfc\left(\frac{x}{2\sqrt{Dt}} + \sqrt{kt} \right) \tag{4.7}$$

where erfc represents the complimentary error function, or 1-erf(x), and c represents the concentration along the length of the bed. It should be noted that although the diffusion coefficient depends on the degree of hydration in the system and also on the porosity of the system, these expansions were not shown in equation 4.7 in the interest of simplicity.

Differentiating equation 4.7 with respect to x and analyzing its value at x=0, one may obtain the rate of change (and, consequently, the rate of absorption per unit area of sediment) at the surface of the gas/sediment interface as:

$$\frac{dQ}{dt} = -D\left(\frac{\partial c}{\partial x} \right)_{x=0} = c^* \sqrt{Dk} \cdot \left[erf(\sqrt{kt}) + \frac{e^{-kt}}{\sqrt{\pi kt}} \right] \tag{4.8}$$

Finally, calculating the total quantity absorbed in a given time, t, may be obtained by simply integrating equation 4.8 with respect to time, as seen in equation 4.9.

$$Q = c^* \sqrt{\frac{D}{k}} \cdot \left(\left(kt + \frac{1}{2} \right) \cdot erf(\sqrt{kt}) + \sqrt{\frac{kt}{\pi}} e^{-kt} \right) \tag{4.9}$$

Of course, one may then use the value of Q, the number of moles absorbed in a given time, t, to also calculate the corresponding pressure drop in the head space above the sediment/water mixture. This is easily done by taking n, the initial moles of gas in the charged system, and subtracting Q, the moles entering the sediment column. This value can be inputted to an appropriate cubic equation of state (such as the aforementioned RKS) using the headspace volume and isothermal temperature to calculate a new system pressure at any time. Figure 4.12 is a theoretical calculation for moles of methane gas absorbed/hydrated, as well as the corresponding pressure drop in the system over the course of 10 days in a system held at 1500psi and 277K

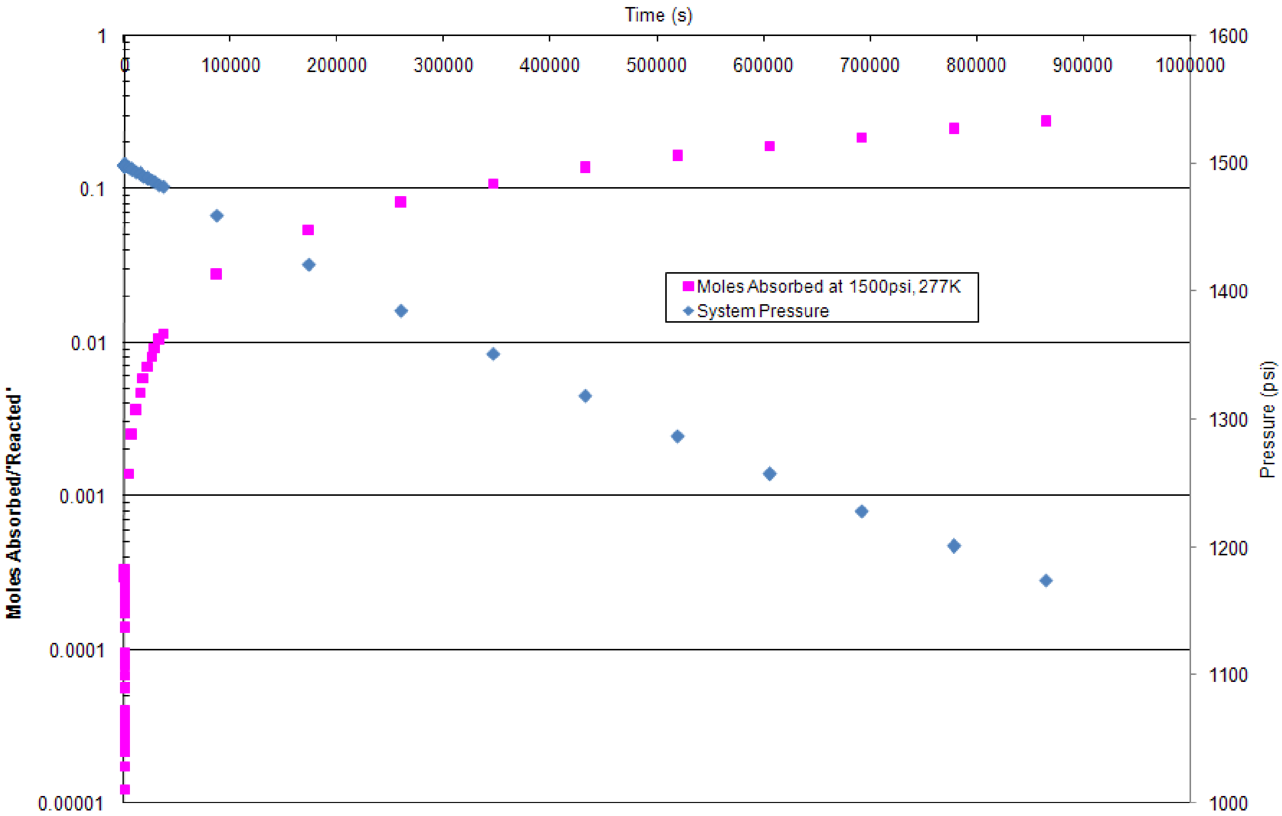

Figure 4.12 Theoretical methane absorption and hydration with time using Danckwerts' solution

It should be pointed out that the value used for the kinetic rate constant was the aforementioned value from Kono et al. 2002. Note that the figure displays the typical character for mass transfer/diffusion problems; that is, a solution involving an error function often involves a rapid increase or decline in concentrations, followed by an asymptote at extended time scales. This nature is further demonstrated in Figure 4.13, which shows the concentration profile in the sediment system at a time of 10 days (8.64 x 10^5 seconds).

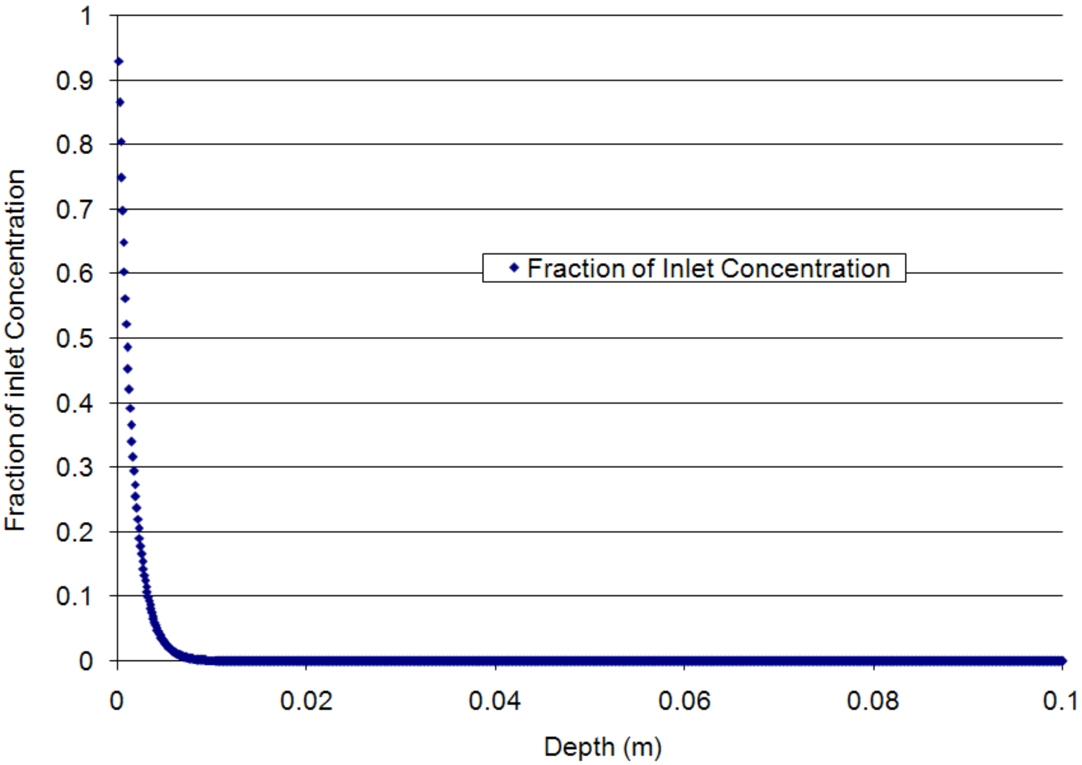

Figure 4.13 Theoretical methane concentration profile in sediment/water system after 10 days

It is clear that even after extended periods of time, the concentration front does not move more than a few centimeters into the sediment column. This is suggestive of a highly mass-transfer limited process; that is, reducing the kinetics by several orders of magnitude causes the concentration profile to become more linear and progress deeper into the sediment. As will be seen in the dissociation data, however, a significant amount of hydrate exists at levels of 5-10cm into the sediment column (enough to cause a temperature effect upon dissociation) and therefore mass transfer of methane *solely* by diffusion into a packed sediment column is not the only means of hydrate formation.

It is worth discussing c^*, the “maximum” boundary condition value for inlet concentration. While gas may be inputted to the cell at very high concentrations (i.e. at 1500psi and 277K, the concentration of gas in the headspace is 5.53 moles/liter), the maximum holding capacity of methane in water or sea water is much more limited due to the limited solubility of methane gas in such systems. As such, c^* used in all subsequent calculations is based upon maximum liquid solubility at system conditions. It is well known that gas solubility increases as the temperature of a solution decreases (a carbonated beverage is much more effervescent if it is cold). However, the system in question also has a major factor driving gas into solution – very high pressures. In fact, in a 1990 work by Y.P. Handa (Handa, 1990), methane gas experienced a 75-fold increase in solubility as pressures were increased from 1 to 100 bar. Figure 4.14 is a 3-dimensional representation of methane solubility as a function of both pressure and temperature.

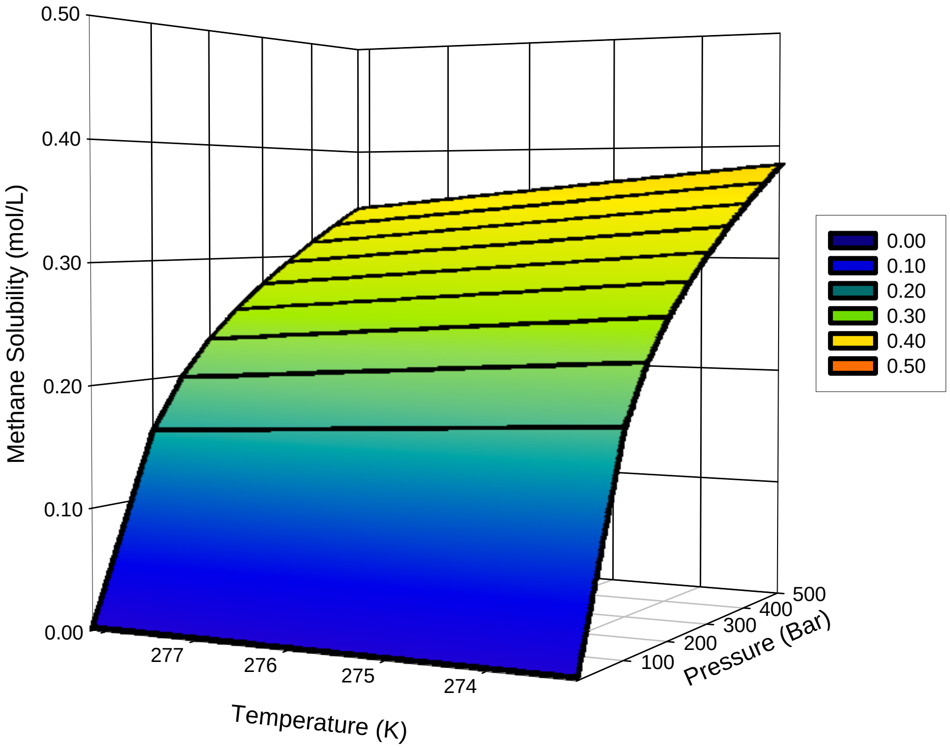

Figure 4.14 Methane solubility as a function of pressure and temperature in water

An equation describing such a surface was found using the package SigmaPlot and is:

$$\text{Solubility}(mol/L) = a \cdot (\ln(P) \cdot T^{-2}) + b \cdot (P^{-.5} T^{-.5}) + c \qquad (4.10)$$

where P is in bar and T is in Kelvin, and the constants are:

$a=1.001\text{x}10^{4}\,\text{K}^{2}$
$b=8.118\ \text{Bar}^{0.5}\,\text{K}^{0.5}$
$c=-.4854\ \text{mol/L}$

Formation experiments were carried out under a variety of different conditions, summarized in table 4.2 below:

Table 4.2 Summary of all formation conditions

Pressure (psi) / Temperature (C)	900	1200	1500
2	DI - BR, GOM	DI - BR, GOM	DI x 3 GOM Salt x 3 GOM
6		DI x 2 GOM	D GOM
10			D GOM

In table 4.2, BR and GOM represent Blake Ridge and Gulf of Mexico Sediments, respectively. In both sets of experiments, 57.78 g (arbitrary) of sediment were used, and 57.10g of water were used – the water amount was chosen based upon amount of water lost after drying/desiccation, and total water necessary to achieve complete saturation of the sediment column. Experiments performed in triplicate represent those done as a consequence of testing the rate of dissociation as a function of fugacity (shown in chapter 5). Additionally, DI represents those experiments performed using deionized water, while salt (at 2^{o}C and 1500psi) represents work done in salt water. Notice also that conditions such as 900psi and 10^{o}C were not studied – this is a consequence of the methane hydrate instability at elevated temperatures. The equilibrium curve for methane hydrate in both pure and salt water is shown in figure 2.3, but is recast in figure 4.15 in terms of pressure for clarity. Note that the equilibrium curves for both pure and salt water methane hydrates follow a typical vapor pressure curve (modified Antoine's equation) above 0^{o}C, but for the sake of future computation, a simple polynomial fit which achieves better that 0.2% accuracy was chosen. Also, as is apparent, salt water shifts the predicted equilibrium pressure by a noticeable degree, the magnitude of which increases at increased formation temperatures. This effect will be a confounding factor in later dissociation studies, discussed in chapter 5.

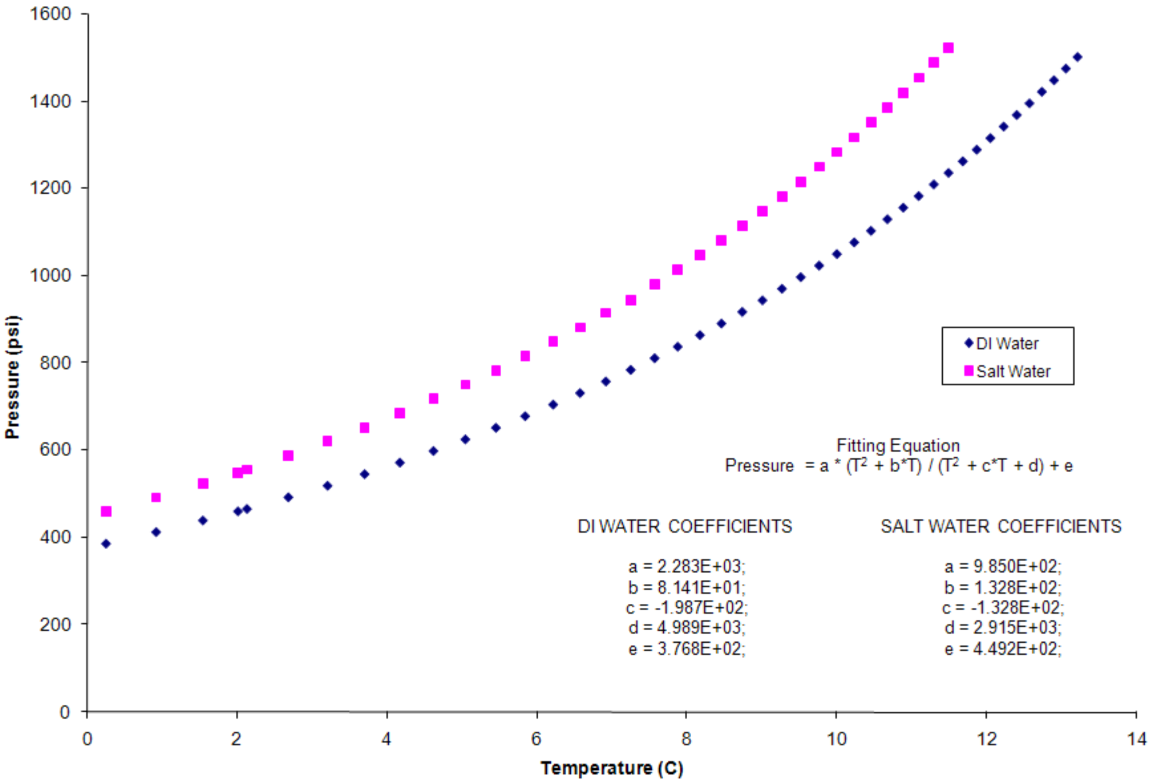

Figure 4.15 Hydrate Equilibrium Pressures in DI and Salt Water (4.02 wt%)

Salt water used in the formation experiments (41.953 g/L) conforms to American Materials Standard D-1141-52 formula A, 1.025 g/ml density at 15^{o}C, and having the composition shown below in table 4.3. Ideally, true seawater, with all of its impurities and biological contaminants would have been used, but for the sake of cost, repeatability, and reliability, a laboratory-prepared solution was used (Makogon and Holditch, 2001).

Table 4.3 Sea Salt Composition Used in 'Salt Water' Experiments

Compound	% Mass
NaCl	58.49
Na_2SO_4	9.75
KCl	1.645
KBr	0.238
H_3BO_3	0.071
$SrCl_2 * 6\ H_2O$	0.095
$MgCl_2 * 6\ H_2O$	26.46
$CaCl_2$	2.765
$NaHCO_3$	0.477
NaF	0.007
Brine pH	8.2

The first of the 3 formation conditions, 900psi, is shown below in figure 4.16. Note that for the Blake Ridge static formation conditions, temperature was held at 2°C in initial experiments, and only after studies transitioned to Gulf of Mexico sediments was the formation temperature varied. Work in Blake Ridge sediments using the dynamic mode of filling had shown an increased rate of formation with increased temperature, and work was begun on Gulf of Mexico sediments shortly thereafter. However, once it was observed that increasing the temperature of formation using the *static* mode to charge the cell yielded little in the way of increased reaction rate (due, in part, to the enormous mass-transfer limitations posed by diffusion), multiple formation temperature runs were not performed on Blake Ridge sediments. Such large mass transfer limitations effectively "cancelled out" any effective changes in reaction rates due to the presence of sediment. That is, reactions proceed so quickly than any gas present in solution was immediately used in the physical transformation to hydrates – thus, the reaction proceeded only as fast as the gas diffused into the column.

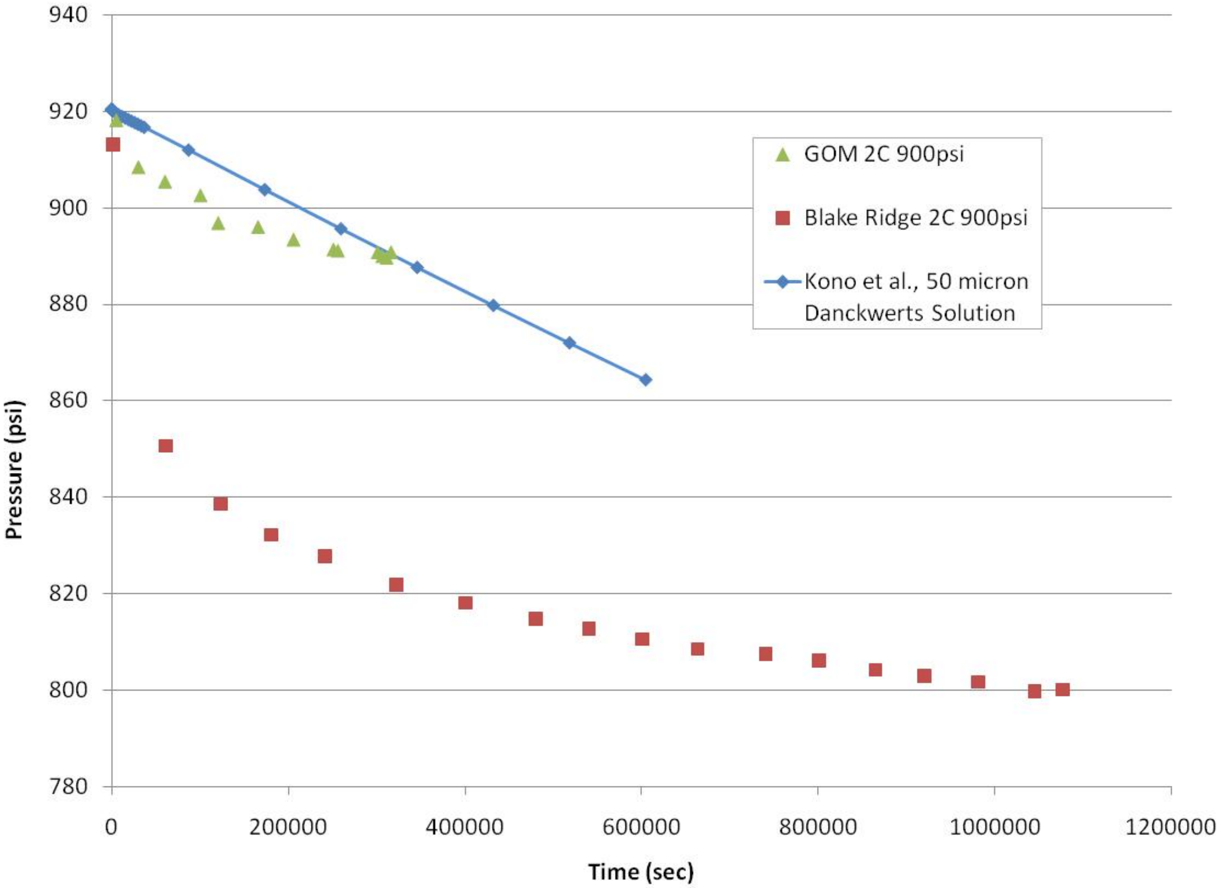

Figure 4.16 A comparison of pressure drop under 900psi, 2^{o}C hydrate formation condition in the Gulf of Mexico and Blake Ridge Sediments as hosts to the theoretical mass-transfer calculations

Figure 4.16 shows a consistent trend that will follow in the 1200 and 1500psi formation conditions. First, it should be noted that the line represents the pressure drop in a system calculated by equation 4.7; that is, in a system that is highly mass-transport limited (i.e. the rate of reaction far exceeds the rate of diffusion) with kinetic rate constants obtained from Kono et al (2002). Note that the very non-porous sediment, that of the Gulf of Mexico, very closely follows underneath this theoretical trend (maximum deviation -10psi). It did, however, begin to asymptote at a time of 3 days, and after 3 days and 12 hours, the experiment was halted due to the apparent lack of continued formation, as indicated by further pressure drop. While thermodynamics dictates that given sufficient pressures at appropriate temperatures, all water in the system should turn to hydrates (stopping at a pressure of 440psi due to equilibrium), such changes in the absence of agitation are diffusion driven and that may take on the order of years. Another startling trend in figure 4.16 is the amount of pressure drop in the Blake Ridge sediment. Such a system, in relation to theory and the Gulf of Mexico sediments, either has: a) a much higher intrinsic diffusion rate or b) a much higher porosity (increasing the overall diffusion coefficient) after charging with gas than the original as-tested sediment. The second option seems much more likely. As gas travels through the sediment column, even at high velocities, some gas is trapped and (most likely) hydrates. There is strong evidence to support this in our dynamic mode scenarios. Additionally, fluidizing the bed may result in less-than-optimal packing upon settling. Both of these things contribute to additional porosity of the system, allowing for faster gas diffusion and, in the case of actual 'faulting' within the sediment, gas communication with the lower regions of the sediment column – both yielding more gas uptake, hydration, and increased pressure drop. As it has been shown that highly porous sediments fundamentally trap more gas as it percolates through the column, as well as the likelihood of a less-than-optimal closest packing arrangement upon settling for larger (and naturally more porous) systems, such behavior may explain the faster uptake of gas in the Blake Ridge system. Note, however, despite the increased amount of gas absorbed/hydrated, the curve still follows the asymptotic decay to the "no observable change" condition as in the Gulf of Mexico system. Such an event took roughly 2 weeks to reach.

Figure 4.17 is the 1200 psi formation condition, although in this case the Gulf of Mexico system was tested at both 2 and 6°C. Note the similarity, as in the 900psi formation case, to that predicted by mass-transfer.

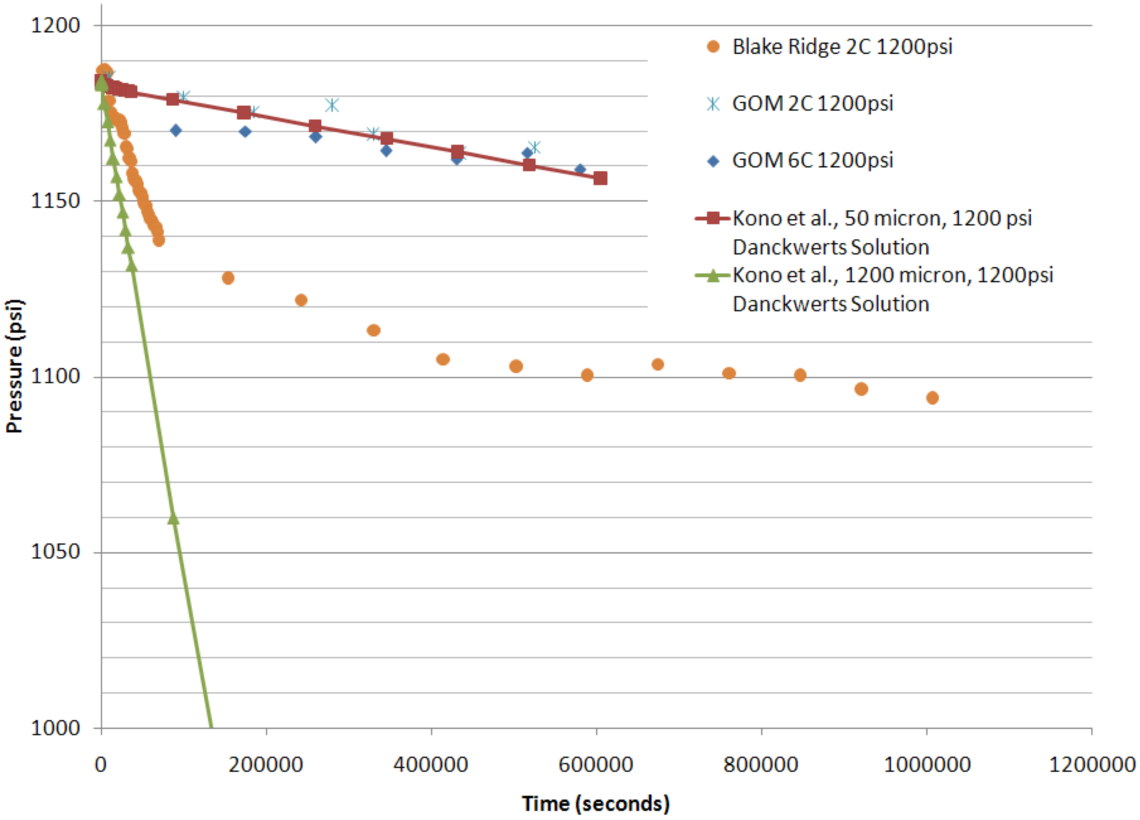

Figure 4.17 A comparison of pressure drop under 1200psi methane hydrate formation conditions for Gulf of Mexico and Blake Ridge host sediments to theoretical mass-transfer calculations

Again, the behavior depicted in figure 4.17 was similar to that observed with the 900 psi run in figure 4.16. However, in addition to hydrate formation runs in the Gulf of Mexico and Blake Ridge host sediments at 2°C, a run was also conducted in the Gulf of Mexico host sediment at 6°C and the corresponding pressure drop was monitored. As can be seen, both the 2^{o}C and 6^{o}C pressure drops in the non-porous system followed slightly below the Danckwerts solution (maximum deviation of -10psi after approximately 1 day of formation), and again all three systems asymptoted to a constant pressure condition, with the GOM system reaching the pseudo-equilibrium after approximately 1 week, and the BR system after 10 days. It is noteworthy that the mass-transfer limited solution begins to overtake the non-porous hydrate system at long time periods (i.e. the pressure drop predicted exceeds observed pressure drops). It could be reasoned that the diffusion coefficient at high time periods is more strongly influenced by the presence of hydrates than at early times – indeed, the diffusion coefficient of methane in gas hydrates is one to two orders of magnitude lower than that observed/predicted for methane in seawater ($2*10^{-12}$ m^2s^{-1}, Kvamme 2002), and because the mass transfer model currently in place does not support transient diffusion coefficients, the model may over predict pressure drop.

Also shown in figure 4.17 is the line of mass transfer predicted from Kono's work in 1200 micron glass beads. Such a system uses particles two orders of magnitude larger than the systems studied in this work, and consequently the overall observed kinetic rate constant (21.2×10^{-2} min^{-1}) increases pressure drop significantly (after $6x10^5$ seconds, pressure in such a system is predicted to be 641psi). However, it should be noted that the large particles used in Kono's work had pore water saturations (that is, the ratio of water volume to the volume of voids) of only 18%. Such low saturations imply a relatively large surface area to volume ratio in the pore spaces; that is, if a void is not completely filled with water, the remaining space must necessarily be gas/methane. In the case of hydrates, it has been shown repeatedly (Clarke and Bishnoi, 2001; Englezos et al., 1987; Kim et al., 1987 and Skovborg and Rasmussen, 1994) that larger surface area to volumes dramatically increase conversion and gas uptake. Consequently, the value for the kinetic rate constant obtained in their studies must be used with caution when applied to fully or almost fully-wetted sediments (i.e. those with a lower participating surface area to volume ratio).

Figure 4.18 shows hydrate formation plots for a set of six runs under various conditions: 3 with DI and 3 with salt water. Note that this set was conducted with the Gulf of Mexico sediments as the host

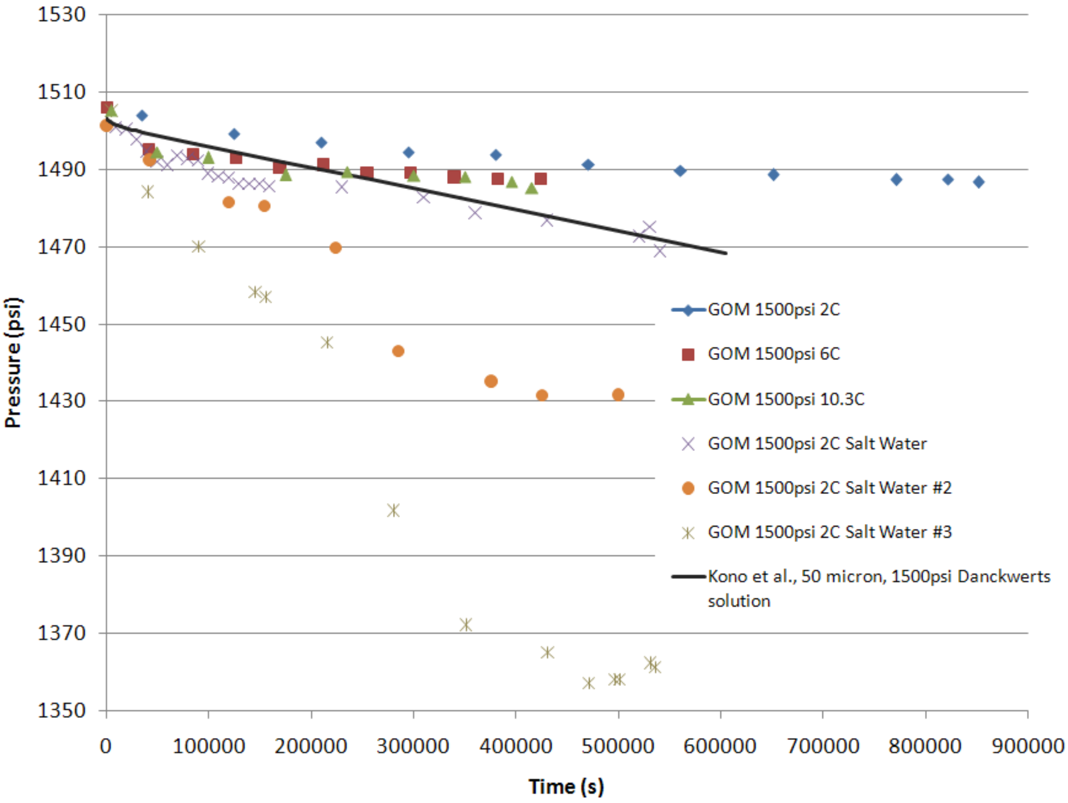

Figure 4.18 A comparison of pressure drop under 1500psi methane hydrate formation conditions in the for Gulf of Mexico host sediments using both DI and sea water to theoretical mass-transfer calculations

For hydrates formed in deionized water, the trend is similar to that observed in the 900 and 1200psi formation conditions. The hydrates formed at 6^{o} and 10^{o}C followed very similar trends (within experimental error), in that the growth rates were higher, initially, than both the 2°C and predicted mass-transfer models. Again, however, as time progressed, both asymptoted to a pressure higher than predicted by the Danckwerts' solution. Most notably was the behavior of the salt water system, in which gas uptakes at $t > 5 \times 10^5$ seconds were between 2 and 8 times that in the deionized water system, as determined by the pressure drop in the system. Also notable was the seemingly unpredictable amount of gas uptake under similar conditions (1500psi, 2°C +/- 0.1 °C) in the salt water system. The total pressure drop ranged from 30psi (predicted by the Danckwerts model) in #1, all the way to 140psi pressure drop in #3. It should be noted that between every run, the system was allowed to warm more than 12°C (often more than 15 °C), with the idea that thermal cycling might eliminate the any partially formed cages in solution, and eliminate any hysteresis effect. Although in the figure, the runs are labeled 1, 2, and 3 in salt water, they were not performed in that sequence (chronologically, the runs were performed 3 → 1 → 2). One might use a hysteresis effect, if it were present after warming 12 degrees, to explain the continued pressure drop in the system. However, because the runs were not performed in such an order, and because there was no noticeable loss of water in between runs, the variation in hydrate formation may simply be due to the stochastic nature of hydrate nucleation and formation, and the random nature by which paths and cracks are made in sediment by rising gas bubbles. Finally, and an effect that might be studied in future work, was the seemingly two-stage formation kinetics in salt water. In figure 4.18, it can be observed in salt water runs 2 and 3, that after approximately 200000 seconds the pressure drops at a much faster rate than $t<200000$. While further work is necessary, one may hypothesize that the k-value (kinetic rate constant) might theoretically change in such a closed system as the water is enriched in ions (hydrates exclude ions as they form). Due to the fact that salt serves to increase formation rate, one would expect the *rate* of pressure change to increase with time as more hydrates form – in essence, a runaway-type reaction up to the solubility limit of the salt or the thermodynamic limit due to inhibition at increased concentrations.

Although such results between salt runs are interesting, the increased rate and amount of consumption in the presence of such an inhibitor is well known in the study of hydrate inhibitors for flow assurance. Makogan and Holditch, 2001, observed such a phenomena both in the presence of thermodynamic inhibitors (alcohols, glycols, and electrolytes), and in kinetic inhibitors and concluded that while the presence of any inhibitor decreases the hydrate strength, it simultaneously "increases hydrate porosity, diffusive permeability, and rate of hydrate growth." This is in agreement with results presented thus far. First, sediment is a very complex system: it is unlike glass beads, washed playground sand, or porous ceramics in that it contains a multitude of salts/ions/impurities, many of which go into solution and may behave as inhibitors (save some larger, as yet fully explored biological products which are said to enhance hydrate formation). Additionally, rough sediment grains provide large areas for hydrate nucleation, unlike the pseudo-defect-free volume of deionized water in a simple hydrate reactor. The sediment gives gas a means to stay in contact with water longer and to increase the surface area involved in the reaction. Consequently, gas uptake, as shown in every single instance in these formation studies, was slightly-to-greatly enhanced in the presence of sediments, and not simply glass beads (as shown by applying a kinetic rate constant obtained from beads to model this system). Also, the application of even **more** salt (figure 4.18) to the system again followed trends suggested by Makogan – gas uptake was statistically significantly increased compared to such a system in deionized water. Exactly which of the salt-effected factors (porosity, diffusive permeability, or rate of growth) most strongly influenced pressure drop in the system is a study in its own right, although a brief sensitivity study of the Danckwerts model, below, may shed some light on the problem.

A numeric study was carried out to determine which of salt's proposed influences alters gas uptake most significantly. Values in the study were varied such that they maintained "reasonable" values, or values that fell within generally regarded errors on measurements. For example, porosity never went below 0 or above 1, kinetic rate parameters varied by 2 orders of magnitude on either side of literature values, and diffusion coefficients were varied by a factor of 40 to simulate possible excess solid or liquid contribution. It should be noted that because the hydrate diffusion coefficient in sediment is dependent on porosity and the diffusion coefficient in water, it was not varied directly; instead, sediment porosity (attempting to encompass the porosity of the hydrate) and the seawater diffusion coefficient were varied independently. Results are shown below in figure 4.19a, b, and c

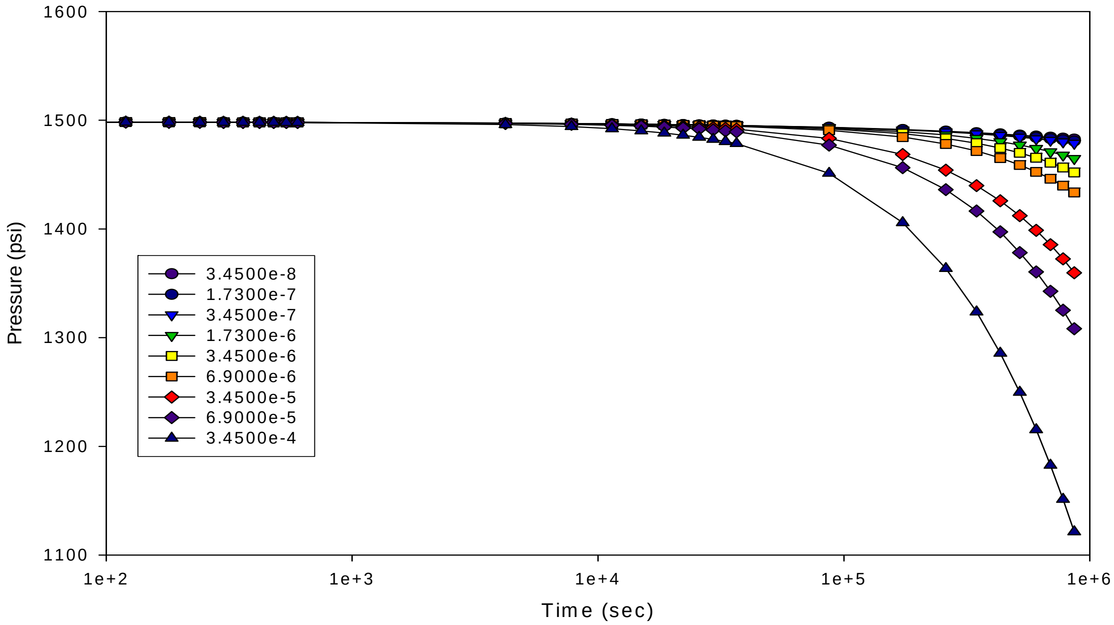

Figure 4.19a The effect of first order kinetic rate constant value (sec^{-1}) on methane uptake at 1500psi and 4°C in host sediment of 50 μm size.

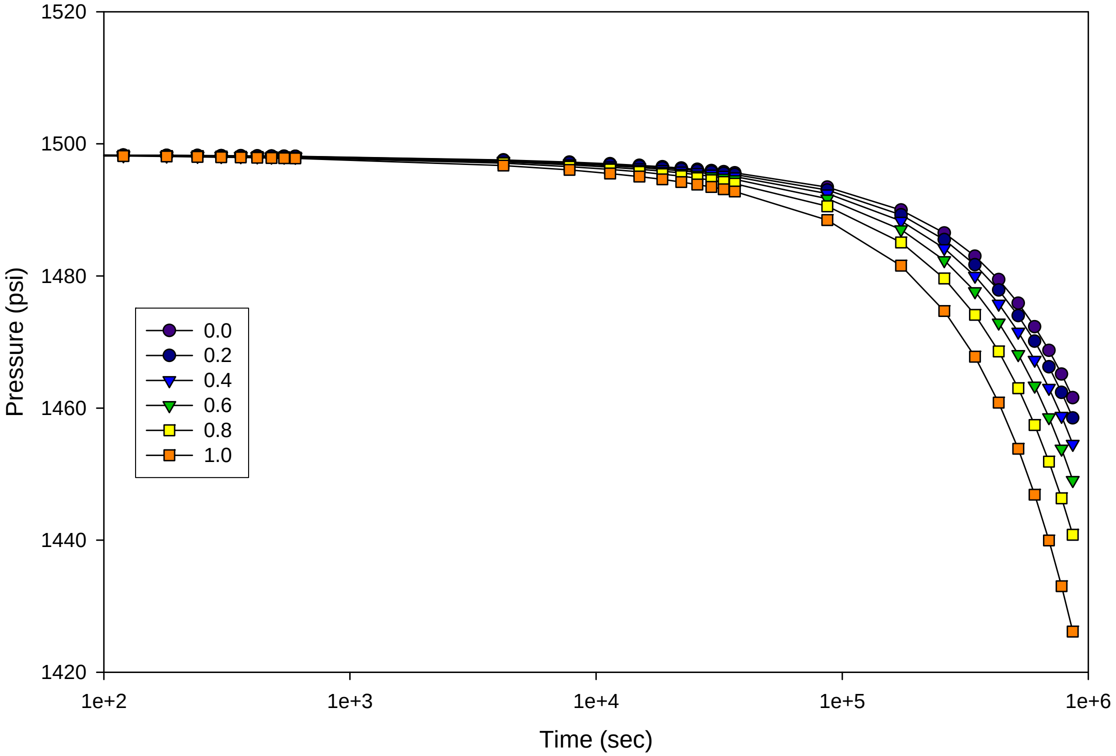

Figure 4.19b The effect of porosity on methane uptake at 1500psi and 4°C in the host sediment of 50 μm size

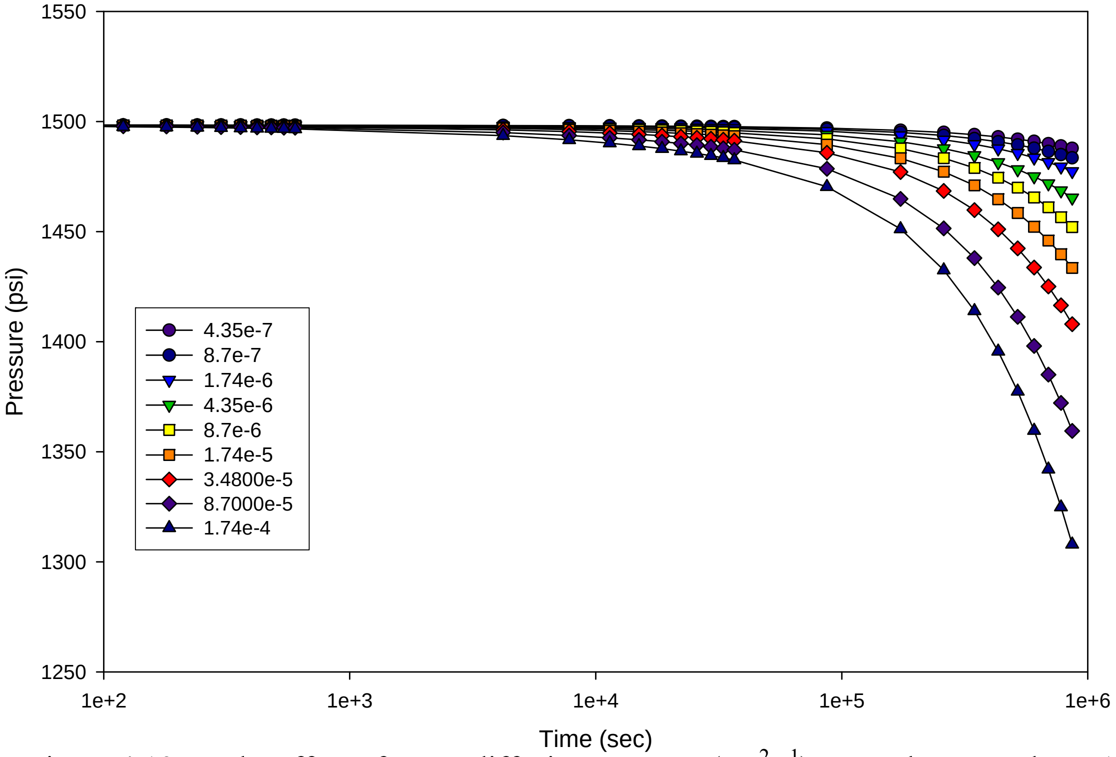

Figure 4.19c The effect of water diffusion constant (cm^2s^{-1}) on methane uptake at 1500psi and 4°C in a sediment of 50 μm size

It is apparent that, in order of increasing pressure reduction, the variables affected by salt follow the order: sediment porosity (altered by hydrate growth) < diffusion coefficient < kinetic rate constant. Unfortunately, current models for methane diffusion coefficients in porous sediments do not account for complete disruption of the sediment bed by growing hydrates, nor do they account for the altered overall diffusion character of the hydrate/sediment/water mix – that is, they assume the sediment bed is either water or sediment in varying amount in contact with each other. While salt may promote increased hydrate porosity, and by extension increased sediment bed porosity, the current sensitivity study does not account for gross morphological/structural changes in the sediment bed by hydrates. Further refinements are necessary in the model to incorporate these parameters. However, what is certain is that increasing salt concentrations alter the diffusion coefficient in water, one of the variables studied. Note that over an order of magnitude increase in the diffusion coefficient of methane in salt water (8.7×10^{-6} cm^2s^{-1} → 1.7×10^{-4} cm^2s^{-1}) must occur to explain the pressure drops observed in experiments (figure 4.18). This seems unlikely, as it has been shown (Himmelblau, 1964) that the diffusion coefficient of gases in water *decreases* with increasing salinity. One assumes, given the propensity of hydrates for excluding ions and enriching the surrounding medium, over long times, the diffusion coefficient of the medium would *decrease* not only due this fact but also due to the very presence of hydrates (having a diffusion coefficient closer to that of a solid, not a liquid). Given the aforementioned conclusions, it is reasonable to conclude that a major effect of salt on hydrate formation is on the rate of its formation; specifically, the kinetic rate constant. Note that a rate constant of 6.9×10^{-5} sec^{-1} would yield results similar to those observed in the highest gas consumption case (Gulf of Mexico, 1500psi, 2°C, #1), but this is over 3 orders of magnitude *faster* than that calculated for such a system (3.11×10^{-8} sec^{-1}), as the following analysis demonstrates. Note such a finding suggest one (or more) of the following:

- The mass-transfer model is too simple.

This is highly likely. Fissures, heterogeneities, and other physical complexities make collapsing the sediment/water system into a solid volume with homogeneous diffusion and reaction a likely factor in incorrect/exaggerated predictions. More likely, gas reacted more slowly than predicted, but simply had a larger surface area to react with due to the aforementioned non-idealities

- The reaction is not first order, as is used in the model

A higher-order model (rate=k P_{gas}^2, or rate=k P_{gas}^3) would tend to predict faster reactions for equivalent pressures. Or, conversely, a first order rate constant would need to be larger than reality in order to account for the same system. While this is an easy and tempting explanation, there have been simply too many models created using very pure systems (see Sloan, chapter 3) in which hydrate growth is easily modeled as a first-order system. While the possibility may exist that sediment alters the fundamental rate law for hydrate growth, it is small.

- Salt's other effects may cause a non-linear increase in hydrate growth

This, too, seems likely. While the sensitivity study used an "all-but-one" method for fixing variables, certainly reality reflects each of the variables working simultaneously. That is, not only does salt increase the rate constant, it increases bed porosity. The cumulative effect is greater than the sum of the parts, and as such, the sensitivity study, because it only varies one effect at a time, over-predicts the value necessary for the rate constant when varied alone.

In order to calculate "true" values of the rate constant from actual data, basic chemical kinetics was used. If one assumes a first order system, the following holds:

$$rate = -k \cdot C_{CH_4} \tag{4.11}$$

$$\frac{dC_{CH_4}}{dt} = -k \cdot C_{CH_4} \tag{4.12}$$

$$\frac{dC_{CH_4}}{C_{CH_4}} = -k \cdot dt \tag{4.13}$$

$$\int \frac{dC_{CH_4}}{C_{CH_4}} = \int -k \cdot dt \tag{4.14}$$

$$\ln(C_{CH_4}) = -kt + C \tag{4.15}$$

$$C_{CH_4} \propto P_{CH_4} \tag{4.16}$$

$$\ln(P_{CH_4}) = -kt + C \tag{4.17}$$

Plotting equation 4.17, the natural logarithm of system pressure versus time, one can fit first-order reaction data with a straight line whose slope is equal to the kinetic rate constant. Shown below in figure 4.20 is an example of such a plot based upon data from the formation experiments. A comprehensive list for each of the pressure experiments can be found in Appendix B. Table 4.4 is a summary of the rate constants for all experiments, fit to a first order system. It should be noted that Blake Ridge sediments did not obey a linear fit on a ln(P) vs. time graph for all times. Instead, it appears as though there are two distinct phases for reaction. At times below 7 x 10^4 seconds (approximately 19.5 hours), there is a rapid growth on par with experiments done in salt water (rate constants of 10^{-7} sec^{-1}), and a slower growth phase with rate constants close to Gulf of Mexico sediments at similar pressures and temperatures. Again, as explained earlier, such non-linearity is most likely *not* due to a different rate law. Instead, it seems most logical that defects in the sediment column (exposing a large surface area), as well as preexisting trapped gas in the porous system, caused a rapid decrease in pressure as hydrates were initially formed. Then, as gas converted to hydrates, diffusion into the sediment column was limited by the presence of a relatively impermeable solid (hydrates), thus resuming the mass-transfer-limited behavior observed in the more non-porous GOM system.

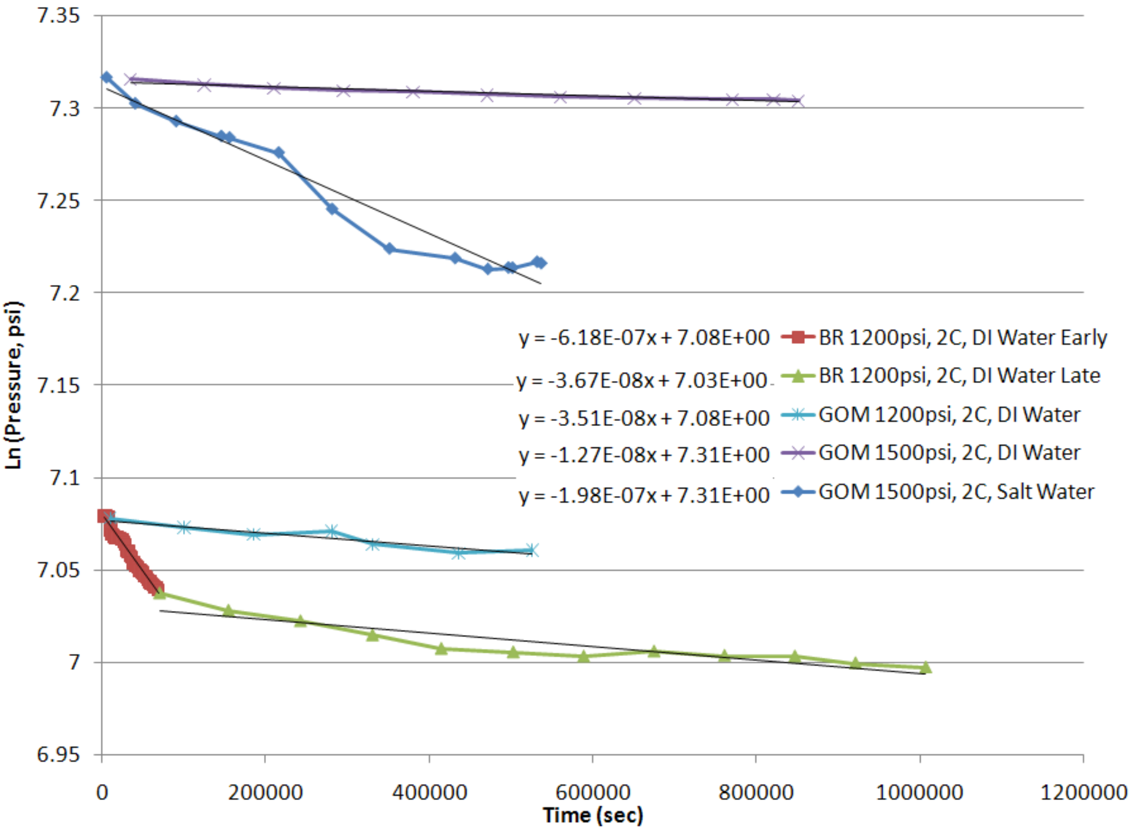

Figure 4.20 Ln (Pressure) vs. time curves for methane hydrate in Gulf of Mexico and Blake Ridge sediments under a variety of formation conditions (linear fits shown)

It can be seen that the fit is quite variable in figure 4.20. Misfits of the kinetic data are often due to the inclusion of data points at the end of each run, in which the pressure did not change appreciably. Notably, the GOM system at 1500psi and 2°C – removal of the last 4 data points (where the pressure fluctuated about the mean) makes the fit appreciably better (R^2 of 0.974 as opposed to R^2 of 0.957). However, all data are included in the interest of completeness. Removal of the last four points yields a kinetic rate constant 16.2% higher than indicated in figure 4.20 and table 4.4; this is typical of the "order of magnitude" kinetic rate constant calculations done in such a manner.

Table 4.4 Extracted first-order kinetic rate constants in GOM and BR sediments

Water	Sediment type	Temperature (°C)	Pressure (psi)	k (s^{-1})
DI	BR, early	2.00	900.00	7.47E-07
DI	BR, late	2.00	900.00	4.48E-08
DI	GOM	2.00	900.00	1.94E-08
DI	BR, early	2.00	1200.00	6.15E-07
DI	BR, late	2.00	1200.00	3.99E-08
DI	GOM	2.00	1200.00	3.51E-08
DI	GOM	6.00	1200.00	2.81E-08
DI	GOM	2.00	1500.00	1.27E-08
DI	GOM	6.00	1500.00	2.15E-08
DI	GOM	10.30	1500.00	5.95E-09
Seawater	GOM	2.00	1500.00	1.98E-07
Seawater	GOM	2.00	1500.00	9.80E-08
Seawater	GOM	2.00	1500.00	3.11E-08

For Blake Ridge sediments, which are most closely related to the system studied by Kono et al. 2002 (~50 μm mean sediment size), the kinetic rate constant was between 18 and 20% of the reported value. As stated, however, this could be due to the particle size distribution, and therefore hydrate/water surface area in either system. Kono used a system that was 50% 100 μm glass spheres and 50% 1 μm ceramic particles. Such a sharply bimodally distributed system, while mathematically yielding an average particle size close to that of the Blake Ridge system, should not be expected, pore-wise, to behave/hydrate as a more smoothly distributed particle-size system should. The 1 μm particles are expected to fill in the spaces between the larger particles, yielding larger surface area to volume ratios and enhanced rates of hydration. Additionally, as explained by Parent and Bishnoi (1996), Natarajan et al (1994), and Englezos et al. (1987), nucleation and kinetics can be masked by "a large driving force or system heterogeneities," and results are "often geometry dependent." The Gulf of Mexico sediments, when performed with deionized water, yielded results on the order of 1-2% of reported values. While the smaller particle size was expected to increase the rate of hydration due to the larger area of contact between pore-space gas and water, the confounding factor remains: how much gas was actually trapped in the sediment column. Here, the lowered gas holdup factor in fine sediments outweighs any gain from increased surface area (i.e. if there is no gas in the column to react, it doesn't matter how small the particles are or how large their internal surface area is). Qualitatively, however, results agree well with previous work in porous systems. Larger particle sizes yielded faster apparent kinetics. And, while early work in pure porous systems concluded that increased pressure (driving force) also increased apparent kinetics, such a trend was not observed in these experiments – perhaps such a trend was lost in experimental error.

While it is clear that a means for stabilizing the sediment column during hydrate formation is necessary to eliminate some of the aforementioned confounding factors, the issue then becomes: what part of the sediment column (i.e. the mudline or the subsurface) is the experiment simulating? Chapter 6 of this work will address potential enhancements to the FISH unit to allow for better understanding of hydrate growth in previously hydrate bearing sediments.

Chapter 5: Effect of Sediments on Hydrate Equilibrium and Dissociation Kinetics

Chapter four of this work addressed the question of *initial* hydrate behavior in sediments. The question of reaction rates, diffusion coefficients, and salt water effects were all studied in the creation of hydrates in two end-members of the previously-hydrate-bearing family of sediments. This chapter will attempt to answer questions regarding the *end* of the hydrate's life-cycle in sediment: does the sediment alter observed dissociation kinetics, and how does it affect thermodynamic equilibrium?

While the thermodynamics of a material may be studied effectively at any point in the material's history, thermodynamics of sediment/salt water hydrates (that is, temperature and pressure formation conditions) were studied at the end of the experiment rather than the beginning for two reasons. The first and most apparent reason is that the formation method used in the static charge mode does not lend itself to easily study the moment of hydrate growth. As discussed, the rapid charge of the system pressure to probable "supercooling" conditions (excess pressure is virtually equivalent to subcooling) gave a limited resolution to the conditions necessary for hydrate growth. That is to say, the pressure was increased above the probable equilibrium point (a necessary pressure for the given temperature) so quickly that we were unable to discern a marked uptake of gas due to hydration. The second reason for assessing thermodynamics after a considerable amount of formation time (1 to 2 weeks) was to address the possible metastability of the newly nucleating hydrates. There has been discussion (Rafailovich, Koga, personal communication June 4th 2006) about the possibility that, in a newly formed hydrate, certain polymorphs may occur until the system relaxes/equilibrates, leading to erroneous formation prediction. Indeed, atypical polymorphs of hydrates (that is, structures other than sI, sII, or sH) have been observed by Chakoumakos (personal communication, 2007) and others (Dyadin et al. 1999a, 1999b) at system conditions outside those normally found on earth (10^4- 10^5 atmospheres). Consequently, while it is unlikely that such "extreme hydrates" appear in this system, hydrates have been seen in metastable "common" structures upon initial formation (Staykova et al., 2002) at usual pressures and temperatures (100 atm, 4°C). Unfortunately, one can never be certain that the observed structure is not metastable – however, repeated experiments yielding results which do not deviate significantly from literature values add credibility to the assumption that hydrates were, in fact, of the common type. Furthermore, because the hydrates were formed from pure methane gas, and methane has not been observed to form any structure other than sI at pressures below 800×10^6 Pa and 15°C (Marshall et al., 1964), we have assumed, for the sake of argument, that all bulk hydrates observed were sI. Gas analyses, shown in chapter 2 (figure 2.9) indicate a lack of measureable hydrate-forming gases other than methane present in both the feed and off gases from dissociating hydrates. Thus impurities, if present (with the potential for sII formation), were far outweighed by the sI content in the system.

5.1 Kinetic Modeling

It is apparent from chapter 4 that there is a high degree of non-ideality in the system studied. Kinetic studies of formation revealed rates that were indicative of fractures, veins, and imperfections within the sediment system, instead of formation from pure diffusion through a solid volume. Additionally, gas holdup studies have shown that no matter what the rate of gas flux through the system, gas will be held up by the sediment column (yielding a more homogeneous distribution of hydrates). Such complexities surely hinder studies regarding formation kinetics, but (as will be clear in the remaining sections) they pose enormous difficulties in studying the kinetics of dissociation and thermal modeling of the system while dissociation occurs. As such, results presented herein should be assessed primarily from a qualitative point of view, with the models serving as a means to acquire order-of-magnitude approximations, and not definitive values for certain properties.

5.1.1 The Question of Heterogeneity

The most challenging aspect of understanding hydrate behavior upon dissociation is determining how the hydrates were distributed within the sediment column on formation. As shown in the left animation in figure 5.1, one would expect from pure diffusion that hydrates should form extremely heterogeneously within the sediment, with the bulk (highest concentration) of hydrate occurring at or directly below the sediment/gas interface, with a rapid decrease in the amount of hydrate as depth increases (see Danckwerts' solution, chapter 4). However, under the low flow dynamic charge condition, it was observed that hydrates formed throughout the column (e.g. the massive hydrate in the Blake Ridge sediment) due to gas holdup as shown in the right animation of figure 5.1. Although under static formation conditions such uniformity is not to be expected, there is a certain gas holdup that allows hydrates to form in quantities greater than simple diffusion would allow, seen in the middle of figure 5.1.

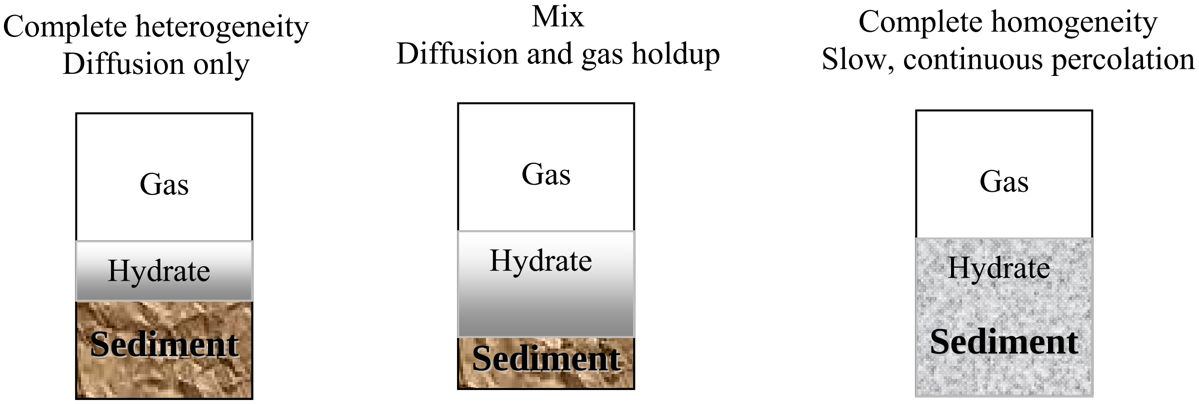

Figure 5.1 Different formation models in the sediment column

Understanding such a distribution is essential to dissociation kinetics because as the hydrates dissociate, they absorb energy (heat of dissociation=5.42 x 10^4 J/mol, Handa and Stupin 1992). As will be shown later, the rate at which the temperature of the sediment/water/gas/hydrate column changes can then be used to back-calculate the rate at which the hydrates dissociated. Unfortunately, because the temperature at every point within the column can not be measured, certain approximations must be made when modeling the system. For the current system, one thermocouple which measured the centerline temperature (both horizontally and vertically) was inserted into the sediment column, and it was assumed that via symmetry, temperatures in the surroundings could be approximated. However, the conundrum in using one thermocouple comes when one tries to relate the rate of temperature change to hydrate dissociation: was the temperature change in the system due to hydrates directly adjacent to the tip of the thermocouple (as in the rightmost case of figure 5.1), or was the rate of change based upon a cooling effect from hydrates dissociating far away (as would be expected in the leftmost case of figure 5.1). The problem can be restated as: was the rate of change in temperature near the thermocouple faster than would be allowed if hydrates *were not* surrounding it? That is, if hydrates formed at or very near the thermocouple, the temperature change upon dissociation should be essentially instantaneous. However, if hydrates formed solely at the top of the column and a “cold front” from dissociating hydrates was forced to propagate through several centimeters of a sediment/water matrix, the rate of change would be much more gradual and slower in onset. To answer this question, a simple heat transfer analysis (using liberal approximations regarding system properties) can be done.

The first step is to define the problem. In this simple case, heat propagation through the sediment was treated as a one-dimensional transient heat transfer problem. Note that while simple, this analysis provides the **maximum** rate of change at the thermocouple’s tip – incorporating two- or three-dimensional effects merely slows down the rate of heat propagation, as the walls of the cell (maintained at a constant temperature) would serve to *slow* the cooling of the thermocouple. The problem can be defined by the familiar one-dimensional heat equation:

$$k\frac{\partial^2 T}{\partial x^2} = c_p \rho \frac{\partial T}{\partial t} \tag{5.1}$$

$$\alpha = \frac{k}{c_p \rho} \tag{5.2}$$

where k, c_p, and ρ are the thermal conductivity, heat capacity, and density of the sediment/water/gas/hydrate mixture (typical values discussed on page 108 of this work). The variable α is introduced for convenience, and is referred to as the thermal diffusivity of the system. Without going into further detail, the above partial differential equation may be non-dimensionalized and solved easily using separation of variables, yielding:

$$\frac{T(x,t)-T_{surface}}{T_{initial}-T_{surface}}=erf\left(\frac{x}{2\sqrt{\alpha t}}\right) \tag{5.3}$$

where T is the temperature, x is the depth in the sediment column (gas/sediment interface=0), and t is the time in seconds. The subscripts indicate the position within the column: *surface* is the temperature at the interface, *initial* is the initial sediment temperature for all points in the column, and *(x,t)* represents the temperature at any spatial or temporal point. It should be noted that this problem was solved using a fixed boundary condition: a constant interface temperature to simulate dissociating hydrates. Although this is unrealistic (dissociating hydrates eventually begin to warm), it provides the maximum "worst case" scenario for calculating temperature change in the column, and as will be shown, needs to be unrealistically low to yield results similar to observed temperature changes in the column. The rate of change at any point in the column may be obtained by differentiation of equation 5.3 with respect to time:

$$\frac{\partial T(x,t)}{\partial t}=\frac{-\alpha e^{-\frac{x^2}{4\alpha t}}(T_{initial}-T_{surface})\cdot x}{2\sqrt{\pi}(\alpha t)^{3/2}} \tag{5.4}$$

Thus, the rate of temperature change at the thermocouple (x=0.05) may be calculated and compared to observed temperature profiles. Figure 5.2 represents a temperature trace vs. time from a dissociation experiment. As can be seen, at early times (t < 30s) the temperature at the centerline decreased rapidly. This is, as expected, due to hydrate dissociation. At longer times, the system gradually warmed back to the initial (wall) temperature as the rate of cooling due to hydrate dissociation was outpaced by the rate of heating.

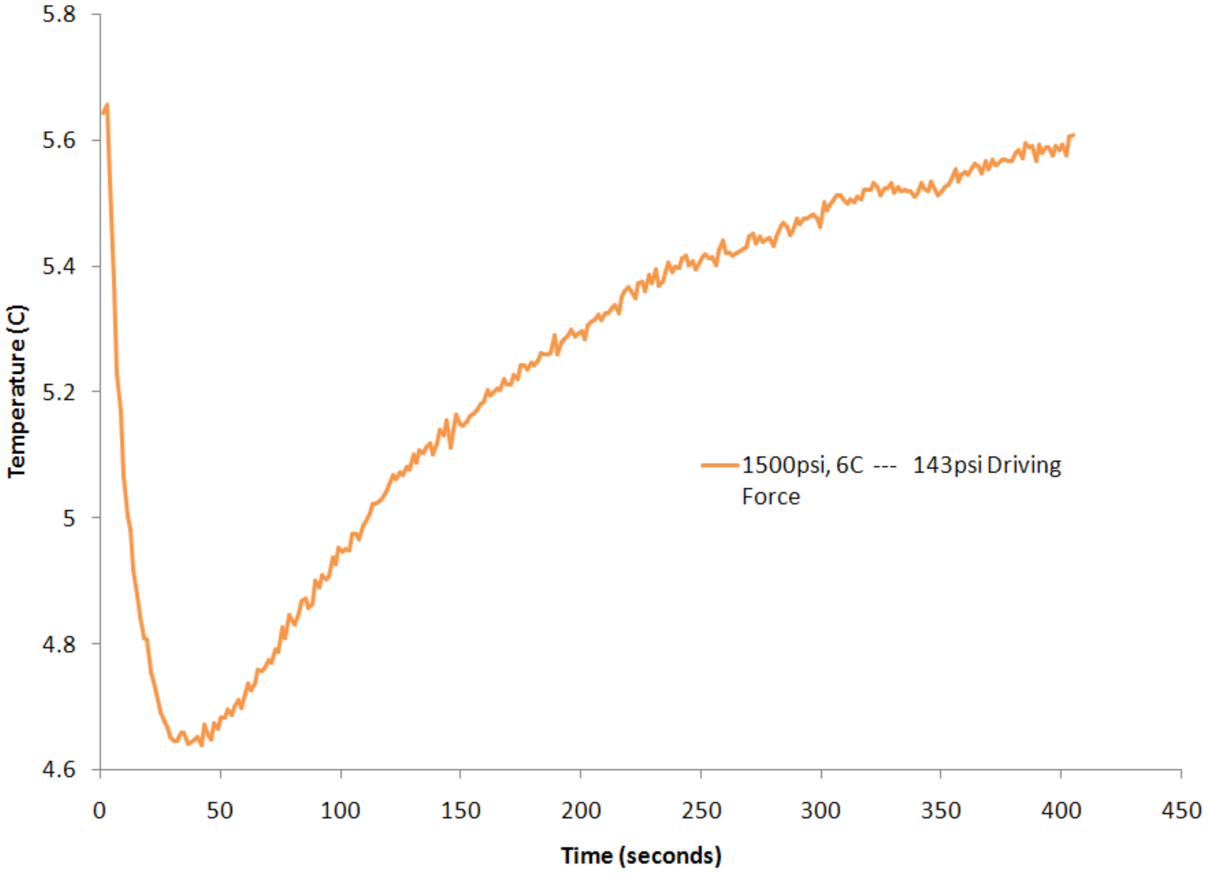

Figure 5.2 Temperature vs. time during dissociation of hydrates in the Gulf of Mexico host sediments at 6^{o}C, 1500psi formation, and 143psi of driving force

Early on (0 < t < 35), as can be seen, the rate of temperature change is nearly -0.03 K/s. It should also be pointed out that the temperature began decreasing almost immediately. One would suspect if hydrates were not present in very close proximity to the thermocouple, the temperature would remain constant until the cooling effect of the dissociation front propagated to thermocouple depth. Indeed, as shown in figure 5.3, the theoretical temperature change in the column would not be observed at the thermocouple until at least

10 seconds after hydrate dissociation (assuming the hydrate was merely 3cm from the thermocouple) and almost 30 seconds assuming the hydrate mass was 5cm from the thermocouple.

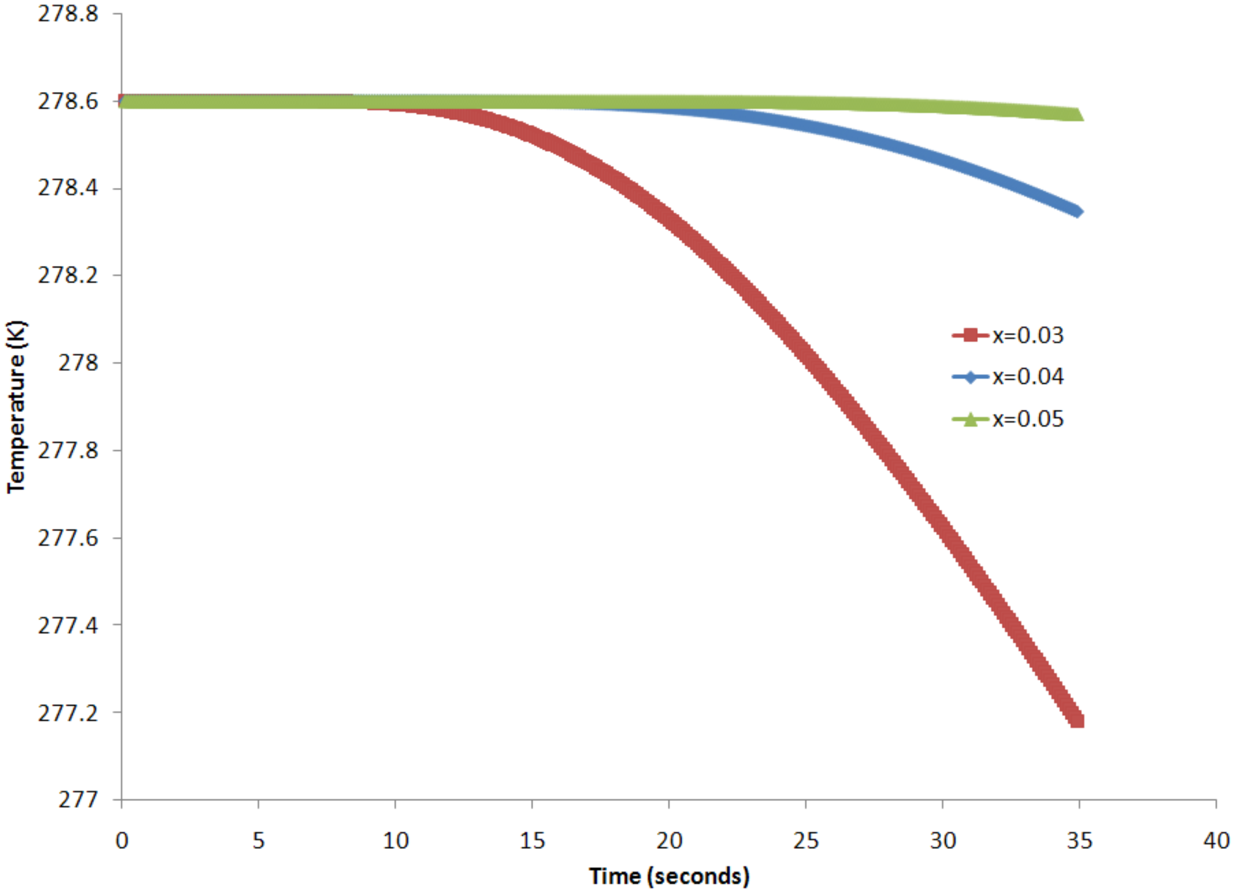

Figure 5.3 Theoretical column temperature as a function of depth (in meters) and time

It should be noted that physical values for thermal conductivity (k=3.145 W.m^{-1}.K^{-1}) and specific heat (c_p=940 J.kg^{-1}.K^{-1}) of the sediment/water/gas/hydrate mixture were taken from Moridis et al., 2005. The value of density was lowered from the reported 1842 kg.m^3 to a value of 1000 kg.m^3 to more closely approximate the more highly porous structure of the simulated matrix. Note that this actually **increases** the value of the thermal diffusivity (the rate at which heat propagates through the medium) and therefore would yield an overestimation of the rate of cooling. It should also be noted that the simulated surface temperature (the hydrate dissociation temperature) was held at **-20°C**. This is, almost certainly, too much cooling to be produced by the small amount of dissociating hydrate trapped within the column. Additionally, sustaining such a temperature depression for 30 seconds in the presence of warmer surroundings (the bath) is improbable. However, the temperature was chosen because it is the temperature necessary to achieve a cooling rate of -0.03 K/s (observed in figure 5.2) at 4cm below the base of the dissociating hydrate (a reasonable value, in light of the calculated penetration depth for diffusion in figure 4.13). The cooling rates versus time at given depths are shown below in figure 5.4

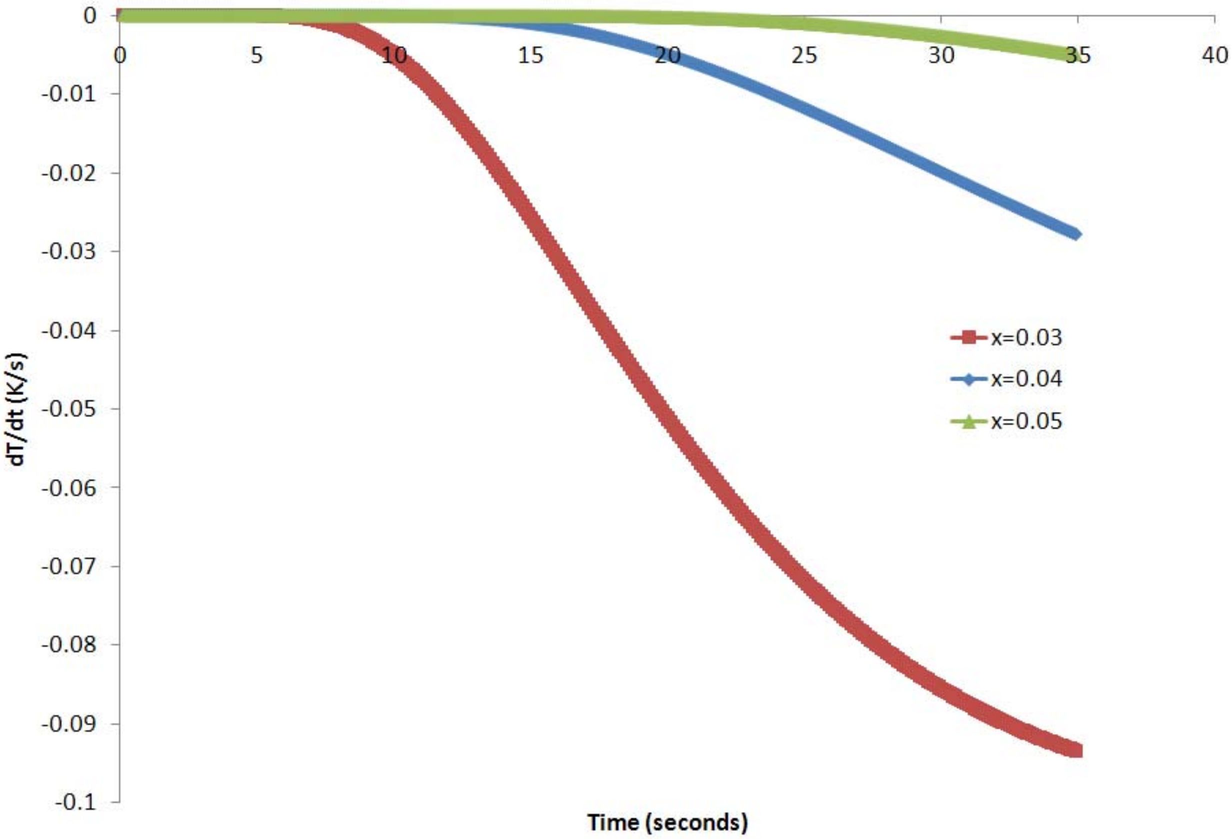

Figure 5.4 Cooling rates in the simulated system as a function of depth and time

In light of the best possible outcomes for hydrate dissociation in a purely heterogeneous sediment column (i.e. all the hydrate is at the top), it is reasonable to assume that, given the rapid onset of temperature change at a depth of 5cm, perhaps the hydrate is more homogeneously distributed. Such an assumption will be made in all remaining calculations. While perfect homogeneity is not expected – to wit, it is just as unlikely as perfect heterogeneity; some hydrate distribution throughout the whole column is far more likely than none at all.

5.1.2 Thermal Modeling

To best simulate dissociating hydrates within the sediment matrix, a three-dimensional heat transfer model using time and spatially-dependant variables should be used. However, because modeling the system was not the primary focus of this work and because many researchers have begun to construct very thorough models of hydrates in porous media (i.e. ToughFX, Moridis, 2002), a more simplified approach was taken. The idea in doing so was that previous work has *not* been done in once hydrate-bearing sediments, and values obtained from the simplified model may be compared to those values obtained in more complex models using less complex sediments (pure sands, glass beads, etc).

The first assumption made in modeling the system was that, as discussed earlier, hydrates formed homogeneously throughout the sediment. Additionally, the system is considered to be isotropic, such that thermal conductivities did not vary with spatial position (or, as explained later, time). These simplifications yield:

$$k\left(\frac{\partial^2 T}{\partial x^2}+\frac{\partial^2 T}{\partial x^2}\right)+\dot{G}(t)=c_p\rho\frac{\partial T}{\partial t} \tag{5.5}$$

where G(t) is the uniformly distributed but transient heat “generation” term due to hydrate dissociation. Of course, in a melting hydrate, this value will be negative (dissociation is endothermic). It should be noted that the treatment of the system will only be in two dimensions, as the third dimension (depth) is assumed to obey a symmetry condition (i.e. the temperature profile does not change with depth) provided by the spatial uniformity of the heat generation and thermal properties of the hydrate/sediment mix. The system, however, is rectangular, and thus must be solved in two dimensions. Finally, the boundary conditions for the system are as follows:

$$\begin{aligned}
&width = a\\
&length = b\\
&T(x,y,0) = T_{bath}\\
&T(0,y,t) = T_{bath}\\
&T(a,y,t) = T_{bath}\\
&T(x,0,t) = T_{bath}\\
&T(x,b,t) = T_{bath}
\end{aligned} \tag{5.6}$$

These boundary conditions simply state that in the beginning of the experiment, the system was at a constant temperature (bath temperature). Additionally, for all times after t=0, the walls of the system were considered to be isothermal (again, the temperature of the bath). These approximations allow for ease of solution.

As presented, a numerical approximation to equation 5.5 may be obtained using finite element analysis. Due to its ease of use, low cost, and availability, the spreadsheet program Microsoft Excel was employed to perform such an analysis. A simplification of the method, as detailed by Eid, 1987, Baughn et al., 1992, and Wetson, 1988 is presented here for explanation. The interested reader is encouraged to explore these works for a more thorough and generic explanation of the method

The fundamental assumption in finite difference analysis is that a system (or, more precisely, the equation describing a system) may be broken into discrete elements, "nodes," which approximate the continuum of points described by an equation. Considering equation 5.5, the resulting equation must be discretized both spatially and temporally with respect to temperature. In the case of the system studied, such a 2-D discretization at a given time might look like:

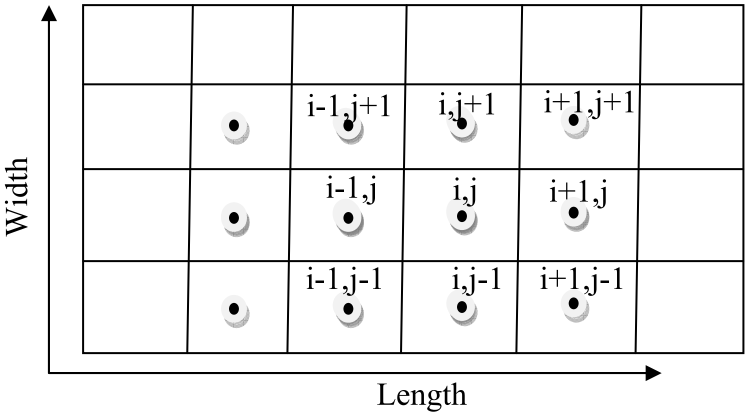

Figure 5.5 Nodal representation of a 2-D discretization

Where i and j are node positions, (i+1,j) is a node to the right, (i,j+1) is a node above, (i+1,j+1) is a node above and right, etc. Each node also has a time, t, associated with it, such that t+1 is one time step in the future, and t-1 is one time step in the past. Note that such terms as "above," "right," and "in the future" convey no magnitude – indeed, depending on the geometry and dynamics of the system, such terms may be nanometers to meters, or seconds to years.

To discretize equation 5.5 in terms of nodes, it helps to non-dimensionalize both the equation and boundary conditions. The result of such becomes:

$$\frac{\partial^2\theta}{\partial X^2}+\frac{a^2}{b^2}\frac{\partial^2\theta}{\partial Y^2}+Q=\frac{\partial\theta}{\partial\tau} \qquad \begin{aligned}&\theta(X,Y,0)=1\\&\theta(0,Y,\tau)=1\\&\theta(a,Y,\tau)=1\\&\theta(X,0,\tau)=1\\&\theta(X,b,\tau)=1\end{aligned} \tag{5.7}$$

$where$

$$X=\frac{x}{a}$$

$$Y=\frac{y}{b}$$

$$\theta=\frac{T}{T_{initial}}$$

$$Q=\frac{a^2G(t)}{kT_{bath}}$$

$$\tau=\frac{\alpha t}{a^2}$$

Equation 5.7 may be discretized using an explicit method, which calculates the current node's temperatures based solely upon temperatures in the previous time step (t-1), or using the more computationally-intensive implicit method, which calculates the current temperature based upon the node's temperature in the previous time step, T(i,j,t-1), and an "average" of temperatures of the 4 surrounding nodes at the current time step – an iterative process. However, because the implicit method is inherently stable, it was used. The interested reader is directed to Fundamentals of Heat and Mass Transfer, 4th Edition, by Incropera and DeWitt, for a discussion on stability. The implicit discretization of equation 5.7, yields equation 5.8:

$$\frac{\theta_{i,j}^{k+1}-\theta_{i,j}^{k}}{\Delta\tau}=\frac{\theta_{i+1,j}^{k+1}-2\theta_{i,j}^{k+1}+\theta_{i-1,j}^{k+1}}{\Delta X^2}+\frac{a^2}{b^2}\frac{\theta_{i,j+1}^{k+1}-2\theta_{i,j}^{k+1}+\theta_{i,j-1}^{k+1}}{\Delta Y^2}+G \tag{5.8}$$

Assuming ΔX=ΔY for the sake of display simplicity, yields equation 5.9:

$$\theta_{i,j}^{k+1} = \left(\frac{1}{2 + 2\frac{a^2}{b^2} + \frac{\Delta X^2}{\Delta \tau}} \right) \left(\theta_{i+1,j}^{k+1} + \theta_{i-1,j}^{k+1} + \frac{a^2}{b^2} \left(\theta_{i,j+1}^{k+1} + \theta_{i,j-1}^{k+1} \right) + \frac{\Delta X^2}{\Delta \tau} + \theta_{i,j}^{k} + G \Delta X^2 \right) \quad (5.9)$$

Thus, the dimensionless temperature at any time step may be found using the above equation. Of course, because the width and length of the cell were different, equation 5.8 was solved assuming different ΔX and ΔY. It should be noted that the solution is iterative – that is, solutions must not only be "marched" in time, in order to find the current time step's temperatures, but also solved iteratively due to the interdependence of every node's temperature on the 4 surrounding nodes. Because the nature of solution is recursive, certain stopping criteria must be in place in order to prevent spending an infinite amount of time calculating one time step. In the case of all the simulations described herein, Microsoft Excel was instructed do discontinue calculation if either: a) the change between successive calculations on a given node was less than 0.000001, representing a change of approximately 3×10^{-4} K or b) 1000 iterations were performed, whichever condition arose first.

Equation 5.8 is a relatively easy task for a spreadsheet to solve, and by examining the behavior of the temperature profile generated using different physical constants (thermal conductivity, density, and heat capacity), one may use the model to approximate those profiles obtained in actual experiments (shown in figure 5.2). However, the difficulty arises in determining the "homogeneous heat generation" term. The total amount of hydrate present in the sediment changes with time as the hydrate dissociates. Therefore, while the generated from node-to-node may be constant at a given time step, it varies temporally. Such a factor is directly related to the kinetic rate of dissociation of the hydrate, and is discussed in section 5.1.3

5.1.3 Kinetics of Decomposition and the Generation Term

There are several decomposition models for hydrate dissociation. However, this work will use the model proposed by Kim et al. (1987), in which hydrate decomposition is analyzed by treating the hydrates as (in this case) spherical particles. The equation describing the change in moles of a hydrate with time, as reported by Kim et al.,1987 is:

$$-\frac{dn_H}{dt} = \frac{7.44 \cdot 10^{11}}{\Psi \rho_H D_0} e^{\frac{-E_a}{RT}} (f_{eq} - f) n_0^{\frac{1}{3}} n_H^{\frac{2}{3}} \tag{5.10}$$

Where n_H is the number of moles of methane hydrated at a given time, n_0 is the initial number of moles of methane in the hydrate, E_a is the activation energy per mole of methane gas (the quantity, Ea/R is reported as 9400K), D_o is the diameter of the hydrate particle (to be discussed), f_{eq} is the equilibrium fugacity of methane in the hydrate phase, f is the fugacity of the methane in the gas phase, ρ_H is the superficial density of hydrate (defined as moles of methane/m^3 of hydrate; taken to be 7900 for fully occupied hydrates), and Ψ is particle sphericity, taken to be 1. Note that the value of 7.44×10^{11} (mol. m^{-2}. MPa^{-1}. s^{-1}) is the intrinsic kinetic rate of dissociation; one of the physical values this work will extract from the dissociation experiments. As shown, the rate of hydrate dissociation depends on essentially two important factors: the total hydrate surface area and the driving force between the equilibrium pressure of a hydrate and the system pressure. As demonstrated by Kim et al., the surface area of the dissociating hydrate is a summation of the surface area of all hydrate particles (the number of which does not change as dissociation proceeds). For the sake of simplicity, the average starting diameter of a hydrate particle in this work was assumed to be equal to the average particle size of the sediment that contained it. That is, there was assumed to be a one-to-one correspondence of particle-to-void size, with the influence of porosity only affecting variables such as thermal conductivity, density, and specific heat, rather than average hydrate particle size. A more thorough treatment of the kinetics of hydrate dissociation in variable-sized hydrate particles has been performed by Clarke and Bishnoi (2001). The main complication of equation 5.10, and one of the deciding factors of dissociation rate, is the difference in between the equilibrium fugacity (taken to be the equilibrium pressure at a given temperature) for a dissociating hydrate and the system fugacity (taken to be the system pressure). As mentioned previously in this work, there is an exponential dependence of hydrate equilibrium pressure on system temperature (figure 4.15). Because, as hydrates dissociate, they absorb energy from and reduce the temperature of their surroundings, the equilibrium fugacity (and consequently, the rate of dissociation) depends strongly on temperature. To simplify the analysis, a non-linear regression was performed to determine the best-fit equation of pressure (psi) to temperature (C) for a methane hydrate. Equation 5.11 represents a polynomial fit to data extracted from CSMGEM (Ballard, 2002)

$$\mathrm{Pr}\,essure = \frac{a \cdot (T^2 + bT)}{T^2 + cT + d} + e \tag{5.11}$$

where

$a = 2.283 \cdot 10^3$

$b = 8.141 \cdot 10^1$

$c = -1.987 \cdot 10^2$

$d = 4.989 \cdot 10^3$

$e = 3.768 \cdot 10^2$

The generation term may be found by first approximating equation 5.10 as:

$$\frac{dn_H}{dt} \approx \frac{\Delta n_H}{\Delta t} \tag{5.12}$$

and then using the heat of dissociation per mole of methane in the hydrate and the total volume of sediment:

$$Gen\left(\frac{W}{m^3}\right) = \frac{\frac{\Delta n_H}{\Delta t}\left(\frac{mol}{s}\right)\cdot \Delta H\left(\frac{J}{mol}\right)}{V_{sediment}(m^3)} \tag{5.13}$$

From equation 5.13, the assumption of homogeneous formation can finally be utilized. The heat generated (a negative value) by the dissociating hydrates is applied over the entire sediment volume. Additionally, the heat of dissociation is held constant. Some works (Handa and Stupin, 1992) have demonstrated that the heat of dissociation of hydrates is affected by pore diameters (and, consequently, hydrate size). However this work involves unconsolidated growth of hydrates with an excess of inter-particle non-pore (bulk) water, and thus the incentive for hydrates to form exclusively within the pore space in the absence of a confining pressure is assumed negligible. In the interest of completeness, however, the sensitivity of the dissociating temperature profile will be explored with respect to the heat of dissociation.

Combining equation 5.10, 5.11, and 5.13, the generation term in equation 5.8 becomes:

$$Gen = \frac{\left[\frac{k^{dissociation}}{\Psi \rho_H D_0}\right] e^{\frac{-E_a}{R\theta_{i,j}^{k+1}}} \left(\frac{a\cdot((\theta_{i,j}^{k+1})^2 + b(\theta_{i,j}^{k+1}))}{(\theta_{i,j}^{k+1})^2 + c(\theta_{i,j}^{k+1}) + d} + e - P^{sys}\right) n_0^{\frac{1}{3}} n_H^{\frac{2}{3}} \cdot \Delta H^{diss}}{V_{sediment}} \tag{5.14}$$

It should be noted that the temperature terms throughout equation 5.14 are time-dependent, and thus equilibrium pressures necessarily had to be recalculated at each time step, which was chosen experimentally. The reason for this is due to the approximation of derivatives (as in equation 5.12) as discrete steps, and the subsequent recalculation of temperature at each step. For example, in a time step process where Δt is large (say 10 seconds), essentially all the hydrate in the sediment may be predicted to dissociate from time step 0 to time step 1.

Given the huge amount of energy absorbed by such an event, the temperature in the system may be predicted to drop substantially. This, in turn, causes the recalculated equilibrium pressure to fall precipitously. However, as shown in equation 5.10, if the equilibrium pressure falls *below* the system pressure, hydrates will be *begin to reform* (as predicted by a positive-valued dn/dt). As the rate of dissociation is proportional to the amount of hydrates present, the system will again begin to dissociate, resulting in oscillatory behavior. This type of behavior is both unstable mathematically and unrealistic, and therefore a smaller time step must be chosen. Of course, one may choose an infinitesimally small value for Δt, although the tradeoff in precision comes at the expense of time – simulations of tens and hundreds of seconds were carried out, and thus a time step of 10^{-6} or 10^{-7}, while applicable, would be unnecessarily precise. Typical values of the time step which captured the behaviors of the model well were between 10^{-3} and 10^{-2} seconds, depending on the simulated values (higher dissociation rates necessitated finer time resolution).

5.1.4 Modeling Results

The simulations were performed using a 400-node grid with 20 x 20 equally spaced nodes over the length and width of the cell, giving a spatial resolution on each node of 1.67 x 0.789 mm. As noted, the simulations used a homogeneous distribution of hydrates, an isothermal condition at the wall, and also assumed a step-change in the pressure (initiating hydrate dissociation) down to system pressure. That is, the simulated pressure of the system was lowered instantaneously to the desired system pressure, which was held below the hydrate equilibrium pressure. While this poses no simulation-related issues, it was somewhat different than the actual behavior of the experimental system, where the pressure was decreased 200psi gradually (20psi per second) to prevent explosive decompression of the sediment matrix and wear on the equipment. The discrepancy this caused will be discussed later.

In order to determine the most influential factors of the sediment/dissociating hydrate on the numerical model, a sensitivity analyses was performed on all possible parameters of the model. It is worth noting that, ideally, the simulation should be sufficiently developed such that initial parameters (obtained from literature), can be used without modification. However, as the sediments used, the geometry of the system, the hydrate formation methods, and the simplicity of the model are all different from those in literature, slight variations are to be expected. Therefore, the effects of physically reasonable perturbations in values were studied. Figures 5.5 through 5.13 show the results of such analysis. Unless noted or varied, the following parameters were used, based upon experimental conditions:

- 2 μm particle diameter
- 2000 mL gas hydrated
- 150 psi initial pressure drop
- 5.6°C wall temperature
- 5.26×10^{-5} m^3 sediment/water volume
- 7900 mol $CH_4.m^{-3}$ hydrate (100% occupancy)
- 0.85 W. $m^{-1}.K^{-1}$ thermal conductivity
- 3000 $J.g^{-1}.K^{-1}$ specific heat
- 1000 $kg.m^{-3}$ density
- 1.24×10^{11} (mol. m^{-2}. MPa^{-1}. s^{-1}) kinetic rate constant (Kim et al., 1987)
- E/R = 9400 (Kim et al., 1987)

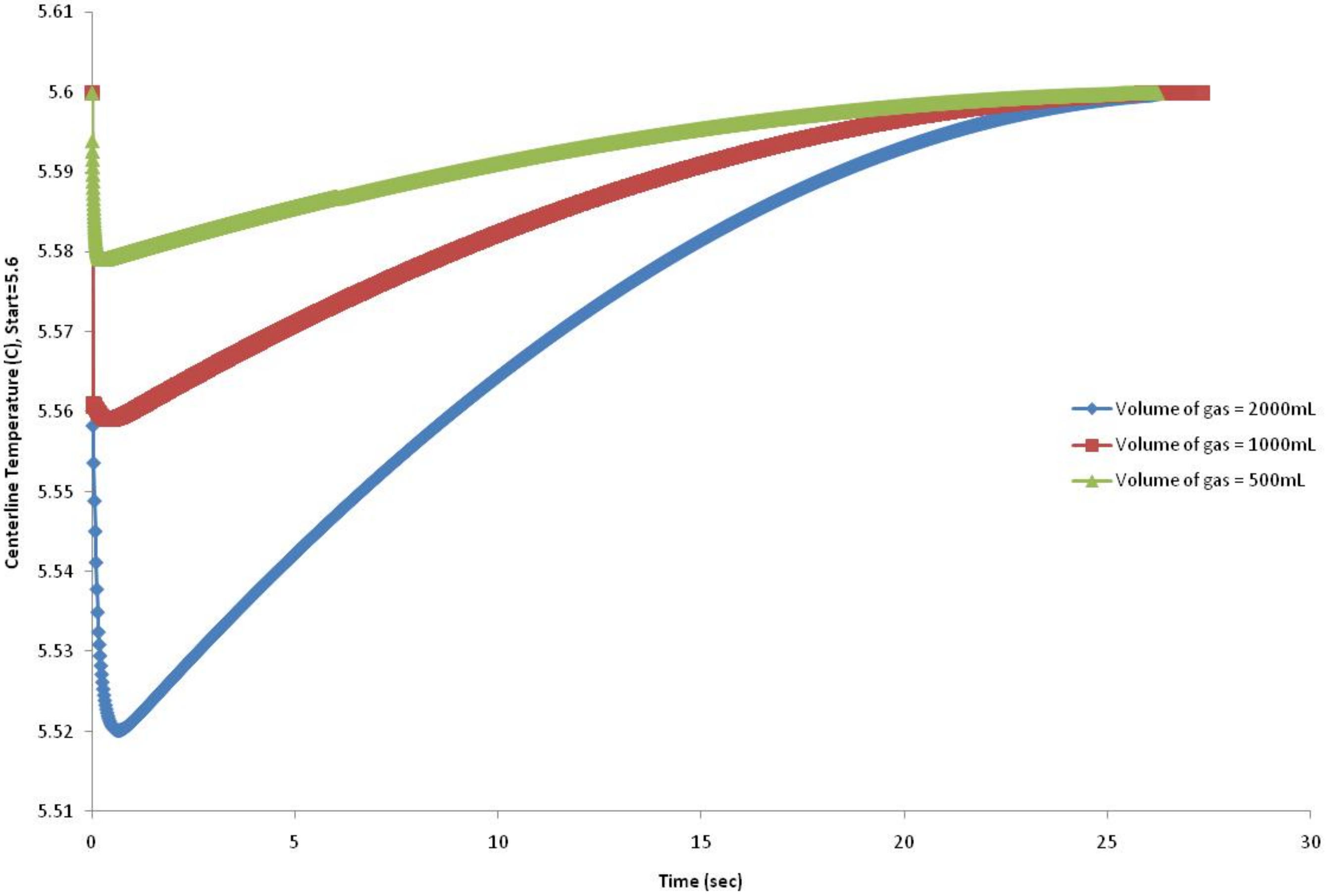

Figure 5.5 Theoretical centerline temperature with respect to time and hydrated gas.

From figure 5.5 it can be seen that a four-fold increase in the amount of enclathrated gas yields a maximal drop in sediment/hydrate temperature of slightly more than 0.08K. This agrees with the fact that a larger volume of enclathrated gas results in increased number of gas hydrate particles, thereby increasing the total surface area available during decomposition. It is interesting to note that the *duration* of the dissociation is affected very little (hydrates completely disappear at around 27 seconds).

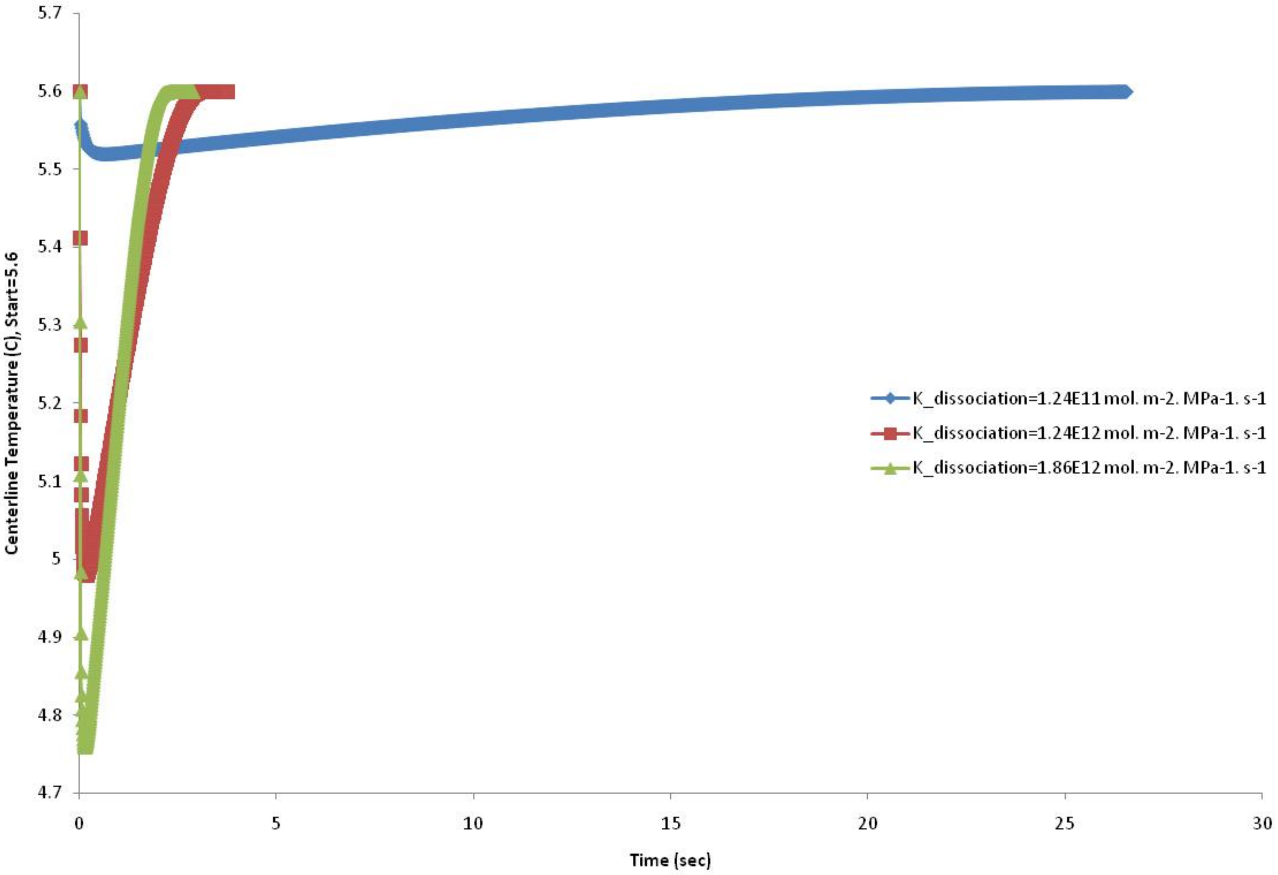

Figure 5.6 Theoretical centerline temperature with respect to time and dissociation rate constant.

Figure 5.6 shows the dramatic change the kinetic rate constant has on both dissociation time and centerline temperature. Moridis et al., **(**2005**)** have cited a 15-fold increase in the kinetic rate constant in porous media compared to the value reported by Kim et al, 1987 (1.78 x 10^{12} mol. m^{-2}.MPa^{-1}.s^{-1} vs. 1.24 x 10^{12} mol.m^{-2}.MPa^{-1}.s^{-1}, respectively). The range reported here is also 15-fold and the results are dramatic. At the high end, 1.86 x 10^{12} mol.m^{-2}.MPa^{-1}.s^{-1}, the hydrates completely dissociate in under 5 seconds, accompanied by a large drop (0.85K) drop in system temperature. The temperature depression predicted by the largest kinetic rate constant (approximately equivalent to that given by Moridis) is almost exactly equal to that observed in our experiments (see figure 5.2).

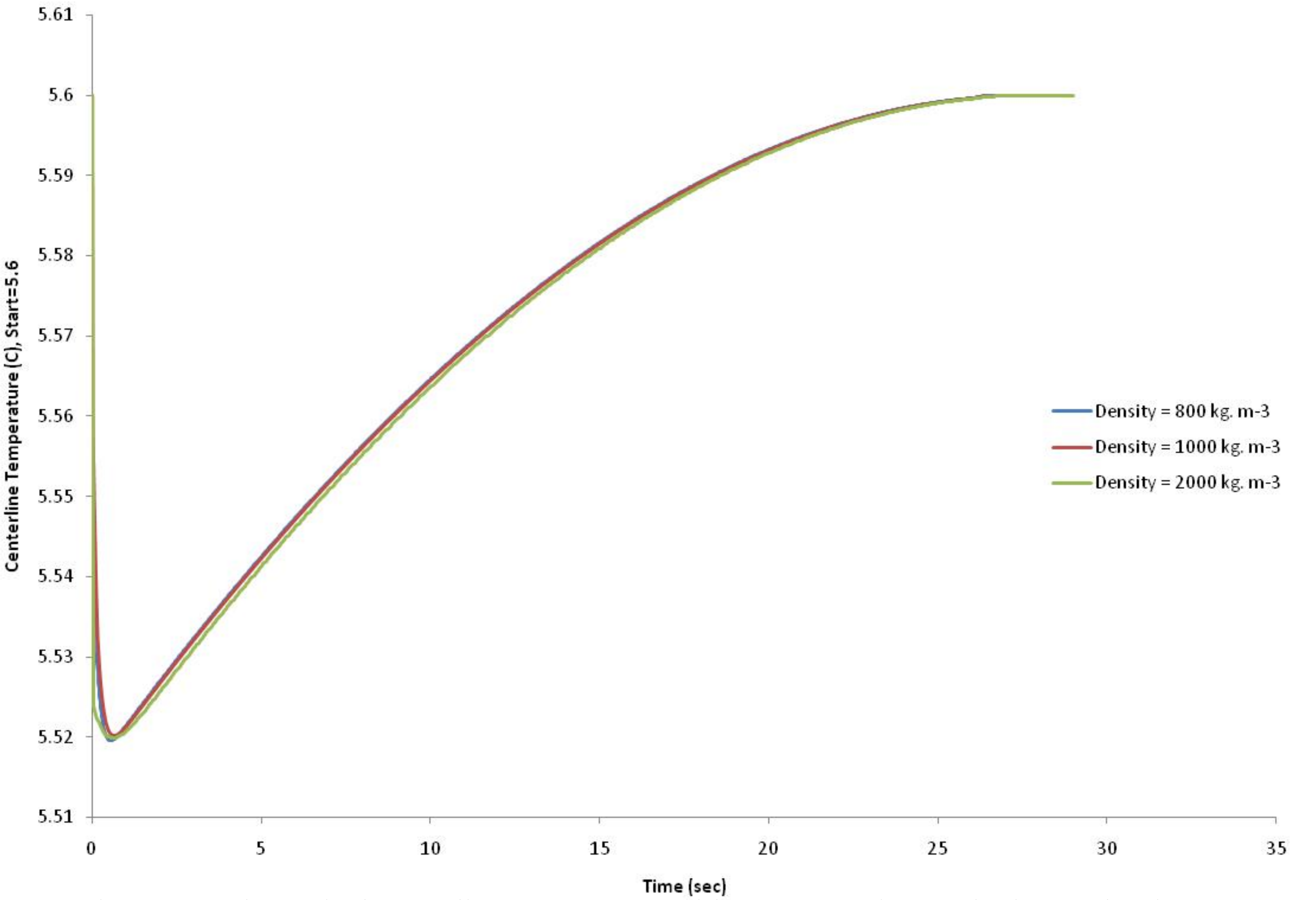

Figure 5.7 Theoretical centerline temperature with respect to time and mixture density

Figure 5.7 illustrates the effect of density on dissociation temperature. Curiously, a 2.5-fold increase in mixture density (altered by sediment/water/hydrate/gas mixture composition and porosity) did not alter the maximum temperature drop in the system appreciably. Although a more dense system shows a slightly slower and lower temperature response (i.e. its temperature showed less decrease) to hydrate dissociation, as would be expected, such a change is relatively minor. This low response is most likely due to the low mass and small geometry of the total system, where even relatively large changes in density would account for a small shift of mass.

A similar situation is seen in figure 5.8, the effect of thermal conductivity of the mixture on centerline temperature.

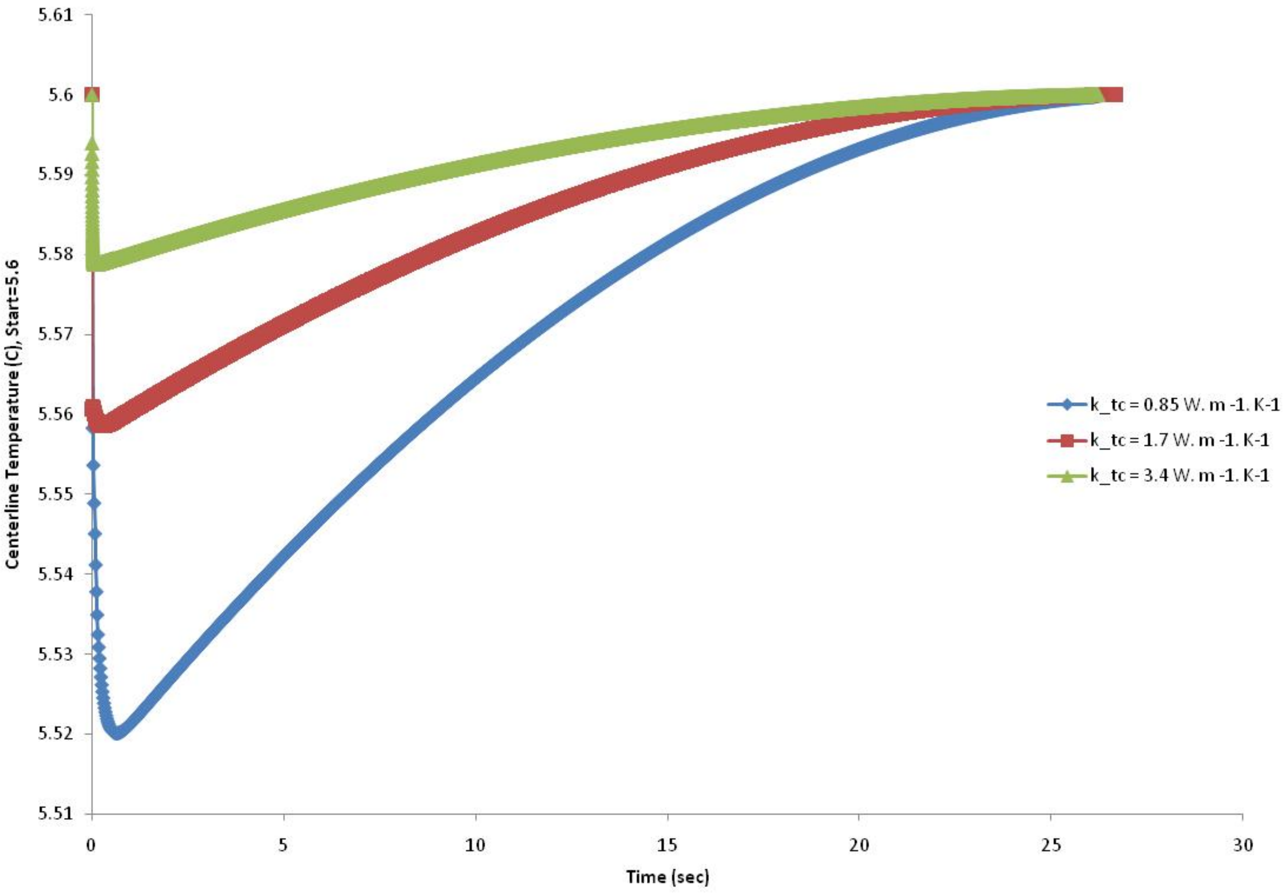

Figure 5.8 Theoretical centerline temperature with respect to time and mixture thermal conductivity

The results agree well with those predicted by Gerami and Pooladi-Darvish (2007), whose sensitivity analysis using a modified Kim model predicted very little change in temperature over a 4-fold change in thermal conductivity. Such a temperature drop occurred during non-equilibrium cooling of the system by hydrate dissociation via depressurization. Their “non-equilibrium” stage represents the entire lifetime of this simulated experiment. This is because the amount of hydrate present in these studies is insufficient to overcome warming of the system by the bath and thus cannot hold the system at the equilibrium temperature dictated by the system pressure.

Initial thermal conductivity values (0.85 W.m^{-1}.K^{-1}) were obtained from an equation regressed from data by Waite et al. (2002) shown below in figure 5.9. However, it should be noted that hydrate fractions were achieved without the use of free water (hydrates were formed from ice particle conversion), and therefore higher values of thermal conductivity are expected in a water-saturated system. This is shown in Moridis et al., 2005 where an average value of 3.2 was obtained for a sand/water mix.

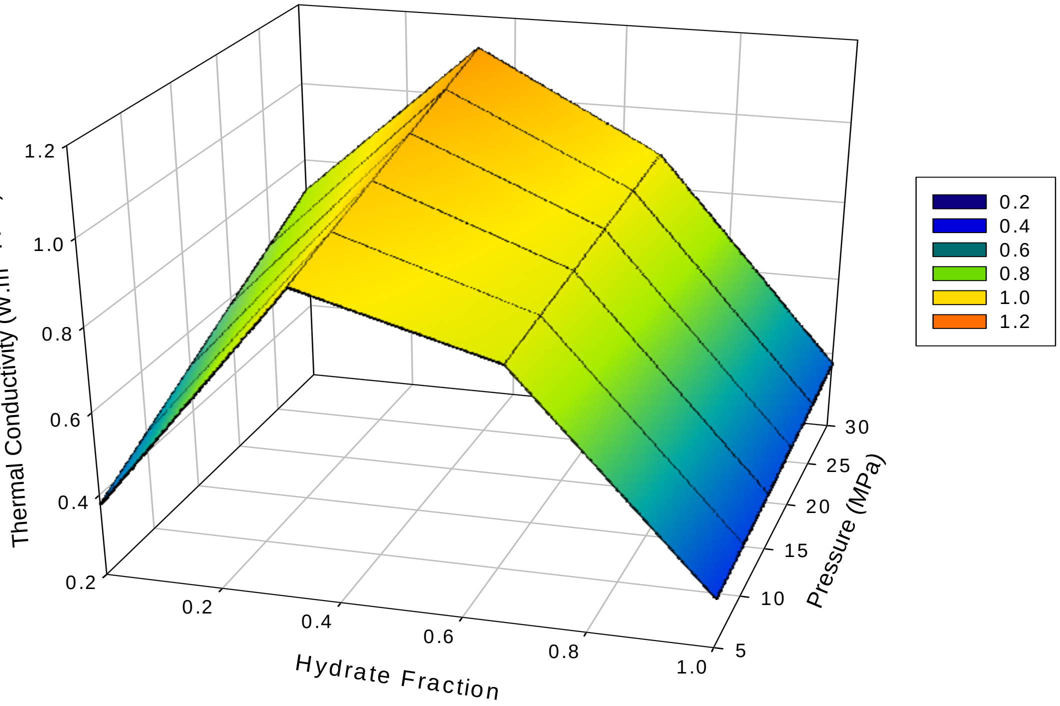

Figure 5.9 Thermal conductivity in hydrate bearing sand as a function of pressure and hydrate fraction

Of particular distinction among the sediments studied was particle size which, correspondingly, controlled pore and hydrate size. Figure 5.10 shows the sensitivity of the heat transfer model to various hydrate radii.

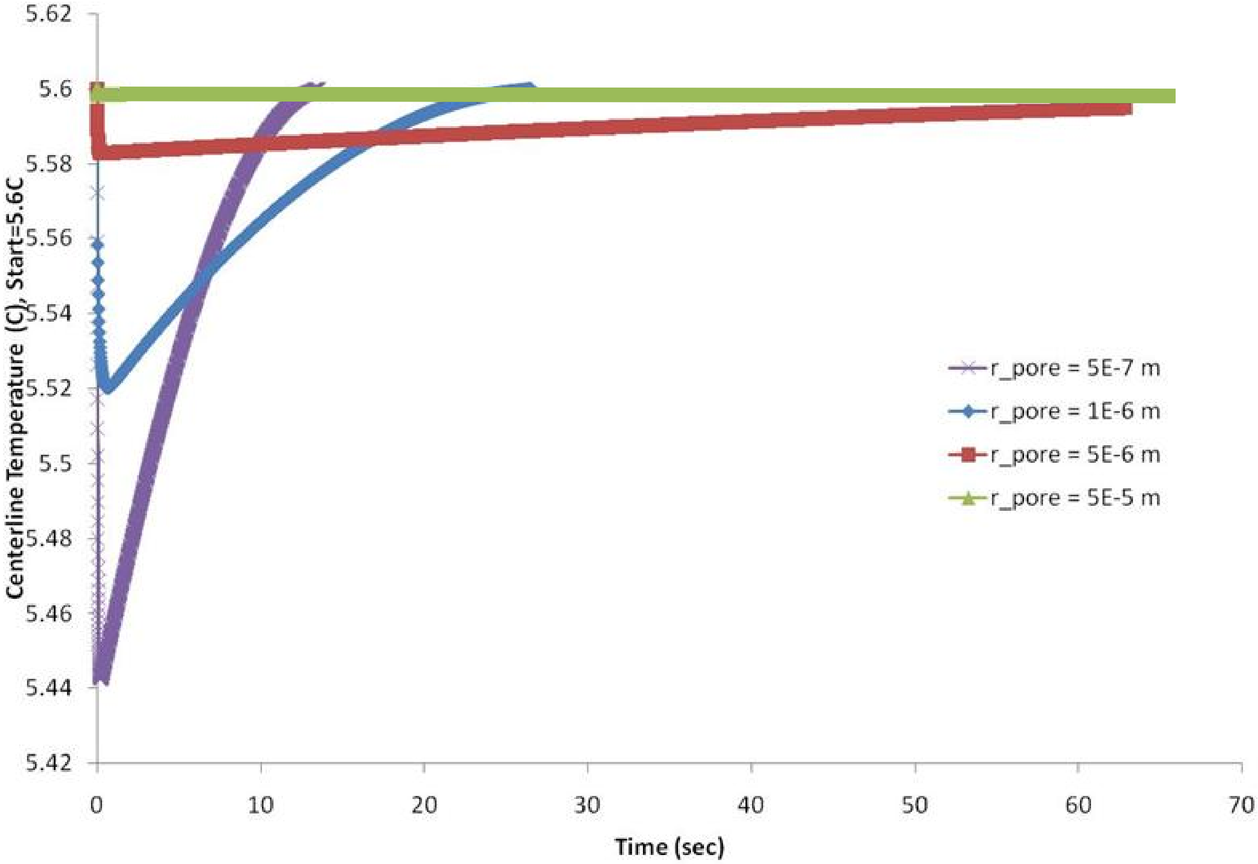

Figure 5.10 Theoretical centerline temperature with respect to time and average particle radius (m)

While an order of magnitude shift in particle size does not display the same thermal effect as an order of magnitude shift in kinetic rate constant, it nevertheless is influential on both temperature depression and length of hydrate dissociation. This is to be expected – larger particles have a smaller surface area to volume ratio (SAV), and thus their dissociation rate should be comparatively slower than smaller particles (the SAV varies as 3/radius). Correspondingly, because the reaction rate is slower, the temperature depression is less, but the length of time it remains depressed increases. Conversely, an order of magnitude decrease in particle size yields a 10-fold increase in SAV with a much more rapid decrease in temperature, but for a shorter amount of time (the hydrates expend themselves more quickly).

Of similar linear-type-dependence is the influence on fugacity difference on temperature depression. This variable represents the **initial** difference between the system pressure and the calculated equilibrium pressure at time t=0. Again, it should be reiterated that this difference was **not** constant throughout dissociation, as equilibrium pressure is exponentially dependent on system temperature. Figure 5.11 illustrates the result graphically.

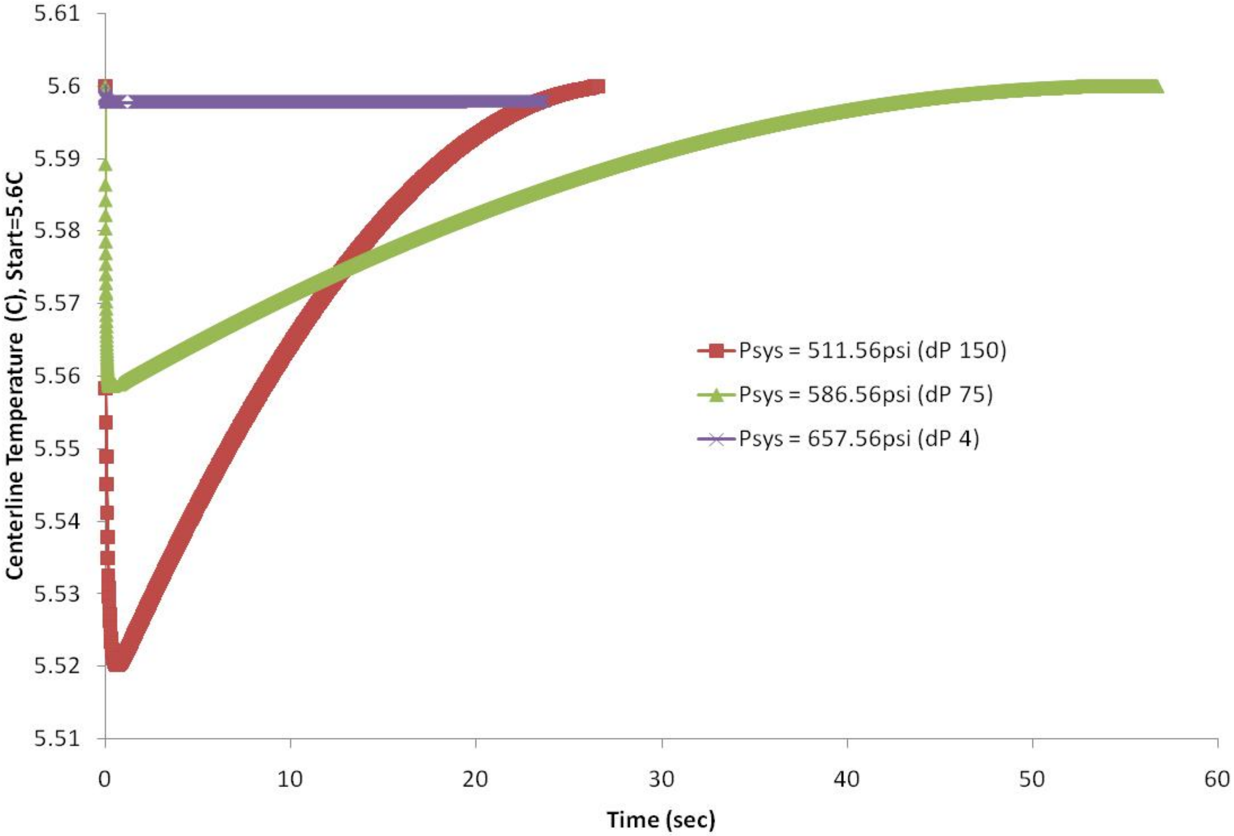

Figure 5.11 Theoretical centerline temperature with respect to time and initial fugacity difference (psi)

As noted, the centerline temperature shows a relatively linear dependence on initial fugacity difference. That is, the 150psi difference results in a maximum temperature depression of approximately 0.08K, and half of such a difference, 75psi, results in a 0.04K maximum decrease. Note that at 0 psi difference between equilibrium and system pressure, no hydrate is allowed to dissociate and, as shown in the 4psi difference case, approaching such a value results in a sustained, low-level temperature depression (truncated at 20 seconds). This effect is comparable to having large average pore radii or lowered kinetic rate constants.

Next, the effect of initial wall temperature was studied. As is expected, increasing the initial temperature of the reaction increased the initial dissociation rate, leading to a greater maximum temperature depression and a shorter "life span" for the hydrates in the sediment. Note that the y-axis of figure 5.12 is dimensionless temperature (current temperature/initial temperature) for the sake of comparison. The lowest temperature dip, corresponding to a wall temperature of $8^{o}C$ (281K) is 0.3K.

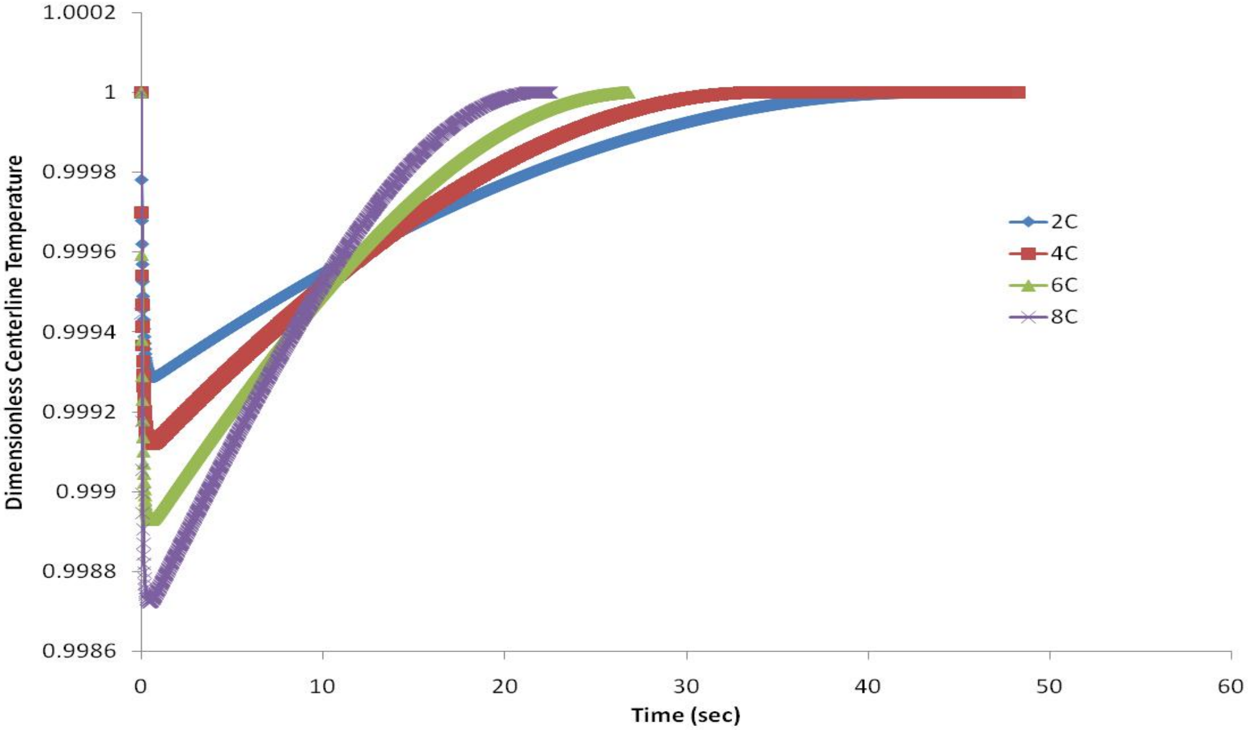

Figure 5.12 Theoretical dimensionless centerline temperature with respect to time and initial wall temperature

Finally, the effect of changing the activation energy, E_a, was studied. As with many thermodynamic (as opposed to kinetic) variables, the magnitude of change amongst measurements does not vary by an order of magnitude. Kim et al., 1987, report a value of 78.3 kJ/mol of methane, while more recent work by Moridis cites a value of 89.7 kJ/mol of methane. It should be noted that the value reported by Kim had a stated error of 4.5 kJ/mol, and thus Moridis' value appears statistically significantly different. Figure 5.13 shows the results of the sensitivity analysis using Moridis' value for the kinetic rate of dissociation (1.86×10^{12} mol. m^{-2}. MPa^{-1}. s^{-1}) for comparison.

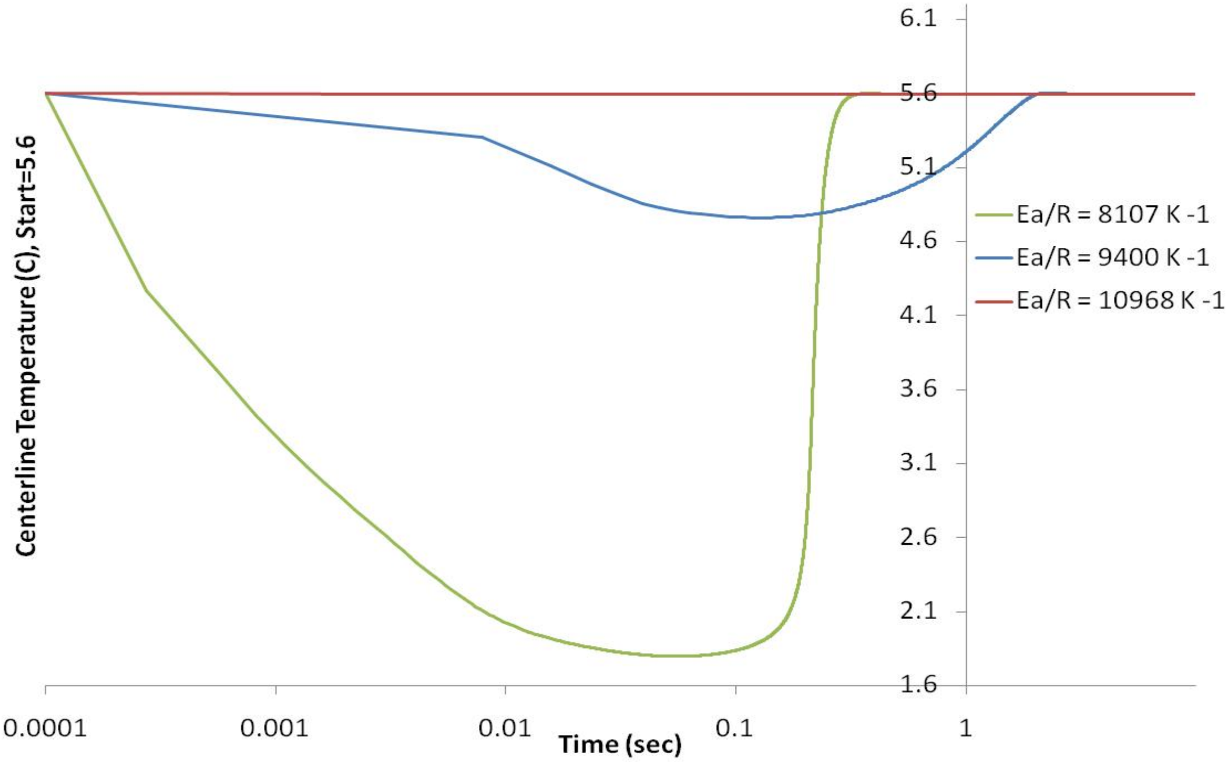

Figure 5.13 Theoretical dimensionless centerline temperature with respect to time and activation energy divided by the universal gas constant (K^{-1}), $k^{dissociation}=1.86\times10^{12}$ mol. m^{-2}. MPa^{-1}. s^{-1}

Figure 5.13 was cast on a log (time) scale because, for low hydrate activation hydrate activation energies combined with the enhanced value for dissociation rates, the simulated cell cools down extremely quickly and loses much of its hydrate content doing so. Physically, this follows logic: a system with a high rate of reaction and very little energetic "barrier" will react rapidly and completely. Also, due to the isothermal boundary condition (essentially equivalent to an infinitely high surface convection coefficient) and total loss of hydrate (a cooling factor), the system warms rapidly. This is opposite the systems which dissociate more slowly, maintaining some "useable" fraction of hydrate and, consequently, a temperature depression, for extended periods of dissociation. The range of activation energies shown in figure 5.13 spans 30% about the mean, given by Kim et al. 1987. As shown, the system temperature responds exponentially to changes in activation energies, as predicted by equation 5.10. Also, it appears that the activation energy value predicted by Moridis et al. is too high, given the low temperature depression (indicative of low-hydrate dissociation) when compared to figure 5.2.

From the above sensitivity studies, it is clear that the assumed pore/particle size, the kinetic rate of dissociation, and the activation energy of the dissociation reaction collectively play a major role in determining both the temperature change and the duration of temperature depression in the system. However, when modeling a system, it is best to have experimental data to back up assumptions and findings from the model. Such data were obtained and are shown below in the following section.

5.2 Experimental Validation and Parameter Extraction

5.2.1 Experimental Dissociation Results

Dissociation experiments were performed on both sediments and, in the case of the Gulf of Mexico sediments, also performed using a system with simulated seawater. As mentioned in chapter 4, dissociation of the system was accomplished using depressurization, and was done in a “step down” manner. The reason for this was two-fold. The first was a purely physical limitation: large pressure drops (initially performed between 400 and 500psi) caused damage to the back-pressure regulator on the system, and thus smaller pressure drops were used. Second was that a smaller pressure drop allowed for a greater separation between cooling caused by hydrate decomposition and cooling simply from depressurization – also, rapid depressurization of the system at high pressure drops caused disruption of the sediment column, leading to erroneous temperature behavior (and repetition of the experiment). Figure 5.14 shows both the temperature and pressure behavior of the system during a typical depressurization run.

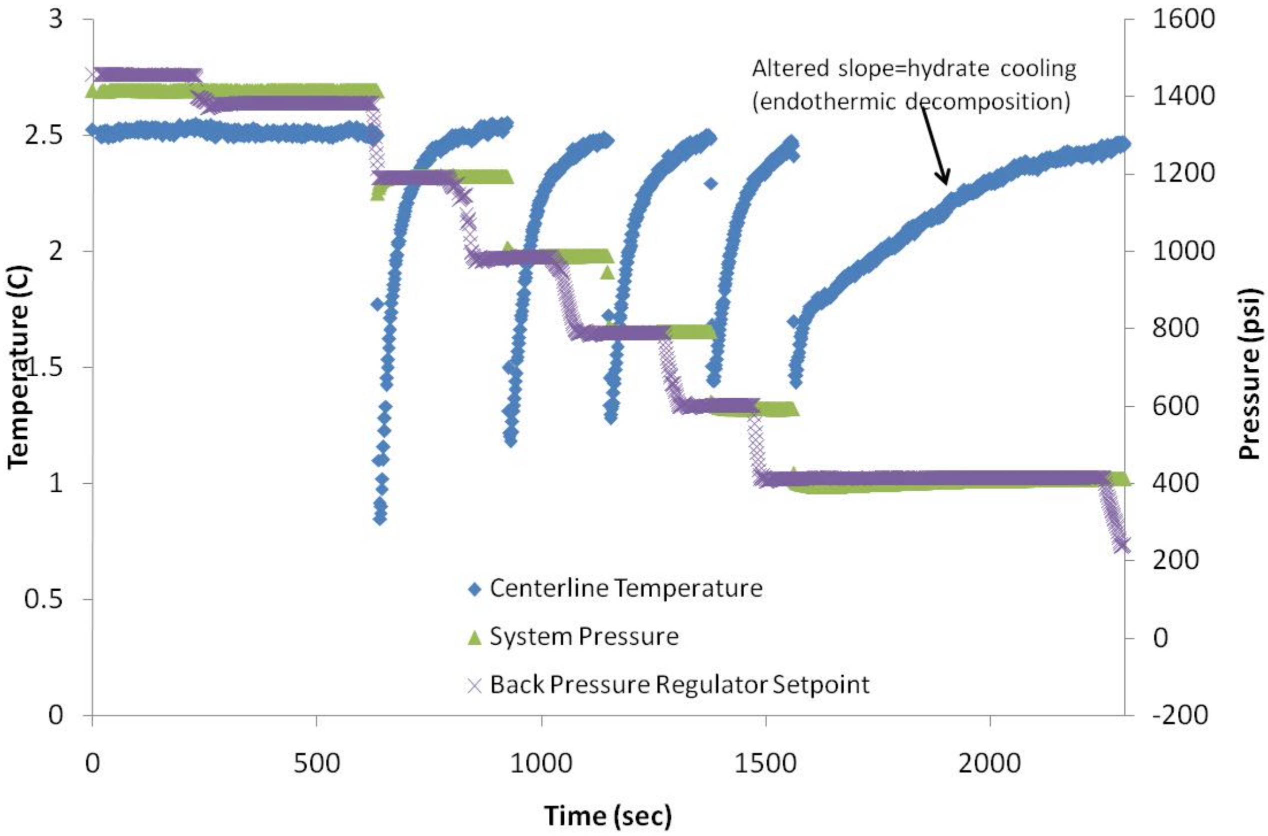

Figure 5.14 Temperature and pressure profiles for hydrate decomposition via depressurization, $T_{initial}$=2.5°C, $P_{initial}$=1500psi

As shown in this trial, the temperature and pressure in the beginning of the run (t < 500s) were held constant. Then, the back-pressure regulator (BPR) was adjusted to a set point approximately 200 psi lower than the current system pressure. After establishing a constant pressure at the BPR, usually within a few seconds, the outlet valve to the system was opened, putting the system and the BPR in communication and allowing gas to escape. Of note in this procedure is that the valve opening was not a "step change" event – that is, the valve was opened over the course of 5-10 seconds to allow for a rapid, yet non-instantaneous depressurization. This preserved the sediment column integrity, yet still allowed for the observation of time-dependent thermal behavior. This procedure is slightly different than the one imposed on the simulations shown in figures 5.5 – 5.13, as depressurization there was initiated as a step-change event, and thus the time of the maximum temperature depression occurred earlier. After the system underwent a depressurization, it was allowed to return to the given bath temperature (in this case, 2.5^{o}C). The depressurization cycle was then repeated. Note that for each of the depressurizations above the hydrate point, the system returns to bath temperature rather rapidly (20 sec). However, once the system was depressurized below its equilibrium pressure, the hydrate contained within the sediment began to dissociate and, due to the endothermic nature of dissociation, cooled the cell, corresponding the decreased rate of warming observed. Again, the system was allowed to warm and then, as per protocol, was depressurized in 200psi increments.

Results for the "dissociation steps," where an altered warming curve was observed, are shown below in figure 5.15. Note that in each case, the predicted fugacity difference is calculated based upon equilibrium predictions in pure water and pure methane. No shifts in equilibrium were observed at temperatures below 6^{o}C, although at 10^{o}C in the DI water condition, the hydrate began dissociating at pressures higher than predicted (at 10.4^{o}C, P_{eq} is predicted to be 1096 psi, $P_{observed}$ was 1146). The reason for this shift in thermodynamics is not completely clear, although it should be noted that at higher temperatures, the slope of the hydrate equilibrium curve (pressure vs. temperature) increases more rapidly, and thus shifts in equilibrium become more apparent. Likewise, at lower temperatures, the effect may simply be masked by an error on the measurement (differences are shown in figure 4.15). For convenience of interpretation, the figure is cast in terms of dimensionless temperature, much like figure 5.12.

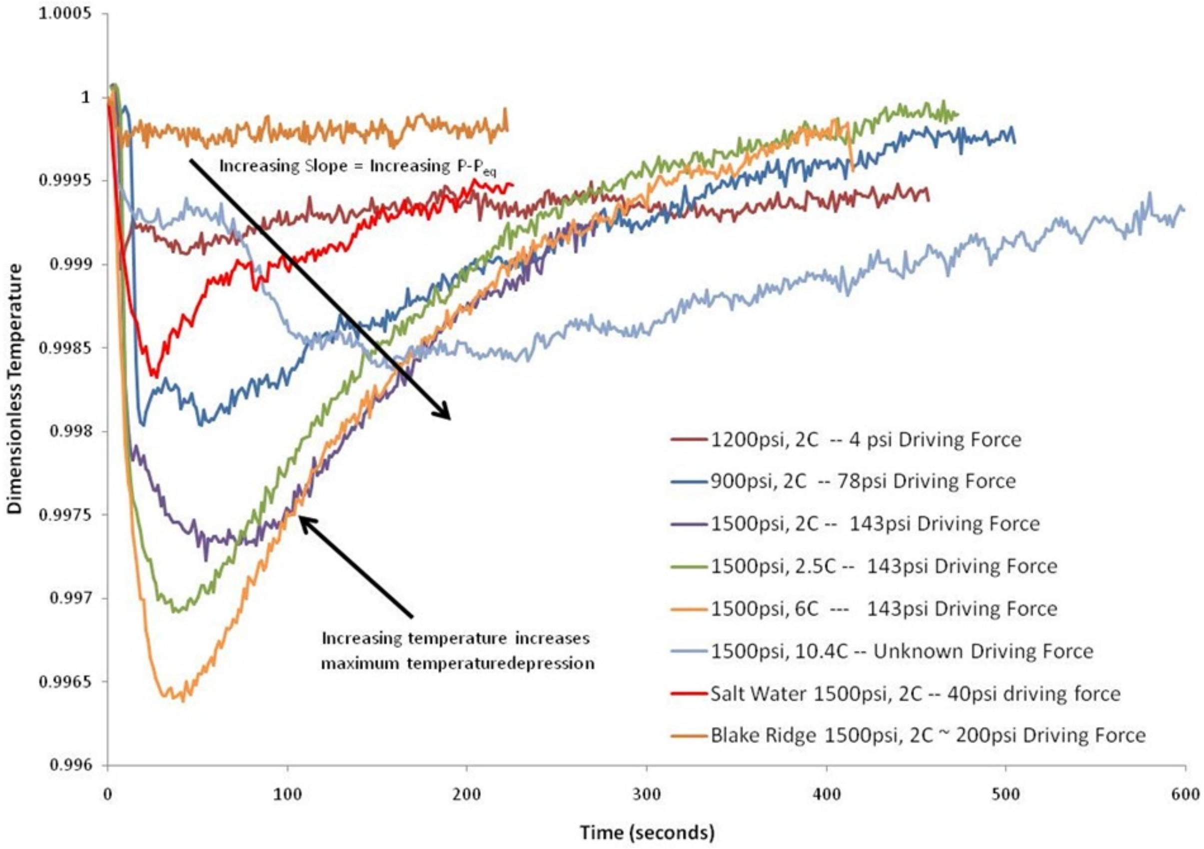

Figure 5.15 Centerline temperature profiles for hydrate decomposition via depressurization for a range of temperatures, pressures, and fugacity differences

The dissociation or, more precisely, the centerline temperature profile, of each of the experiments represented in figure 5.15 follows essentially a 3-stage process. In the first stage, there is rapid cooling due to dissociating hydrates. It should be reiterated that each of these curves began with a 200psi step-down in pressure. While the pressure drop was not instantaneous, it was done in a consistent manner between runs and always held at the same magnitude by a back-pressure regulator. The second stage of the process occurred when the amount of cooling produced by the dissociating hydrates equaled the rate at which heat entered the system through the walls of the reaction vessel. This led to a zero-slope in the temperature vs. time curve (t~20 seconds) and signaled the point of maximum temperature depression. Finally, the third stage was the point at which the rate of hydrate dissociation was outpaced by the rate of heat input through the walls of the vessel, which occurred for all times greater than 30 seconds. The system then asymptotically warmed to the prescribed bath temperature, and all hydrates dissociated.

There are numerous interesting characteristics and trends that can be seen from figure 5.15:

1. Higher temperatures, for the same driving force, result in a greater temperature depression observed.

Each warm-up curve for similar driving forces also had approximately the same slope (at $t > 20$ seconds). This is expected; higher temperatures yield faster dissociation kinetics and the accompanying faster drop in temperature that results in faster cooling. Additionally, the same trend is observed in computer simulations of the model (figure 5.12). It should be noted that the magnitude of temperature depression cannot simply be attributed to the expansion of the gas at different pressures. That is, while the system at 6^oC was dropped from 735psi to 535psi and the 2^oC system was dropped from 516psi to 316psi, the temperature depression predicted is opposite to that predicted by adiabatic expansion of the gas at each condition. For clarity, figure 5.16 demonstrates this effect: at lower initial pressures, a 200psi drop should result in a lower final temperature of the system, assuming cooling is solely due to gas expansion. However, the opposite is observed in this system, indicative of the hydrate's role in cooling the system, and the effect of temperature on the rate of dissociation.

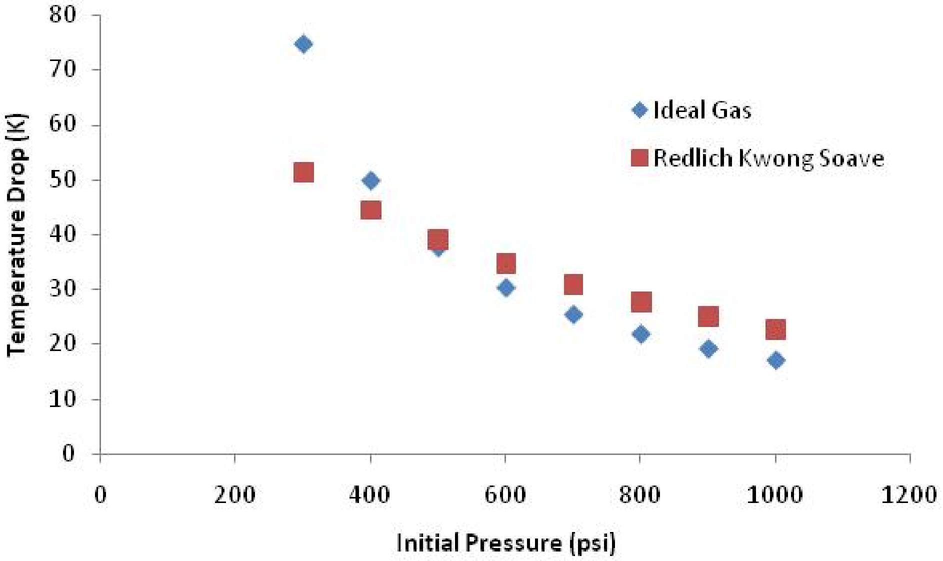

Figure 5.16 Predicted temperature drop vs. pressure for an instantaneous decrease of 200 psi in pressure (adiabatic expansion)

2. Altering the fugacity difference affects the slope of the warm-up curve (stage 3).

This, too, is expected and is predicted by the heat transfer model (figure 5.11). For a system with a high driving force, it is to be expected that it will cool off more rapidly than a system with a low driving force – a higher rate of dissociation is predicted. Additionally, it will tend to warm more quickly, as the amount of hydrate in the system at the point of maximum temperature depression is actually lower than a similar system with a lower fugacity difference. Quite simply, a fixed amount of hydrate that exhausts itself more quickly will warm more quickly. Similarly, hydrates dissociated with very little fugacity difference will demonstrate less of a temperature depression, but will persist in such a depression for longer time frames. This can clearly be seen in the case of the 4 psi fugacity difference (shown in dark red from figure 5.15). It should be noted that the 10.3°C case seems to exhibit much of the "slower" warm up features present in the low-fugacity-difference dissociations done at lower temperatures. As mentioned previously, the 10°C case began dissociating at pressures above the theoretically calculated equilibrium pressure. Therefore, while the driving force was unknown, the nature (slope) of the warm-up curve suggests dissociation occurred between 4 and 75 psi of the equilibrium pressure. Repeated runs to determine the actual equilibrium point suffered from hydrate formation inside the gas sparger, and higher-temperature runs were aborted.

3. Large particle sizes, and consequently large pore spaces, yield slower production of gas from hydrates, even at high driving forces.

The low rate of cooling in the large-grained and porous sediments was noted. For even a 200 psi difference between system pressure and theoretical hydrate equilibrium pressure, a very slight temperature depression was observed. However, the temperature depression, much like that in the low-fugacity-difference hydrate dissociations in fine-grained sediments, was sustained. In terms of the 3-phase dissociation model, phase 2 for large-grained sediments was almost 2 orders of magnitude longer than those in fine-grained sediments. This is backed by computer models (figure 5.10, green line). For a fixed amount of enclathrated gas, distribution in many small spheres will yield a faster dissociation of the hydrate simply due to the greater surface area. Conversely, if all the hydrate is contained within one large sphere (or other large volumes), dissociation will proceed more slowly due to a lower surface area, and will necessarily take longer to fully expend the hydrate mass. Such hydrate accumulations might be found in highly fractured consolidated sediments such as chalk deposits or large-grained sand beds within the sediment. Thus, if extracting methane from such sources (high hydrate concentrations), it would be expected that longer times would be necessary to fully recover gas, and although these experiments predict a slight temperature drop (above the ice point), reservoir-scale systems would necessitate more precise approximations of total hydrated gas to determine if ice formation would present a problem.

4. Hydrates formed in salt water appear, for similar conditions in DI water, to dissociate more rapidly.

This can be seen in the salt-water hydrate dissociated with only a 45 psi driving force compared to a DI water hydrate dissociated with a 75psi driving force. In such a case, the magnitude of the temperature depression was slightly less, although the slope of the warm-up curve was greater, in general, than the DI water case. As shown in chapter 4, the presence of salt water appeared to form more highly fissured hydrate/sediment systems (due to increased formation rates), and therefore the increased surface area of such hydrates might explain the more rapid warm-up. More experiments are needed, preferably in a consolidated system to control hydrate/sediment expansion, to fully explore the effect of salt on dissociation kinetics.

5.2.2 Model Results Extracted from Experiment

While the simplified model of equation 5.9 seems to do very well in predicting the qualitative behavior (phases 1, 2, and 3) of the experimental results, there are shortcomings which limit its usability, and require some a posteriori tuning of the coefficients. The most noticeable discrepancy between model and experiment is the time scale for dissociation. Note that in experimental results, dissociations take on the order of 400 to 600 seconds to complete (as evidenced by the centerline temperature returning to bath temperature). In most model predictions, save for those in the low-end of the rate constant or driving force value, or those on the high-end of pore size or activation energy, dissociations occurred on the order of

30 seconds – almost an order of magnitude less than observed. This means that either the values inputted to the model (based upon known sediment and hydrate properties) were incorrect, or the model is not accounting for a particular factor during dissociation. Clearly, the model is deficient. A factor left out due to complexity, but one of the most likely causes for the discrepancy, is mass transport through the media as hydrates dissociate. Prior to dissociation, the sediment and hydrate column starts out as a relatively solid mass with low porosity (as evidenced by the lack of visual volume change before and after hydrate formation). However, upon hydrate dissociation, the column is rapidly changed from a solid mass to one which contains a high degree of localized porosity (a fluidized bed); the volume of gas released from the sediment is between approximately 10 and 40 times the volume of the sediment/water. Consequently, as gas is released, the thermal conductivity of the system drops rapidly (methane is approximately two orders of magnitude worse at conducting heat than is a sediment/hydrate mixture; 0.034 W. $m^{-1}.K^{-1}$ and 3.2 W. $m^{-1}.K^{-1}$, respectively). Additionally, because the system is unconfined, porosity may increase to levels not typically observed in systems where a confining stress is present. As such, model values for the thermal conductivity ought to be altered in a stepwise (or, in the case of a robust model, smooth) fashion mid-run; during phase 1, the system is allowed to behave as a "solid" hydrate/sediment system, and during phase 2 and 3, the system thermal conductivity is lowered to reflect gas infiltration/porosity increase (Lee Chin, personal communication, 2007). Unfortunately, however, such a gross oversimplification is not suitable for extracting the primary variable in the experiment, kinetic rate constants. As seen in figure 5.8, decreasing the overall thermal conductivity merely results in an increased magnitude of temperature drop, with the system returning to equilibrium at approximately the same time

over the range of thermal conductivity values. To achieve the desired result – that is, extended dissociation times, thermal conductivity must be altered on a localized basis, something which is not possible given the fundamental assumption of temporal and spatial independence of thermal conductivity, density, and specific heat in this simple model. Additionally, the dynamic nature of the system (internal and external conduction) is not accounted for, and leads to a more rapid cooling based upon not only isothermal boundary conditions, but also on a sustained, erroneously high internal thermal conductivity.

Given these caveats, however, some assessments of the kinetics of dissociation in previously-hydrate-bearing sediments can be made. To achieve the temperature depressions seen in these experiments (specifically, 6^{o}C, 143 psi driving force) while maintaining a thermal conductivity more closely approximating that of water with little hydrate (0.85 $W.m^{-1}.K^{-1}$), a kinetic rate constant of 15.03 times that of Kim et al., 1987, is necessary (1.86 x 10^{12} $mol.m^{-2}.MPa^{-1}.s^{-1}$). This does agree with values given by Moridis et al., 2005, but as pointed out previously, causes hydrates to dissociate an order of magnitude too quickly. Unfortunately, as both a low thermal conductivity and high dissociation rate correlate strongly with increased temperature depressions, it is unknown whether this value is valid, or is simply an overestimate to accommodate a lack of internal mass transfer. It is important to note that in the Kim/Bishnoi experiment, hydrates were dissociated in a stirred bath, theoretically eliminating heat transfer to the hydrate particles, resulting in the acquisition of the fundamental rate constant of dissociation for methane hydrates. Additionally, recent work by Gupta (2007) suggests that on a large (reservoir) scale, gas production from hydrates may simply be modeled as a heat transfer problem, thereby eliminating the necessity of obtaining/fitting kinetic data for each type of sediment or hydrate environment. In the systems studied in this work, however, both heat transfer and kinetics were coupled, as evidenced by the temperature drops in figure 5.15. Fortunately, from experiment it can be seen that for the larger-grained systems (Blake Ridge sediments), little temperature drop was observed, and therefore might serve as a system which approaches isothermal dissociation. Dissociation results from hydrates formed at 900 and 1200psi (both at 2^{o}C) in Blake Ridge sediment are shown below in figure 5.17.

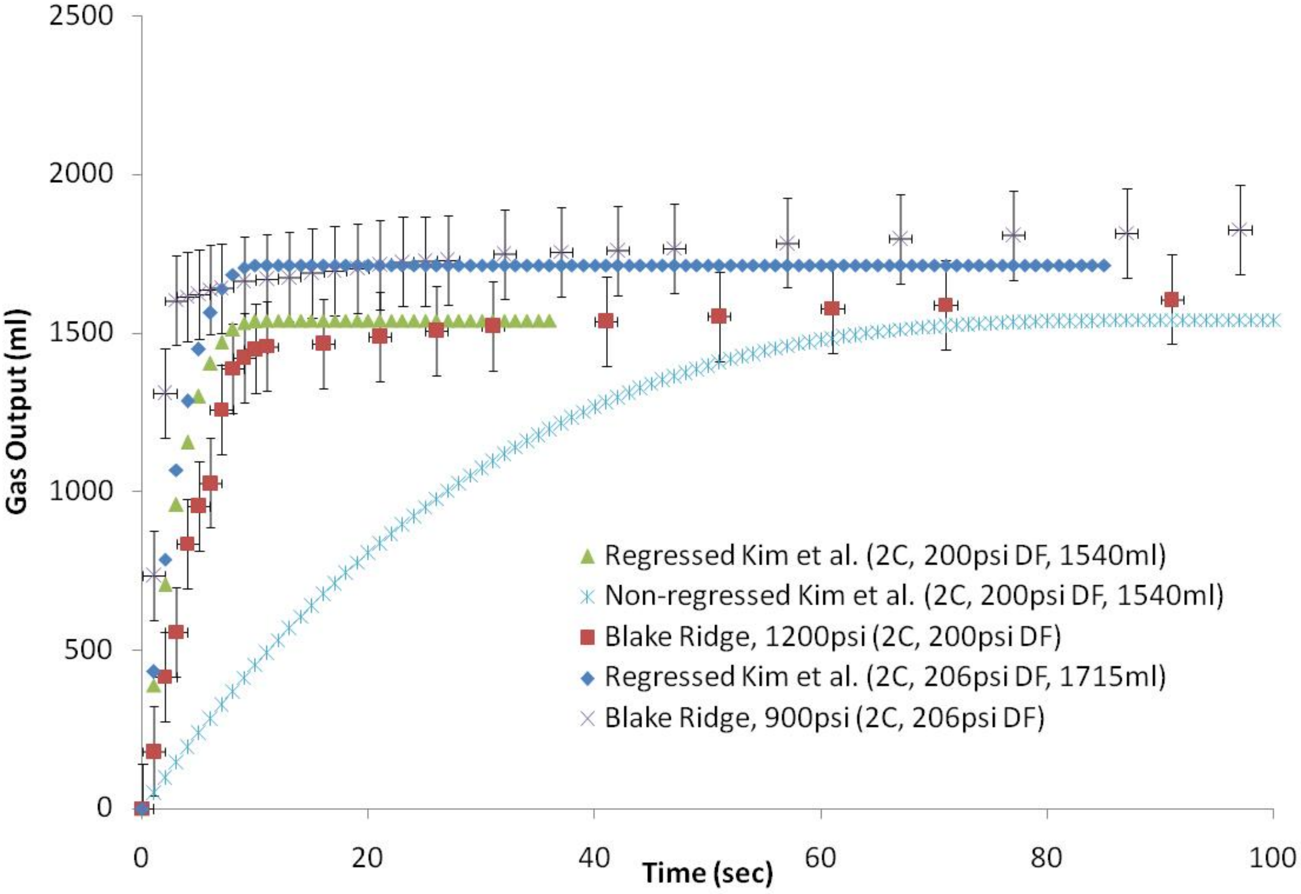

Figure 5.17 Experimental and predicted gas evolution in Blake Ridge sediments

Figure 5.17 shows both the experimental data points (with error bars) and the kinetic model of Kim et. al (1987) regressed to fit the data. Note that the only value of the model regressed was the intrinsic rate constant, k. To obtain a value for both sets of experiments (the 900 and

1200psi runs), a basic least-squares regression was performed simultaneously on each of the data sets. The result of the regression was a k-value of approximately 30.07 times larger (6.28×10^{12} mol.m^{-2}.MPa^{-1}.s^{-1}) than that reported by Kim. While such a large discrepancy is unusual, it is supported by plotting the original k-value (1.24×10^{11} mol.m^{-2}.MPa^{-1}.s^{-1}) against experimental data (also shown in figure 5.17). Clearly, the gas evolution predicted using a non-regressed rate constant is too low, even in light of the error on the measurement, to explain the experimental results. In should be reiterated that this system was essentially isothermal despite hydrate formation (closely approximating the Kim/Bishnoi system) – in fact, non-isothermal lowering of the temperature, as seen in the Gulf of Mexico system, would have resulted in *better* agreement with the model, not worse.

From the above results, it seems clear that sediments affect hydrate dissociation kinetics in a way that is not entirely heat-transfer related. While it is still uncertain what hydrate property is altered, a reasonable assumption may be the way in which the hydrates form, thus exposing different, non-spherical geometries for dissociation. From figure 5.17, dissociation (and concomitant gas release) occurs at rates greater than predicted, suggesting that either the original measurement of the rate constant was incorrect, or, more likely, the means by which the surface area of the hydrates is estimated behaves non-ideally/spherically. Although no attempt has been made in this work to determine such sphericity, it seems reasonable to assume that hydrates do not, in fact, grow as perfect spheres between grains of sediment particles. Additionally, while the Kim et al. model of equation 5.10 does make an attempt to correct for non-spherical particles (it, too, is a variable parameter), the order of magnitude difference between results in this work and those obtained by Kim et al suggests that a modification of the model might be necessary. At the very least, a better/more thorough means of characterizing hydrate growth in porous media should be performed.

In summary, it appears as though results of hydrate dissociation in previously hydrate bearing host sediments, while affected by system geometry and heat transfer to the medium, show that sediments do, in fact, alter dissociation kinetics by at least an order of magnitude, in agreement with literature using homogeneous sands. Such alterations are most likely due to the means by which hydrates form in and around grains and pore spaces. Work performed in previously hydrate bearing host sediments using a consolidated core holder will substantially eliminate many of the experimental difficulties shown here, and microtomographic work to visualize *in situ* hydrate formation at a microscopic level will elucidate surface area and microstructural hydrate character.

Chapter 6: Conclusions and Future Work

This dissertation is primarily concerned with understanding the effects of previously-hydrate-bearing sediments from natural sites that can serve as hosts to methane hydrates. This has practical application not only in understanding how hydrates form within different types of sediment under different conditions, but also how they dissociate. The fundamental concept is: understand first where and how hydrates will form in economically recoverable deposits, and then understand what effect the sediment will have in obtaining the gas trapped within such deposits. This study systematically focused on aspects that are outlined below.

6.1 A Novel Device to Study Hydrates

This portion of the work demonstrated a new device, namely, Flexible Study of Hydrates (FISH), constructed “from the ground up” at Brookhaven National Laboratory. The unit is of flexible design, suitable for high pressure operation (up to 2000 psi), and can obtain pressure and temperature data of comparable accuracy to current formation methods. Additionally, it allows for a visual observation of hydrate formation/decomposition behavior on a macroscopic scale – a 30 cm view-through windowed cell allows a complete view from gas inlet to gas outlet, a setup not normally used in hydrate studies. Additionally, the system’s flexibility lies in its size and portability. Multiple gas inlets, outlets, and sampling ports, all metered with precision pressure/temperature/and flow measurements allow for the study of hydrates in a variety of media and pressure conditions simultaneously.

A customized gas sparger consisting of glass wool sandwiched between two wire meshes was developed to allow a more even bubble distribution within the column and also prevent a possible hydrate plugging condition within the gas feed lines. The custom gas sparger was subsequently fitted with a Gore-Tex membrane which allows true water-resistance but finely dispersed gas flow to the column. A LabView setup was created to not only passively acquire pressure and temperature readings, but also actively control flow, allowing studies in the future to easily operate either isochorically or isobarically. Collectively, the FISH unit and the Labview allowed us to gather data that are discussed here.

6.2 Hydrate Formation in Previously-hydrate-bearing Sediments From Natural Sites

To ascertain the effect of porous media on hydrate formation kinetics, previously-hydrate-bearing sediment samples were obtained from the Gulf of Mexico and the Blake Ridge, a formation off the eastern coastline of the United States. This work represents the first time such media has been used to reform hydrates, and demonstrates an important "iteration" in the realism of experiments done to determine the feasibility of using hydrates as an energy source. The two sediments were chosen not only because of availability, but also due to their nature: Gulf of Mexico is a fine grained (< 10 μm) sediment with porosities less than 0.49, while Blake Ridge sediments are somewhat larger (21 μm) with a high percentage being sand (> 125 μm) and high porosity (0.51).

Two different methods were developed to form hydrates in such sediments: continuous low-flow conditions to desired pressures, or a rapid "charge and hold" condition. It was shown that at flows less than 200 ml CH_4/min to the cell, there was a marked increase in gas uptake by hydrates with this method. This suggests that on laboratory time scales, complete hydration of the water content inside the system may be achieved, despite using fully-saturated sediments. Additionally, it was observed that the enhanced gas uptake was observed only in the Blake Ridge sediments, perhaps due to the increased gas holdup from the larger grained sediments.

The static-charge formation method revealed hydrate formation rates in fine-grained sediments that behaved essentially as mass-transfer-controlled reactions, with close agreement to theory in gas uptake over time frames of two weeks. In larger, more porous sediments, gas uptake rates were significantly enhanced compared to fine-grained sediments. The reason for this is possible residual gas holdup in the system (also seen in the continuous flow-regime) leading to erroneously high gas absorption rates. However, the substitution of salt water, a thermodynamic inhibitor, to the fine-grained systems allowed for gas uptakes 8 times that predicted by diffusion alone. This result agrees with hydrates formed from salt water in the absence of porous media, and suggests that enhanced formation kinetics in sediments/porous media may simply be due to the salts/impurities present, not the nature of the media itself.

Morphologically, it appeared that under both flow regimes, the coarse Blake Ridge sediments formed larger masses of hydrate which excluded sediments, whereas the fine-grained Gulf of Mexico sediments typically formed tiny nodules/veins against the glass of the reactor, with the remaining gas uptake apparently arising from hydrates dispersed within the column of sediment. From a purely hypothetical economic standpoint, it would appear at hydrates in more coarsely-grained and porous sediments would be the most likely candidates for the ideal “massive” hydrate accumulations, with fine-grained sediments forming non-dispersed hydrate accumulations at faults/fissures/non-homogeneities within the sediment.

6.3 Hydrate Dissociation in Previously-hydrate-bearing Sediments

This portion of the work occurred at the end of the formation cycle described above. A step-down pressure reduction method was used to decompose hydrates, as opposed to thermal stimulation, which allowed for control of driving force (fugacity difference) during hydrate dissociation. Results of gas production rates for a variety of temperature and pressure conditions were measured, and the cooling effect of hydrate decomposition was modeled using the rate equation of Kim et al. for kinetics in the hopes that fundamental hydrate/sediment properties could be extracted.

Temperature depressions within the sediments at the time of dissociation agree, qualitatively, with heat transfer models. Fine-grained systems yield larger temperature drops as compared to coarse grained systems. The reason for this is that for a given volume of hydrate forming between sediment grains, the surface area of hydrate, which plays an integral role in the rate of decomposition, is increased as sediment sizes decrease. Additionally, as expected, larger differences between the system and hydrate equilibrium pressures yielded increased rates of reaction. Finally, increased temperatures yielded the as-expected increase in reaction rates, with the final conclusion being that, qualitatively, sediments demonstrate little difference in dissociation characteristics than do other types of porous media which serve to simulate actual sediments. However, as will be discussed shortly, the need to understand **how** the hydrates form around the different sediments is of critical importance, as the surface area estimation involved in modeling and predicting hydrate behavior can be easily *qualitatively* captured, but quantitatively results have not agreed well with experiments on pure hydrates in porous media-free systems.

Due to the modeling complexity of the unconsolidated, almost-fluidized, non-isothermal system, it was difficult to deconvolute the effect of the sediment/hydrate heat transfer properties (thermal conductivity, density, specific heat) from the pure chemical kinetics occurring at decomposition. From estimates based on the temperature drop in fine-grained sediments and gas production rates in coarse-grained systems, it appears that the intrinsic kinetic rate constant for hydrate dissociation in porous media is between 15 and 30 times that given by Kim et al. ($1.86 - 6.28x10^{12}$ $mol.m^{-2}.MPa^{-1}.s^{-1}$). While heat transfer, unfortunately, appears to be coupled in obtaining such values (kinetics should be independent), even in the most ideal, essentially isothermal case, the values from Kim et al. underpredict gas production rates.

6.4 Future Work

Given the above findings, the following suggestions for future work and analysis on gas hydrate formation and decomposition are made:

1) Perform work in a consolidated system using previously-hydrate-bearing sediments as hosts.

As mentioned, the FISH unit has the capability of running different high pressure cells in parallel. To enhance the realism of the experiment, it would be ideal to have a system where a confining stress could be applied (much like one would find below the mudline), essentially restricting sediment and fluid movement upon hydrate formation. Such work would make modeling tremendously easier, but would also give a better and more accurate understanding of the type of macroscopic growth morphology in different sediments. The availability of previously-hydrate-bearing sediments at Brookhaven National Laboratory (BNL) is a very useful step in accurately predicting reservoir behavior, and while results in unconsolidated systems show little difference to results predicted by typical porous media (glass beads, well-characterized sands, etc.), the presence of an overburden stress could feasibly alter hydrate growth *within* sediment particles, rather than *around* the particles, as would be expected in an unconfined system. Of course, for thoroughness, it would also be interesting to test sediments from different locations around the world, as grain morphology (and mineralogy) is expected to alter hydrate growth.

2) Perform microscopic investigations of hydrate formation between grains for methane hydrate

Early computerized microtomographic (CMT) work on tetrahydrofuran hydrates at BNL has shown *tremendous* potential for understanding the way in which hydrates grow in porous media. As mentioned, part of the difficulty in modeling and predicting hydrate dissociation behavior has been in the assumptions made about the surface area of the hydrate exposed. In this work and in others, hydrates have been considered spherical particles between sediment grains that behave as shrinking cores. Based upon the rate-constant discrepancy between hydrates formed in pure water and hydrates formed in porous media, it seems that such an assumption is flawed. Being able to quantify hydrate surface areas by physical observation would be a huge advance in the science, and would alleviate the need for the very rough approximations which, in light of BNL's CMT work, are almost certainly invalid. Work should be done using methane gas, however, and not THF, as gas infiltration to the media, and subsequent hydrate guest availability is substantially different between these two systems (as is the fundamental crystallographic structure). Additionally, for realism, single-phase hydrate formation (that is, from dissolved methane in water) would be ideal, as areas of high gas flux, resulting in two-phase hydrate growth, ought to be the exception, rather than the rule.

3) Different gas mixtures, and possible CO_2 sequestration

This suggestion is, perhaps, the most distant goal. It would be interesting to see the effect of mixtures of gas within a sediment matrix. While most of the world's deposits of hydrates in oceanic sediments are structure I from essentially pure methane, there are sites where hydrates have formed from thermogenic gas (resulting in structure II). Due to sII's inherently more stable structure, it stands to reason that the method/morphology of formation between and within sediment grains might be altered (e.g. they might form in smaller pores or more tortuous geometries more easily). Mixtures of methane and ethane, the most likely combination of sII forming guests, could easily be studied in the same way as methane hydrates are, and would actually require less extreme pressures.

Along with such work, a natural extension would be the study of CO_2 sequestration. Recent work by Bjorn Kvamme, in conjunction with ConocoPhillips (personal communication, August 2007) has demonstrated the feasibility of $CH_4 \rightarrow CO_2$ hydrate exchange. The work was performed in consolidated sandstones, and it would certainly be interesting to determine if such an effect were possible in unconsolidated (yet overburdened) sediments, given the apparent propensity of hydrates to form in clusters and non-ideal shapes.

Works Cited

Asher, G.B. Development of a Computerized Thermal Conductivity Measurement System Utilizing the Transient Needle Probe Technique - an Application to Hydrates in Porous Media, Colorado School of Mines, 1987.

Ballard, A., A non-ideal hydrate solid solution model for a multi-phase equilibria program, Ph. D. Thesis, Colorado School of Mines, Golden, CO, USA, 2002

Baughn, J.W., Rossi, M. Two-Dimensional Transient Heat Conduction Analysis Using Spreadsheets. Heat Transfer Engineering, 13 (2), 1992, 0145-7632.

Bernard, B.B., Brooks, J.M., Sackett, W.M., Natural gas seepage in the Gulf of Mexico, Earth and Planetary Science Letters, Volume 31, Issue 1, June 1976, pp 48-54.

Booth, J.S., Clennell, B., Pecher, I.A., Winters, W.J., Relle, M.K., and Dillon, W.P.: “Laboratory investigation of gas hydrate genesis in sediments--Modes of occurrence, volumes and growth patterns: Gas Hydrates in Nature--Results from Geophysical and Geochemical Studies, European Geophysical Society, XXIII, General Assembly, Nice, France, Spring 1998, 452 p.

Boswell, R. Resource potential of methane hydrate coming into focus. *Journal of Petroleum Science and Engineering*, 56 (1-3), 2007, pp. 9-13.

Castaldi, Marco. Personal communication, June 4th, 2006

Chakoumakos, B.C., Oak Ridge National Laboratory, Personal Communication, July 2007

Chakoumakos, B. C., Rawn, C.J., Rondinone, A.J., Marshall, S.L, Stern L.A., Circone, S., Kirby, S.H. ‚Jones, C. Y., Ishii, Y., “The Use of Rigid Body Constraints in Rietveld Refinements of Neutron Diffraction Data of Clathrate Hydrates,” *Proceedings of the Fourth International Conference on Gas Hydrates*, Yokohama, Japan, 19-23 May, 2002, pp. 655-658.

Cherskiy, N.V., Tsarev, V.P. Evaluation of the reserves in the light of search and prospecting of natural gases from the bottom sediments of the world’s ocean. Geologiya i Geofizika 5, 1977, 21–31 (in Russian).

Chin, L., ConocoPhillips, Bartlesville, OK, Personal Communication, August 2007

Clarke, M. and Bishnoi, P. R.: 2001, Determination of the active energy and intrinsic rate constant of methane gas hydrate decomposition, Can. J. of Chem. Eng. 79(2), 2001, 143–147.

Clarke, M. A., Pooladi-Darvish, M., and Bishnoi, P. R. A method to predict equilibrium conditions of gas hydrate formation in porous media, Ind. Eng. Chem. Res., V38, 1999, pp. 2485-2490.

Claypool, G.W., and Kvenvolden, K.A. Methane and other hydrocarbon gases in marine sediments: Ann. Rev. Earth Planetary Science, 11: 1983, pp. 299-327.

Clennell, B. M., Hovland, M., Booth, J. S., Henry, P., and Winters, W. J. Formation of natural gas hydrates in marine sediments 1. Conceptual model of gas hydrate growth conditioned by host sediment properties, Journal of Geophysical Research, V104, No. B10, 1999, pp. 22985-23003.

Collett, T.S. Energy Resource Potential of Natural Gas Hydrates. AAPG Bulletin 2002 86: 1971-1992

Dai, J., Xu, H., Snyder, F., Dutta, N. Detection and estimation of gas hydrates using rock physics and seismic inversion: Examples from the northern deepwater Gulf of Mexico. The leading Edge 2004 23: 60-66

Dallimore, S.R., Uchida, T., Collett, T.S.: "Scientific Results from JAPEX/JNOC/GSC Mallik 2L-38 Gas Hydrate Research Well, Mackenzie Delta, Northwest Territories, Canada", Geological Survey of Canada Bulletin 544, February 1999.

Danckwerts, P. V., Trans. Faraday Soc., 46, 1950, pp.300

Dillon, W. P., Nealson, J. W., Taylor, M. H.. Seafloor collapse and methane venting associated with gas hydrate on the Blake Ridge: Cause and implications to seafloor stability and methane release. In Natural Gas Hydrates: Occurrence, Distribution, and Detection (Paull, C. K., Dillon, W. P. ed.) American Geophysical Union, Washington D.C., 2002, pp. 211-233.

Dooley, JJ. *Energy R&D in Japan*. Pacific Northwest National Laboratory. PNNL-12214. Washington, D.C. May 1999.

Dowd, B.A., Andrews, A.B., Marr, R.B., Siddons, D.P., Jones, K.W., and Peskin, A.M. Advances in x-ray computed microtomography at the NSLS. Presented at 47th Annual Denver X-Ray Conference, Colorado Springs, Colorado, August 3-7, 1998. In: T.C. Huang, R. Barton, V.E. Buhrke, J.V. Gilfrich, G.J. Havrilla, R. Jenkins, I.C. Noyan, P.K. Predecki, D.K. Smith, and R.L, Snyder (Editors), Advances in X-Ray Analysis, Vol. 42. Plenum Publishing Corp., New York, 1999, pp. 171-180

Dvorkin, J., Nur, A.: "Elasticity of High-Porosity Sandstones: Theory for Two North Sea Datasets", Geophysics, 61, 1996, pp. 1363-1370.

Dvorkin, J., Prasad, M., Sakai, A., Lavoie, D.: “Elasticity of Marine Sediments”; GRL, 26, 1999, pp. 1781-1784.

Dyadin, Y.A., Larionov, E.G., Manakov, A.Y., Zhurko, F.V., Aladko, E.Y., Mikina, T.V., Komarov, V.Y. Clathrate Hydrates of Hydrogen and Neon, *Mendelev Comm.* 5, 1999a, pp. 171-172

Dyadin, Y.A., Larionov, E.G., Manakov, A.Y., Zhurko, F.V. Double clathrate hydrates of tetrahydrofuran and xenon at pressures up to 15kbar, Mendelev Comm. 9 (2), 1999b, pp. 80-81

Ecker, C., Dvorkin, J., Nur, A. M., Estimating the amount of gas hydrate and free gas from marine seismic data. Geophysics, 65, 2000, pp. 563-575.

Eaton M., Mahajan D., Flood R. A novel high-pressure apparatus to study hydrate-sediment interactions *Journal of Petroleum Science and Engineering*, 56 (1-3), 2007, pp. 101-107.

Eid J. A Methodology and Tutorial for Thermal Modeling with PC Spreadsheets. Heat Transfer Engineering 8(2): 1987, 95-107

Englezos, P., N. Kalogerakis, P.D. Dholabhai and P.R. Bishnoi, Kinetics of Formation of Methane and Ethane Gas Hydrates, *Chem. Eng. Sci.*, 42, 1987, pp. 2647-2658.

Feeser, V. Gas hydrate formation in deep sea sediments. The role of the sediment-mechanical process control. DGMK Tagungsbericht V9706, 1997, pp.51-60.

Fick, A. "On liquid diffusion" Phil. Mag 10: 1855, pp. 30-39

Gerami S., Pooladi-Darvish M. Predicting gas generation by depressurization of gas hydrates where the sharp-interface assumption is not valid *Journal of Petroleum Science and Engineering*, 56 (1-3), 2007, pp. 146-164.

Ginsburg, G.D., Soloviev, V.A. Submarine gas hydrate estimation: theoretical and empirical approaches. Proceedings of Offshore Technology Conference, Houston, TX, vol. 1, 1995, pp. 513–518.

Gornitz, V., Fung, I. Potential distribution of methane hydrates in the world’s oceans. Global Biogeochemical Cycles 8, 1994, pp. 335– 347.

Gupta, A., Methane Hydrate Dissociation Measurements And Modeling: The Role Of Heat Transfer And Reaction Kinetics, Ph. D. Thesis, Colorado School of Mines, Golden, CO, USA, 2007

Handa, Y. P. Effect of hydrostatic pressure and salinity on the stability of gas hydrates, *J. Phys. Chem.*, 94, 6, 1990, pp. 2652 – 2657

Handa, Y.P., Stupin, D. Thermodynamic properties and dissociation characteristics of methane and propane hydrate in 70-A-radius silica gel pores, J. Phys. Chem., V96, 1992, pp. 8599-8603.

Harvey, L.D.D., Huang, Z. Evaluation of potential impact of methane clathrate destabilization on future global warming. Journal of Geophysical Research 100, 2905–2926.1995, pp. 3–8.

Helgerud, M., Dvorkin, J., Nur, A., Sakai, A., Collett, T.: "Elastic Wave Velocity in Marine Sediments with Gas Hydrates: Effective Medium Cooling", GRL, 26, 1999, pp. 2021-2024.

Himmelblau, D. M. Diffusion of dissolved gases in liquids. Chem. Rev. 64: 1964, pp. 527-550

Holbrook, W.S., Hoskins, H., Wood, W.T., Stephen, R.A., Lizarralde D., and Leg 164 Science Party. Methane hydrate and free gas on the Blake Ridge from vertical seismic profiling. Science 273, 1996, 1840–1843.

Hong, H, Pooladi-Darvish, M and Bishnoi P.R. Analytical modeling of gas production from hydrates in porous media, JCPT, vol.42, No.11, 2003, pp.45-56.

Hovland, M., and Gudmestad, O. T.,. Potential influence of gas hydrates on seabed installations. In Natural Gas Hydrates: Occurrence, Distribution, and Detection (Paull, C. K., Dillon, W. P. ed.) American Geophysical Union, Washington D.C., 2001, p.311.

Huo, Z., Hydrate Phase Equilibria Measurements by X-ray Diffraction and Raman Spectroscopy, Ph. D. Thesis, Colorado School of Mines, Golden, CO, USA, 2003.

Incropera F.P., DeWitt, D.P. Fundamentals of Heat and Mass Transfer. John Wiley and Sons, New York, 4th edition, 1996.

Iversen, N., Jørgensen, B.B., Diffusion coefficients of sulfate and methane in marine sediments: influence of porosity, *Geochim. Cosmochim. Acta* **57**, 1993, pp. 571–578

Jamialahmadi, M., Muller-Steinhagen, H., Izadpanah, M.R., Pressure drop, gas hold-up and heat transfer during single and two-phase flow through porous media, International Journal of Heat and Fluid Flow, Volume 26, Issue 1, February 2005, Pages 156-172.

Joint Industry Project, Cruise Report The Gulf of Mexico Gas Hydrate, Covering the cruise of the Drilling Vessel *Uncle John* Mobile, Alabama to Galveston, Texas Atwater Valley Blocks 13/14 and Keathley Canyon Block

151.http://www.netl.doe.gov/technologies/oil-gas/publications/Hydrates/reports/GOMJIPCruise05.pdf. Visited Sept. 21, 2007

Jones K.W., Feng H., Tomov S., Winters W.J., Prodanovic M., Mahajan D. Characterization of methane hydrate host sediments using synchrotron-computed microtomography (CMT) Journal of Petroleum Science and Engineering, 56 (1-3), 2007, pp. 136-145.

Jones, K.W., Feng, H., Lindquist, W.B., Adler, P.M., Thovert, J.F., Vekemans, B., Vincze, L., Szaloki, I., van Grieken, R., Adams, F., and Riekel, C. Study of microtomography of porous materials using synchrotron computed microtomography. In: F. Mees, R. Swennen, M. VanGeet, and P. Jacobs (Editors), Applications of X-Ray Computed Tomography in the Geosciences, Geological Society of London Special Publications, Vol. 15. The Geological Society of London, 2003, pp. 39-49.

Kamath, V. A., and G. D. Holder "Dissociation Heat Transfer Characteristics Of Methane Hydrates," *AIChE Journal*, Vol. 33, No. 2, 1987, pp. 347-350.

Kim, H. C., Bishnoi, P. R., Heidemann, R. A. and Rizvi, S. S. H.: 1987, Kinetics of methane hydrate dissociation, Chem. Eng. Sci. 42(7), 1987, pp. 1645–1653.

Kleingberg, R. Personal Communication. 2006

Kneafsey T.J., Tomutsa L., Moridis G.J., Seol Y., Freifeld B.M., Taylor C.E., Gupta A. Methane hydrate formation and dissociation in a partially saturated core-scale sand sample. *Journal of Petroleum Science and Engineering*, 56 (1-3), 2007, pp. 108-126.

Kono H.O., Narasimhan S., Song F., Smith D.H. Synthesis of methane gas hydrate in porous sediments and its dissociation by depressurizing. *Powder Technology*, 122 (2-3), 2002, pp. 239-246.

Kvamme B., Graue A., Buanes T., Kuznetsova T., Ersland G. Storage of CO2 in natural gas hydrate reservoirs and the effect of hydrate as an extra sealing in cold aquifers. International Journal of Greenhouse Gas Control, 1 (2), 2007, pp. 236-246.

Kvenvolden, K.A. Methane hydrate—a major reservoir of carbon in the shallow geosphere? Chemical Geology 71, 1988, pp. 41–51.

Kvenvolden, K.A., Claypool, G.E. Gas hydrates in oceanic sediment. USGS Open-File Report 88-216, 1988, 50 pp.

Kvenvolden, K. A., Lorenson, D., *Natural Gas Hydrates*, ed. C. K. Paull and W. P. Dillon, American Geophysical Union, Washington, DC, 2001.

Lekvam, K., Ruoff, P., A reaction kinetic mechanism for methane hydrate formation in liquid water. *J. Am. Chem. Soc.* **115,** 1993, pp. 8565–8569

Lorenson T. D., Microscopic Character of Marine Sediment Containing Disseminated Gas Hydrate: Examples from the Blake Ridge and the Middle America Trench, *Ann NY Acad Sci* 2000 912: 189-194

MacDonald, G.J. The future of methane as an energy resource. Annual Review of Energy 15, 1990, pp. 53–83.

Maekawa, T., Itoh, S., Sakata, S., Igari, S.-I. and Imai, N., 1995. Pressure and temperature conditions for methane hydrate dissociation in sodium chloride solutions. *Geochem. J.* **29**, pp. 325–329.

Mahajan, D., Kotzle, T.F., Klooster, W.T., Brammer, L., McMullan, R.K., and Goland, A.N. Crystal Growth, Structure Characterization, and Schemes for Economical Transport: *An Integrated Approach to the Study of Natural Gas Hydrates*. Ann. N.Y. Acad. Sci. 912 940 (2000).

Mak, T. C. W. and McMullan, R. K. Polyhedral Clathrate Hydrates. X. Structure of the Double Hydrate of Tetrahydrofuran and Hydrogen Sulfide, *J. of Chem. Phys*. 42(8), 1965, 2732.

Makogon, Y. F. and Holditch, S. A.: 2001, Experiments illustrate hydrate morphology and kinetics, Gas and Oil J. 45–50

Makogon, Y.F.,. Perspectives of development of gas hydrate accumulations. Gasovaya Promyshlennost 3, 1981, pp. 16–18 (in Russian).

Makogon, Y.F., 1997. Hydrates of Hydrocarbons. Penn Well, Tulsa, OK. 504 p.

Marshall, D.R., Saito, S., Kobayashi , R. Hydrates at high pressure: Part I. Methane–water, argon–water, and nitrogen–water systems. *AIChE J.* 10,1964, pp. 202–205

Matsumoto, R., Watanabe, Y., Satoh, M., Okada, H., Hiroki, Y., Kawasaki, M. Distribution and occurrence of marine gas hydrates. Preliminary results of ODP Leg 164. Blake Ridge drilling. Chishitsugaku Zasshi V102(11), 1996, pp. 932

McIver, R.D., Gas hydrates. In: Meyer, R.G., Olson, J.C. (Eds.), Long-Term Energy Resources. Pitman, Boston, MA, 1981, pp. 713–726.

McMullan, R., Jeffrey, G. A., *The Journal of Chemical Phys*ics, 42(8), 2725-2732, 1965.

McNair, H. M., Miller J. M. Basic gas chromatography. 1998. Wiley, New York.

Milkov, A.V. Global estimates of hydrate-bound gas in marine sediments: how much is really out there? Earth-Sci Rev 66 (3-4), 2004, pp. 183-197

Milkov, A.V., Claypool, G.E., Lee, Y.-J., Dickens, G.R., Xu, W., Borowski, W.S. and the ODP Leg 204 Scientific Party, 2003. In situ methane concentrations at Hydrate Ridge offshore Oregon: new constraints on the global gas hydrate inventory from an active margin. Geology 31, 833– 836. of ODP, Initial Reports, vol. 146 (Pt.1). Ocean Drilling Program, College Station, TX.

Monterey Bay Aquarium Research Institute (MBARI), http://www.mbari.org/expeditions/vance/images/DrillingHydrateClose.jpg, Retrieved 9/23/07

Moridis, G.J. Numerical simulation of gas production from methane hydrates, Soc. Pet. Eng. 2002, 75691

Moridis, G.J., Y. Seol and T. Kneafsey, *Studies of Reaction Kinetics of Methane Hydrate Dissociation in Porous Media*, Proceedings of the 5th International Conference on Gas Hydrates, Trondheim, Norway, June 13-16, 2005

Natarajan, V., P.R. Bishnoi, and N. Kalogerakis, "Induction Phenomena in Gas Hydrate Nucleation", *Chem. Eng. Sci.* 49, 1994, pp. 2075-2087.

NIST monograph 175. *Temperature-Electromotive Force Reference Functions and Tables for the Letter-Designated Thermocouple Types Based on the ITS-90.* Washington, D.C.: National Inst. of Standards and Technology,1993.

Nesterov, I.I., Salmanov, F.K. Present and future hydrocarbon resources of the Earth’s crust. In: Meyer, R.G., Olson, J.C. (Eds.), Long-term Energy Resources. Pitman, Boston, MA, 1981, pp. 185–192.

Parent, J.S., and P.R. Bishnoi, "Investigations Into the Nucleation Behaviour of Natural Gas Hydrates", *Chemical Engineering Communications (CEC)*, 144, 51-64 (1996).

Rawn, C. J., et al., *Proceedings of the Fourth International Conference on Gas Hydrates, Yokohama*, Japan, 19-23 May, 2002, pp. 595-598.

Rodgers, R.E., Zhang, G., Kothapalli, C., French, W.T., 2004. Laboratory evidence of microbial–sediment–gas hydrate synergistic interactions in ocean sediments. Proceedings of the 14th International Offshore and Polar Engineering Conference, Toulon, France, 2004, pp. 41–47.

Ruppel , C., Anomalously cold temperatures observed at the base of the gas hydrate stability zone on the US Atlantic passive margin, *Geology* 25, 1997, pp. 699–702

Sassen R, MacDonald IR. Evidence of structure H hydrate, Gulf of Mexico continental slope. Org Geochem 22(6), 1994, pp. 1029–1032

Selim, M.S. and Sloan, E.D., 1989. Heat and mass transfer during the dissociation of hydrates in porous media. *A.I.Ch.E. Journal* **35**, pp. 1049–1052.

Sheshadri, K., Wilder, J. W., and Smith, D. H. Measurements of equilibrium pressures and temperatures for propane hydrate in silica gels with different pore-size distributions. J. Phys. Chem. B, V105, 2001, pp. 2627-2631.

Skovborg P., Rasmussen, P. *Chemical Engineering Science* 49, 1994, pp. 1131–1143.

Sloan, E. D., 1998. *Clathrate Hydrates of Natural Gases.* 2nd Ed., Marcel Decker, Inc

Soloviev, V.A. Global estimation of gas content in submarine gas hydrate accumulations. Russian Geology and Geophysics 43, 2002, pp. 609–624.

Staykova, D.K., Hansen, T., Salamatin, A.N., and Kuhs, W.F Kinetic Diffraction Experiments on the Formation of Porous Gas Hydrates, *Proc 4th Int Conf Gas Hydrates, Yokohama.* 2002*,* pp 537–542

Stern, L.A., Kirby S.H., Durham W.B., Circone S.,Waite, W.F., 2000. Laboratory synthesis of pure methane hydrate suitable for measurement of physical properties and decomposition behaviour. In M.D. Max (Ed.) Natural gas hydrate in oceanic and permafrost environments, Kluwer Academic Publishers, Dordrecht, pp. 323-348.

Subramanian, S., *Measurements of clathrate hydrates containing methane and ethane using Raman spectroscopy*, Ph. D. Thesis, Colorado School of Mines, Golden, CO, USA, 2000.

Subramanian, S., Ballard, A., Kini, R., Dec, S., Sloan, E.D., "Structural Transitions in Methane + Ethane Gas Hydrates – Part I: Upper Transition Point and Applications," Chemical Engineering Science 55, 2000, 5763.

Suess, E., Torres, M.E., Bohrmann, G., Collier, R.W., Rickert, D., Goldfinger, C., Linke, P., Heuser, A., Sahling, H., Heeschen, K., Jung, C., Nakamura, K., Greinert, J., Pfannkuche, O., Trehu, A., Klinkhammer, G., Whiticar, M.J., Eisenhauer, A., Teichert, B., and Elvert, M. Sea floor methane hydrates at Hydrate Ridge, Cascadia margin. *In* Paull, C.K., and Dillon, W.P. (Eds.), *Natural Gas Hydrates: Occurrence, Distribution, and Detection.* Am. Geophysical Union, Geophys. Monogr. Ser., 124: 2001, pp. 87–98.

Taylor, M.H., Dillon, W.P. and Pecher, I.A. Trapping and migration of methane associated with the gas hydrate stability zone at the Blake Ridge Diapir: new insights from seismic data. *Mar. Geol.* 164, 2000, pp. 789–790.

Trehu A.M., Long P.E., Torres M.E., Bohrmann G., Rack F.R., Collett T.S., Goldberg D.S., Milkov A. V., Riedel M., Schultheiss P., Bangs N. L.,. Barr S. R,. Borowski W. S, Claypool G. E., Delwiche M. E., Dickens G. R., Gracia E., Guerin G., Holland M., Johnson J. E., Lee Y. -J., Liu C. -S., Su X., Teichert B., Tomaru H., Vanneste M., Watanabe M., Weinberger J.L. Three-dimensional distribution of gas hydrate beneath southern Hydrate Ridge: Constraints from ODP Leg 204 *Earth and Planetary Science Letters*, 222 (3-4), 2004, pp. 845-862.

Trofimuk, A.A., Cherskiy, N.V., Tsarev, V.P., Accumulation of natural gases in zones of hydrate—formation in the hydrosphere. Doklady Akademii Nauk SSSR 212, 1973, 931–934 (in Russian).

Trofimuk, A.A., Cherskiy, N.V., Tsarev, V.P. The reserves of biogenic methane in the ocean. Doklady Akademii Nauk SSSR 225, 1975, pp. 936– 939 (in Russian).

Trofimuk, A.A., Cherskiy, N.V., Tsarev, V.P., Gas hydrates–new sources of hydrocarbons. Priroda 1, 1979, pp. 18– 27 (in Russian).

Trofimuk, A.A., Tchersky, N.V., Makogon, U.F., Tsariov, V.P., 1983. Possible gas reserves in continental and marine deposits and prospecting and development methods. In: Delahaye, Ch., Grenon, M. (Eds.), Conventional and Unconventional World Natural Gas Resources. Proceedings of the Fifth IIASA Conference on Energy Resources. International Institute for Applied Systems Analysis, Laxenburg, pp. 459–468.

Turner, D. J. and Sloan, E. D., 2002. Hydrate phase equilibria measurements and prediction in sediments, Proceedings of the 4th ICGH, Yokohama, pp. 327-330.

Uchida, T., Ebinuma, T., and Ishizaki, T., Dissociation condition measurements of methane hydrate in confined small pores of porous glass, J. Phys. Chem. B, V103, 1999, pp. 3659-3662.

Uchida, T., Ebinuma, T., Takaya, S., Nagao, J., and Narita, H, Effects of pore sizes on dissociation temperatures and pressures of methane, carbon dioxide, and propane hydrates in porous media, J. Phys. Chem. B, V106, 2002, pp. 820-826.

USGS, 2002. http://marine.usgs.gov/fact-sheets/gas-hydrates/title.html. Last update September 1992.

Van der Waals, J. H. & Platteeuw, J. C., *Advances in Physical Chemistry*, 2, 1-57, 1959.

Vrentas, J. S., Vrentas, C. M. Green's function method for the solution of diffusion-reaction problems, AIChE Journal, 34 (2), 1988, pp. 347-349

Waite, W.F., deMartin, B.J., Kirby, S.H., Pinkston, J. , Ruppel, C.D. Thermal conductivity measurements in porous mixtures of methane hydrate and quartz sand, *Geophys. Res. Lett.* **29**,2002, 24.

Wegrzyn, J.E., Mahajan, D, Gurevich, M. Catalytic routes to transportation fuels utilizing natural gas hydrates. Catalysis Today 50: 1999, pp. 97–108.

Wentworth, C.R. A scale of grade and class terms for clastic sediments. Jour. Geology, 30, 1922, pp. 377-392.

Weston, K. C. Heat transfer simulation using productivity tools, Proc. Summer Computer Simulation Conf. of the Society for Computer Simulation, 1988, pp. 260-265.

Winters, W.J., Waite, W.F., Pecher, I.A. Comparison of Methane Gas Hydrate Formation on Physical Properties of Fine- and Coarse-Grained Sediments, AAPG Hedberg Conference, Sept. 12-16, 2004, Vancouver, BC, Canada.

Yousuf, M., Qadri, S.B., Knies, D.L., Grabowski, K.S., Coffin, R.B., Pohlman, J.W.,“Novel results on structural investigations of natural minerals of clathrate hydrates,” *Applied Physics A-Materials Science & Processing*. Springer Verlag, New York, NY, 2003.

Zehner, P. Impuls-, Stoff- und Wärmetransport in Blasensäulen Teil 1: Strömungsmodell der Blasensäule und Flüssigkeitsgeschwindigkeiten. *Verfahrenstechnik* 16, 1982, 347-351

Appendix A: Brooks Mass Flow Controller Certificate

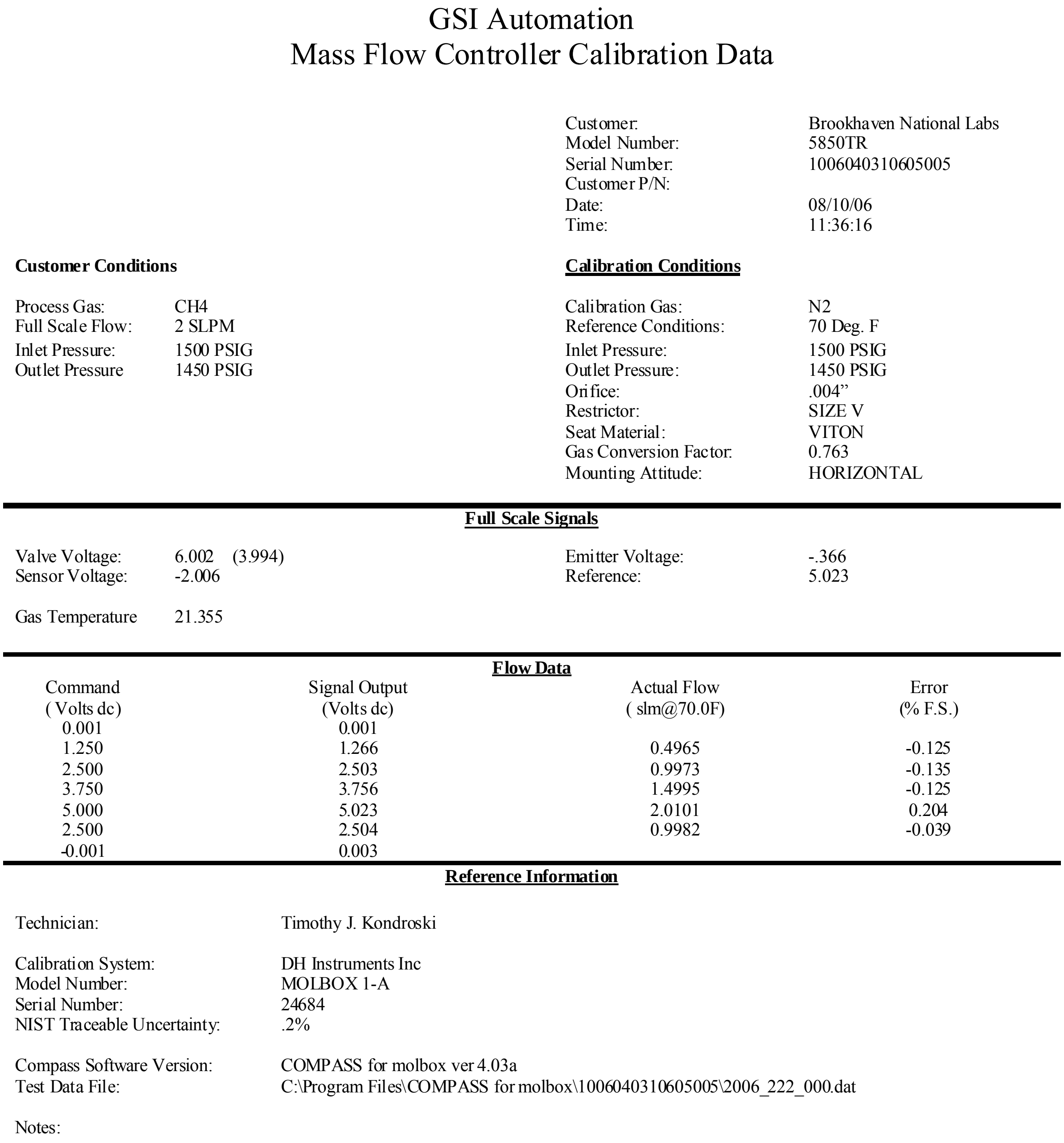

GSI Automation
Mass Flow Controller Calibration Data

Customer:	Brookhaven National Labs
Model Number:	5850TR
Serial Number:	1006040310605005
Customer P/N:	
Date:	08/10/06
Time:	11:36:16

Customer Conditions		**Calibration Conditions**	
Process Gas:	CH4	Calibration Gas:	N2
Full Scale Flow:	2 SLPM	Reference Conditions:	70 Deg. F
Inlet Pressure:	1500 PSIG	Inlet Pressure:	1500 PSIG
Outlet Pressure	1450 PSIG	Outlet Pressure:	1450 PSIG
		Orifice:	.004”
		Restrictor:	SIZE V
		Seat Material:	VITON
		Gas Conversion Factor:	0.763
		Mounting Attitude:	HORIZONTAL

Full Scale Signals

Valve Voltage:	6.002 (3.994)	Emitter Voltage:	-.366
Sensor Voltage:	-2.006	Reference:	5.023
Gas Temperature	21.355		

Flow Data

Command (Volts dc)	Signal Output (Volts dc)	Actual Flow (slm@70.0F)	Error (% F.S.)
0.001	0.001		
1.250	1.266	0.4965	-0.125
2.500	2.503	0.9973	-0.135
3.750	3.756	1.4995	-0.125
5.000	5.023	2.0101	0.204
2.500	2.504	0.9982	-0.039
-0.001	0.003		

Reference Information

Technician:	Timothy J. Kondroski
Calibration System:	DH Instruments Inc
Model Number:	MOLBOX 1-A
Serial Number:	24684
NIST Traceable Uncertainty:	.2%
Compass Software Version:	COMPASS for molbox ver 4.03a
Test Data File:	C:\Program Files\COMPASS for molbox\1006040310605005\2006_222_000.dat

Notes:

Appendix B: Pressure vs. Time Formation Tables

Table B.1 Gulf Of Mexico pressure vs. time formation data for 10.3^{o}C, 1500psi, deionized water formation conditions

Time (s)	Pressure (psi)
1129.99	1505.96
42505.52	1495.20
85015.76	1493.94
127526.03	1492.80
170039.32	1490.39
212550.06	1491.19
255060.59	1489.02
297571.17	1489.02
340081.69	1487.99
382592.39	1487.41
425102.87	1487.53

Table B.2 Gulf Of Mexico pressure vs. time formation data for $6^{o}C$, 1500psi, deionized water formation conditions

Time (s)	Pressure (psi)
2019.30	1502.38
41859.40	1483.99
83729.88	1483.19
125580.35	1477.93
167432.48	1476.78
209283.19	1481.13
251133.73	1479.53
292984.09	1479.64
334854.34	1477.35
376701.58	1477.70
418564.53	1475.18
460410.66	1480.10
502281.10	1476.44
544131.59	1479.30

Table B.3 Gulf Of Mexico pressure vs. time formation data for 2^{o}C, 1500psi, deionized water formation conditions

Time (s)	Pressure (psi)
35075.95	1503.93
125256.56	1499.35
210428.54	1497.06
295599.62	1494.43
380770.56	1493.86
470950.99	1491.23
561131.76	1489.62
651312.38	1488.59
771555.13	1487.33
821655.42	1487.45
851715.46	1486.65

Table B.4 Gulf Of Mexico pressure vs. time formation data for 2°C, 1500psi, salt water formation conditions

Time (s)	Pressure (psi)
5604.97	1505.20
40674.97	1484.13
90774.97	1469.94
145884.97	1458.14
155904.97	1457.00
216024.97	1445.21
281154.97	1401.70
351294.97	1372.05
431454.97	1364.95
471534.97	1356.94
496584.97	1357.97
501594.97	1357.85
531654.97	1362.20
536664.97	1361.17

Table B.5 Gulf Of Mexico pressure vs. time formation data for $2^{o}C$, 1500psi, salt water formation conditions #2

Time (s)	Pressure (psi)
859.98	1501.37
42679.98	1492.44
120199.98	1481.33
154879.98	1480.53
224239.98	1469.65
285439.98	1442.98
376219.98	1435.08
426199.98	1431.53
500659.98	1431.64
572059.98	1419.97
591439.98	1418.25

Table B.6 Gulf of Mexico pressure vs. time formation data for 2°C, 1500psi, salt water formation conditions #3

Time (s)	Pressure (psi)
9809.98	1500.84
19829.98	1500.39
29849.98	1497.64
39869.98	1494.66
49889.98	1492.03
59909.98	1491.11
69929.98	1493.63
79949.98	1492.72
89969.98	1492.26
99989.98	1488.94
110009.98	1488.14
120029.98	1487.79
130049.98	1486.30
140069.98	1486.19
150089.98	1486.30
160109.98	1485.50
230249.98	1485.39
310409.98	1482.76
360509.98	1478.75
430649.98	1476.80
520829.98	1472.68
530849.98	1474.97
540869.98	1468.90

Table B.7 Blake Ridge pressure vs. time formation data for 2^{o}C, 1200psi, deionized water formation conditions

Time (s)	Pressure (psi)
2420.92	1187.00
4423.08	1187.34
6425.09	1186.77
8427.09	1186.54
10429.09	1178.41
12431.09	1175.32
14433.08	1174.29
16435.08	1173.60
18437.09	1173.49
20439.09	1172.92
22441.09	1173.03
24443.09	1172.46
26445.09	1170.74
28447.09	1169.02
30449.08	1165.36
32450.95	1164.79
34452.96	1162.16
36454.95	1161.12
38456.96	1157.80
40458.96	1156.20
42460.96	1155.63
44462.96	1154.83
46464.95	1153.00
48466.96	1152.31
50468.96	1151.28
52470.96	1149.45
54472.95	1148.65
56474.96	1146.93
58476.96	1146.01
60478.95	1144.64
62480.88	1143.95
64482.88	1142.92
66484.88	1142.58
68486.88	1141.09
70488.90	1138.80
154572.44	1128.04
242660.25	1121.63
330747.88	1113.04
414831.58	1104.91
502919.26	1102.85
589004.54	1100.33
675090.38	1103.31
761177.22	1100.79
847262.74	1100.33
921336.74	1096.33
1007422.31	1093.81

Table B.8 Gulf of Mexico pressure vs. time formation data for 2^{o}C, 1200psi, deionized water formation conditions

Time (s)	Pressure (psi)
10024.98	1185.41
100114.98	1179.46
185199.98	1175.22
280294.98	1177.17
330344.98	1168.93
435449.98	1163.55
525539.98	1165.26

Table B.9 Gulf of Mexico pressure vs. time formation data for 6^{o}C, 1200psi, deionized water formation conditions

Time (s)	Pressure (psi)
5020.02	1183.34
90111.37	1170.07
175212.21	1169.95
260297.81	1168.24
345383.60	1164.23
430489.24	1161.94
515580.25	1163.77
580656.08	1158.96

Table B.10 Gulf of Mexico pressure vs. time formation data for 2°C, 900psi, deionized water formation conditions

Time (s)	Pressure (psi)
5630.04	918.18
30655.20	908.45
60685.39	905.47
100725.85	902.61
120750.89	896.89
165790.27	896.09
205829.17	893.45
210834.17	893.11
215839.17	892.54
220844.17	892.19
225849.17	892.54
230854.17	892.08
235859.17	892.88
240864.17	892.65
245869.17	891.05
250874.17	891.39
255879.17	891.16
300924.17	890.82
305929.17	890.02
310934.17	889.68

Table B.11 Gulf of Mexico pressure vs. time formation data for 2^{o}C, 900psi, deionized water formation conditions

Time (s)	Pressure (psi)
2002.00	912.26
61744.00	851.45
123744.00	839.20
180744.00	833.03
241744.00	826.78
322744.00	820.94
400744.00	817.76
480744.00	814.50
540744.00	812.39
600744.00	809.78
663744.00	809.54
740744.00	807.61
800744.00	805.40
864744.00	803.94
919744.00	802.83
980744.00	801.67
1044744.00	800.53
1076744.00	799.44